ATOMISTIC SIMULATION OF TRANSITION METAL OXIDES AND LAYERED PHYLLOSILICATE MATERIALS

By

R. SEATON ULLBERG

A DISSERTATION PRESENTED TO THE GRADUATE SCHOOL
OF THE UNIVERSITY OF FLORIDA IN PARTIAL FULFILLMENT
OF THE REQUIREMENTS FOR THE DEGREE OF
DOCTOR OF PHILOSOPHY

UNIVERSITY OF FLORIDA

2024

To my Mom, Dad, family, and friends who have supported me the whole way

ACKNOWLEDGMENTS

I would like to begin by expressing my most sincere appreciation for my advisor, Prof. Simon R. Phillpot, without whom I would have never chosen to pursue graduate studies. His patient guidance and brilliant insights have paved the way for my success as a budding scientist. The passion he so clearly has for discovery and the optimism with which he tackles challenges will continue to serve as guiding principles in my own life both personally and professionally. His style of leadership is compassionate and inspires deep personal development which I have been a tremendous beneficiary of. The support and reassurance he has provided to me over the course of my graduate journey cannot be overstated – I simply could not have imagined a better advisor.

I would also like to thank my collaborators, Prof. Adrien Couet, Prof. Nathalie Wall, Prof. Megan Butala, and all contributors to the SStAC and NEUP projects which are so central to this dissertation. They have enabled me to explore cutting-edge research topics spanning a wide range of materials systems and simulation methodologies. Each collaborator has imparted upon me a deeper understanding of the myriad topics they are so passionate about by expressing a genuine excitement to help advance scientific understanding not just in the abstract, but on a personal level.

I am grateful for my committee members, Prof. Michael Tonks, Prof. Victoria Miller, and Prof. Youping Chen for their continued guidance and commitment to holding me accountable for conducting high quality research. In particular, I would like to thank Prof. Tonks for his leadership on the SStAC project which kickstarted my graduate career.

Members of the Phillpot Research Group, both past and present, are also deserving of my sincere gratitude. Dr. Ximeng Wang and Dr. Yuan Liu have always

been a source of joy in my day, not to mention their valuable scientific insights and ability to bring the group together for some much needed out-of-office camaraderie. I am so grateful to have worked with Dr. An Ta, his wealth of experience with molecular dynamics has saved me on a number of occasions and the scientific discussions we have always inspire me to think creatively and remain curious. I would especially like to thank Dr. Eugene Ragasa who constantly fueled my interest in programming and got me involved in impactful research as an undergraduate that ended up being extremely helpful in my graduate studies.

I would like to express my profound love and appreciation for my family and friends. My Mom and Dad have always been selflessly committed to placing my needs above all else. Without their support I could never have achieved this. I am beyond grateful for the support my Oma and FarFar have shown me. Their excitement to hear about what I have been working on is infectious and motivates me to achieve the heights they know I am capable of. I wish my late Grandma and Grandpa could read this so that I could share just how much their love and guidance played a role in my achievement. They will be with me always. Finally, I would be remiss not to thank each and every one of my dear friends. Every moment we share together reminds me what life is all about and makes me feel recharged. Thank you.

TABLE OF CONTENTS

page

LIST OF TABLES

LIST OF FIGURES

LIST OF ABBREVIATIONS

CHGNet	Crystal Hamiltonian Graph Neural Network
DFT	Density Functional Theory
DRX	Disordered Rocksalt
GGA	Generalized Gradient Approximation
HEO	High Entropy Oxide
HLW	High Level Waste
IMB	Interlayer Mesopore Boundary
MD	Molecular Dynamics
NEB	Nudged Elastic Band Method
SQS	Special Quasirandom Structure
SRO	Short Range Order

Abstract of Dissertation Presented to the Graduate School
of the University of Florida in Partial Fulfillment of the
Requirements for the Degree of Doctor of Philosophy

ATOMISTIC SIMULATION OF TRANSITION METAL OXIDES AND LAYERED PHYLLOSILICATE MATERIALS

By

R. Seaton Ullberg

May 2024

Chair: Simon R. Phillpot
Major: Materials Science and Engineering

$MnCr_2O_4$ spinel is a component of the multilayered oxide film which forms atop austenitic steel alloys under high-temperature corrosion conditions. The thermodynamics and kinetics of cationic and anionic point defects in this spinel are examined through density functional theory calculations. To model the physical conditions of the corrosion process more closely, temperature is accounted for by adjusting the chemical potential of each species to fit experimentally determined values. We find that manganese is the most mobile species - migrating through the lattice via a vacancy mediated mechanism. Oxygen migration can occur via vacancy mediated or three-body interstitial mechanisms with similarly low barrier heights, highlighting the possibility of oxide growth at the film/alloy interface due to the high oxygen permeability. Furthermore, a selection of more complex migration mechanisms involving substitution and antisite defects are evaluated for their potential contribution to cation mobility.

Phyllosilicate clay minerals have been proposed as a possible buffer material to be used in deep geological repositories containing high-level waste and used nuclear fuel. Here, we characterize how ions interact with two types of adsorption sites present

in these clays: Mg_{Al}' substitutions and undercoordinated edge surface atoms. We consider multiple structural models representative of the local environments that ions in these systems are likely to encounter. Using molecular dynamics simulation with the CLAYFF potential, we investigate the spatial distribution, interlayer composition, and residence times of Na^+ and Cl^- ions as radionuclide analogs in pyrophyllite and montmorillonite to identify the most favorable conditions for sequestration. The most significant factor impacting ion adsorption is found to be the localization of charge density at substitution sites.

Disordered rocksalt (DRX) materials are a promising new high entropy oxide system to create advanced cathodes for Li-ion batteries. While there are promising results showing significant improvements in capacity relative to conventional layered transition metal oxide cathodes, short range order (SRO) induced by charge discharge cycling degrades the reversible capacity. Density functional theory (DFT) and novel crystal graph neural network methods are employed to predict SRO formation and screen a wide compositional space for new materials capable of resisting SRO formation during cycling.

CHAPTER 1
INTRODUCTION

1.1 Overview

Rapid growth in raw computational power and expanded access in the era of cloud computing has been a tremendous boon for research scientists in all domains. Computer simulations of real physical systems can serve as a valuable complement to experiments in situations where achieving a desired measurement is costly, dangerous, or time consuming. Historically, the cost of computational resources has limited what was deemed reasonable or even possible to offload to simulation, but the commoditization of “compute” in the modern era has drastically changed that calculus [1]. The field of materials science is well suited to benefit from significant investment in simulation.

With interesting problems to solve at length scales ranging from Angstroms to meters, no single technique is flexible to be applicable in all situations. However, the problem becomes more tractable when the physical phenomena associated with each length scale are framed as a hierarchy. At the bottom, quantum mechanical effects control interactions between individual atoms and can be reasonably considered up to about 10 nm. To address problems on this scale, we have ab-inito methods like density functional theory (DFT) which offer the highest fidelity at the greatest computational cost. Stepping beyond that, interactions on the order of 1000 nm are better served by classical atomistic methods like molecular dynamics (MD) which approximates individual atoms as classically interacting particles thus losing the quantum mechanical accuracy of DFT but gaining a tremendous amount in maximum system size. Further up still is the mesoscale which is on the order of 10 μm. Methods such as phase-field

modeling commonly operate at this level. The top of the hierarchy may be referred to as the engineering scale which includes methods such as finite element modeling (FEM) where the subject of the simulation would be easily perceptible to the human eye. The choice of a simulation methodology is ultimately a decision of efficient trade-offs depending on the property that needs to be calculated and the accuracy required to make the prediction useful.

In this dissertation, simulation is used across multiple length scales highlighting the strengths of each tier of the hierarchy. DFT is used to evaluate high fidelity kinetic barriers of point defects in an oxide film which ultimately informs diffusivity over the mesoscale. MD simulation is used to probe dynamical properties of flexible molecules and an aqueous solution interacting with nanoscale representation of clay buffer materials. Lastly, emerging machine learning (ML) methods which achieve near-DFT accuracy at a fraction of the computational cost are applied to an emerging class of cathode materials to advance Li-ion battery performance.

1.2 High Temperature Corrosion of Stainless Steel Alloys

The cost of corrosion damage in the United States alone is estimated to be upwards of $276 billion annually [2]. Materials failure instigated by corrosion damage tends to result in abrupt brittle fracture, through stress corrosion cracking, making the problem a safety hazard as well as an economic drain. Corrosion can be particularly impactful in high-tech industrial applications such as aerospace or nuclear energy where materials are pushed to their limits to maximize performance. In these fields, austenitic stainless steel alloys are ubiquitous structural materials due to their unique balance of mechanical robustness, cost, and of course, corrosion resistance. Under standard conditions, austenitic steels are highly resilient to corrosion damage. However,

in the extreme environmental conditions required to operate these cutting-edge technologies, the resistance can quickly degrade [3], [4], [5].

The standard model for understanding how stainless steels are passivated relies heavily on the behavior of Cr near grain boundaries. Under standard conditions, Cr is an excellent passivating agent and its relatively high availability in the steel matrix (usually > 16 wt. %) means that it can preferentially oxidize to form a passive surface film that protects the Fe. However, at higher temperatures in the range of 600 – 800 ºC, the alloy undergoes a process known as sensitization in which the Cr tends to migrate to the grain boundaries and form $Cr_{23}C_6$ precipitates. This migration leaves the region near the grain boundary depleted in Cr which limits the ability to form a passivating layer. The critical Cr composition below which passivation begins to fail is reported as 12 wt. % [6].

Recent experimental work has shown that the oxide film which develops atop austenitic steel alloys exposed to high temperature (> 700 ºC) tends to have a layered structure as shown in Figure 1-1. Not only does the total thickness of the oxide grow over time, but the relative amounts of each layer change. This presents an interesting question about what the rate limiting mechanisms are that control oxide growth and the migration of cations and oxygen between layers.

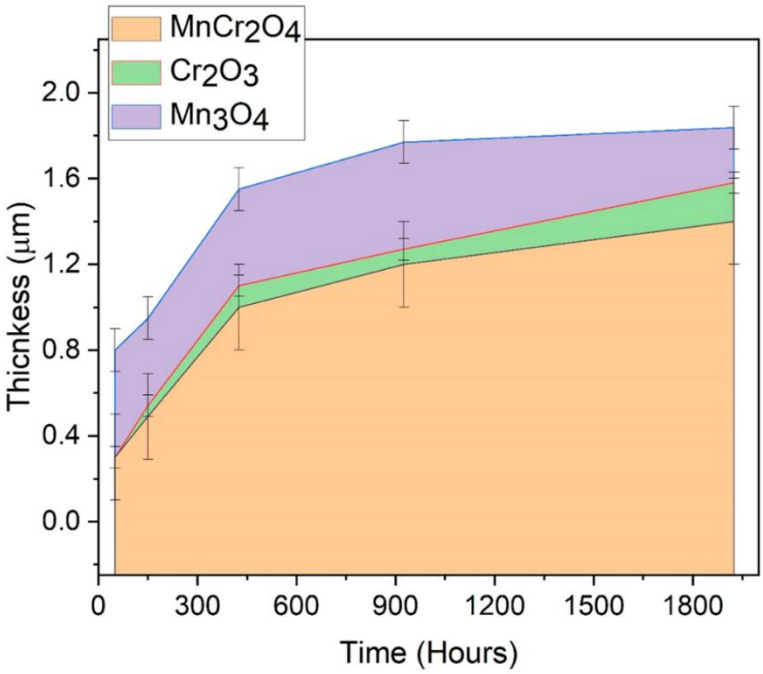

Figure 1-1. Change in oxide thickness as a function of exposure time. (Adapted from I. Abdallah et al., Corros. Sci., 2022 [7])

From inspection of Figure 1-1, the $MnCr_2O_4$ phase mediates the flow of cations coming from the bulk alloy below to the outermost oxide surface. This presents the challenge of characterizing kinetic barriers to migration through this complex spinel phase in order to fully understand the atomistic mechanisms driving oxide growth. By evaluating migration barrier heights of point defects through this phase it is possible to inform a hierarchical model that can operate on engineering time and length scales to predict how the layers ultimately equilibrate.

1.3 Functionalized Clay Buffer Materials for Radionuclide Sequestration

Nuclear energy offers a promising way to achieve low-emission energy independence in an era where energy consumption is growing rapidly [8], [9]. While the technology is capable of producing tremendous amounts of energy, the question of how to manage the dangerous high level waste (HLW) products it generates poses a great challenge to researchers. One technique that has been adopted by multiple nations with

established nuclear energy programs is the use of deep geological repositories to hold the waste packages [10], [11]. A schematic of such a repository is presented in Figure 1-2. These HLW waste packages contain radioactive fission products such as iodine-129 and technetium-99 which can take the take the form of aqueous pertechnetate (TcO_4^-), iodate (IO_3^-), and iodide (I^-) [12]. Therefore, any proposed storage solution must remain stable for hundreds of years, withstand the radiation damage, and prevent the leeching of radionuclides which could pollute groundwater sources.

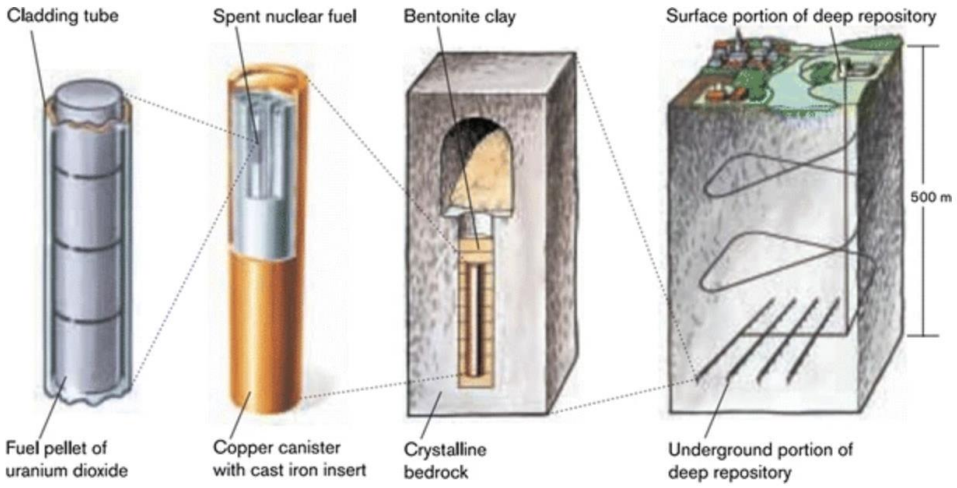

Figure 1-2. Schematic depicting the components of a deep geological repository for HLW disposal. (Adapted from Y. G. Chen et al., Environ Earth Sci., 2016 [13])

One crucial component of the geological storage system is the use of a clay buffer material to insulate the waste package from the surrounding geosphere. Clays are uniquely well suited to the task because they are abundant in the earth's crust, can swell to limit the influx of groundwater, and they are stable over the extended timescales required to neutralize the radioactive load. Recent work has shown that the radionuclide sequestration performance of the clay buffer can be optimized by functionalizing the structure with bare metallic cations and long-chain alkylammonium molecules [14]. This

finding presents an interesting opportunity to investigate the precise atomistic mechanisms driving the improved sequestration performance.

1.4 High Entropy Li-Oxide Cathode Materials

The energy storage capacity of modern Li-ion batteries has become a bottleneck in building the infrastructure required to power a stable energy grid using renewable sources of energy. To break through this limitation researchers are turning to entirely new material systems to improve the energy density of future battery technologies. One novel material being considered is high entropy oxides (HEO) with excess Li concentration. These prospective materials are promising candidates due to the ability to exploit both cation ($Mn^{3+/4+}$) and anion ($O^{2-/}F^{-}$) redox reactions (Figure 1-3), the vast compositional space that can be tailored to optimize performance, and the possibility to develop efficient compositions that exclude highly polluting or inaccessible transmission metal components [15]. One particular crystal structure which has been popularized in the literature is rocksalt. On the rocksalt lattice, cation disorder can contribute to improved Li permeation while the anion sublattice is often left as pure O or may be doped with a small fraction of F [16]. This structural motif is commonly referred to as disordered rocksalt (DRX).

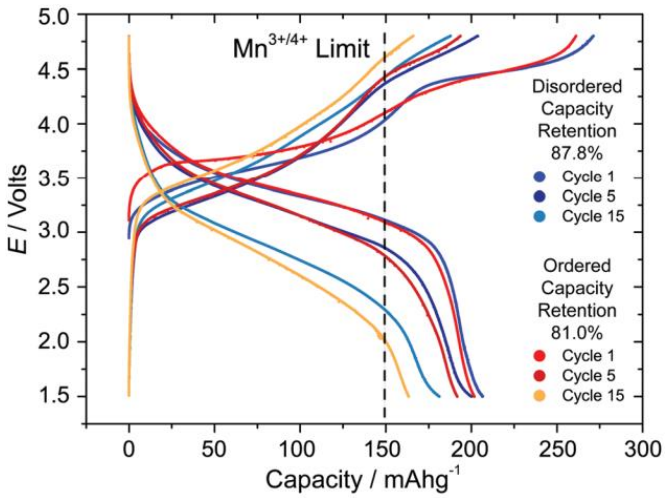

Figure 1-3. Charge discharge diagram depicting the improved energy capacity of Li-HEO batteries surpassing the Mn redox limit denoted by the vertical dashed line. (Adapted from M. A. Jones et al., Chem. Comm., 2019 [17])

Despite promising capacity measurements in lab experiments [18], [19], the sintering process when synthesizing these materials tends to induce short range order (SRO) into the cation lattice which can have deleterious effects on the mobility of Li. This effect is exacerbated during charge/discharge cycles which tend to result in larger clusters of Li that reduce the fraction of Li available to migrate through the lattice and contribute to ion conductivity. The consequences of this behavior are well understood from an experimental perspective, but atomistic details of the structural and compositional factors which contribute to SRO formation have not been fully investigated. This challenge presents an opportunity to use computational methods to accelerate the screening of new compositions for experimentalists to synthesize and to contribute to the theory of SRO formation with detail at the atomic scale.

CHAPTER 2
COMPUTATIONAL METHODS

2.1 Density Functional Theory

2.1.1 Foundational Principles

Density functional theory (DFT) is a quantum mechanical method to compute the electronic structure of a system of atoms. It strikes a balance between computational cost and consistency with physical measurement that makes it a highly effective tool to study both molecules and crystalline matter. In its original formulation, DFT relies on the concept of electron density to compute the ground state properties of a system. In application to solid state physics and quantum chemistry, most methodologies rely on the time-independent, non-relativistic Schrödinger equation (Equation 2-1) to evaluate the total energy of a system.

$$\widehat{H}\Psi_i\left(\vec{x}_1, \dots, \vec{x}_N, \vec{R}_1, \dots, \vec{R}_M\right) = E_i\Psi_i(\vec{x}_1, \dots, \vec{x}_N, \vec{R}_1, \dots, \vec{R}_M) \quad (2\text{-}1)$$

In this equation, $\widehat{H}$ is the Hamiltonian of a system containing M nuclei and N electrons, Ψ_i is the eigenstate wavefunction, and E_i is the eigenvalue.

The substantial difference between the mass of the nuclei and electrons leads to a commensurate difference in their velocities. Because of this difference, we can model the system as electrons moving through a field of fixed nuclei. This development yields a key approximation in our understanding of quantum mechanics – the Born-Oppenheimer approximation [20]. The approximation states that the nuclear kinetic energy is zero and the nuclear potential energy is time dependent under the assumption that electron wavefunctions are equilibrated with respect to the nucleus. Applying this approximation, we can represent the reduced electronic Hamiltonian ($\widehat{H}_e$) in the following way:

$$\hat{H}_e = \left[-\frac{\hbar^2}{2m_e} \sum_i^N \nabla_i^2 + \sum_{i,I} \frac{Z_I e^2}{|r_i - R_I|} + \frac{1}{2} \sum_{i \neq j} \frac{e^2}{|r_i - r_j|} \right] = \hat{T} + \hat{V}_{N-e} + \hat{V}_{e-e} \qquad (2\text{-}2)$$

where the subscripts i and j index the N electrons in the system and the subscript I indexes the nuclei in the system. m_e is the mass of one electron, Z_I is the atomic number of nucleus I, and the vectors $\vec{r}_i$ and $\vec{R}_I$ refer to the spatial coordinates of the electrons and nuclei respectively. Equation 2-2 can be broken down into three components: kinetic energy of the electrons ($\hat{T}$), electrostatic interactions between nuclei and electrons ($\hat{V}_{N-e}$), and the repulsive potential between two electrons ($\hat{V}_{e-e}$). To this point, all equations have been defined in terms of a wavefunction which has the limitation of being an unobservable quantity. Instead, we can utilize the Hamiltonian's reliance on the number of electrons in a system to reformulate these relations in terms of electron density, which is an observable quantity. To connect these quantities, we express the number of electrons N as the integral of the electron density ρ over all space as shown in Equation 2-3.

$$N = \int \rho(r) dr \qquad (2\text{-}3)$$

Electron density may be better understood as the probability of finding an electron within a unit volume at a specific position in space. This is expressed below in Equation 2-4:

$$n(r) = \sum_i \Psi_i^*(r) \Psi_i(r) \qquad (2\text{-}4)$$

where Ψ_i^* is the complex conjugate of the waveform Ψ_i.

The Hohenberg-Kohn theorems provide the next step in understanding the foundations of DFT - specifically the Existence Theorem and the Variational Theorem [21]. The Existence Theorem states that the external potential (v_{ext}) of an *N*-electron system is a unique functional of the ground state electron density n_0. It goes on to

describe that in a uniform electron gas, the external potential exists as a uniformly distributed positive charge, while in a molecule, the external potential creates an attraction to the nuclei. Following these constraints, the total energy of a system can be expressed according to Equation 2-5.

$$E[\rho] = E_{N-e}[\rho] + T[\rho] + E_{e-e}[\rho] \quad (2\text{-}5)$$

The Variational Theorem states that the functional which produces the ground state energy of system results in the lowest energy if and only if the input density is the true ground state density ($E_0 \leq E[\tilde{\rho}]$). Therefore, for any candidate density ($\tilde{\rho}$) which satisfies the necessary boundary conditions, the energy returned by Equation 2-5 represents an upper bound of the true ground state energy E_0.

The next foundational principal is that of the Kohn-Sham equations [22]. Kohn and Sham made the advancement of applying the Hamiltonian operator to a system of non-interacting electrons after coming to the conclusion that such an expression would be considerably simpler. The revised Hamiltonian has the following properties which make it more computationally feasible: it can be expressed as a sum of one-electron operators, its eigenfunctions are Slater determinants of the individual one-electron eigenfunctions, and its eigenvalues are the sum of the one-electron eigenvalues. The Kohn-Sham equations can be expressed as follows:

$$\left[-\frac{\hbar^2\nabla^2}{2m} + v_{ext}(r) + v_H(r) + v_{xc}(r)\right]\phi_i = \varepsilon_i\phi_i(r) \quad (2\text{-}6)$$

where ϕ_i represents the single particle orbitals of the non-interacting system, the Hartree potential ($v_H = e^2 \int \frac{n(r)}{|r-r'|} d^3r'$) represents the Coulombic repulsion between particles, and the non-classical corrections to the electron-electron repulsion energy are

described by the exchange-correlation potential ($v_{xc} = \frac{\delta E_{xc}[n]}{\delta n}$). This DFT formulation is the most widely used electronic structure method due to its computational efficiency and high fidelity. In fact, Kohn-Sham DFT (KS-DFT) would be able to perfectly describe the electron density and ground state energy of a system if exact exchange-correlation energy could be given. In practice, exact exchange-correlation energies are not known and thus exist as the only term in KS-DFT which must be approximated [23], [24], [25].

2.1.2 Exchange-Correlation Functionals

As stated in Chapter 2.1.1, KS-DFT relies on approximate exchange-correlation energies in order to predict the electron density and ground state energy of a system of atoms. These energies are provided in the form of functionals which may take as inputs a number of functions beyond just local electron density, such as derivatives of density, to improve their fidelity relative to physical measurements. Using this approach of including additional inputs to formulate the exchange-correlation energy, a hierarchy of methods has been established which increases in both complexity and fidelity. The first rung of this so-called "Jacob's ladder" is the Hartree level of theory [24], but the highest level of theory would be considered chemical accuracy which is broadly described as having an error of less than 1 kcal/mol. The lower levels of the hierarchy can be generalized in the following equation:

$$E_{xc}[n_\uparrow, n_\downarrow] = \int d^3r n\varepsilon_{xc}(n_\uparrow, n_\downarrow, \nabla_\uparrow, \nabla_\downarrow, \tau_\uparrow, \tau_\downarrow) \qquad (2\text{-}7)$$

where $n_\uparrow$ and $n_\downarrow$ are the up and down electron spin densities respectively, ε_{xc} is the exchange-correlation energy density per unit volume, $n(r) = n_\uparrow(r) + n_\downarrow(r)$ is the total density, and $\tau_\sigma(r) = \sum_i^{occup} \frac{1}{2}|\nabla\Psi_{i\sigma}(r)|^2$ is the kinetic energy density for the occupied KS orbitals $\Psi_{i\sigma}(r)$. Additionally, each KS orbital is a nonlocal functional of the density $n_\sigma(r)$.

The lowest level of the hierarchy is called the local density approximation (LDA) and is obtained by removing the ∇_n and τ terms from Equation 2-7. LDA can also be expanded to treat up and down spin densities independently in which it is referred to as the local spin density approximation (LSDA). The LDA is an exact solution for any uniform electron gas. When applied to real material systems, it tends to minimize electron density inhomogeneity and overestimate bond strengths when bond lengths are close to their equilibrium values [22], [26], [27], [28].

The generalized gradient approximation (GGA) is the next level in the hierarchy [23], [29], [30]. Under this approximation, only the τ term of Equation 2-7 is dropped. As the name suggests, the gradient of the electron density remains an input parameter. This treatment tends to predict weaker bonds in real materials. Furthermore, the GGA may not be able to predict accurate energies and geometries simultaneously depending on the construction of the density gradient [31]. More precisely, GGA is incapable of accurately satisfying the slowly varying density limit in extended systems and the strict lower bound on the exchange energy of a single-orbital system simultaneously [25]. In practice, this often requires simulations to be run in two parts where an initial structural relaxation is conducted to achieve an appropriate input geometry and a subsequent single point calculation is done to produce the most accurate total energy value. A variety of GGA functionals are available such as Perdew-Wang91 (PW91) [28], Perdew-Burke-Ernzerhof (PBE) [30], and Armiento-Mattsson05 (AM05) [32], [33], but the PBE is widely regarded as a balanced solution to both structural relaxation and total energy prediction. Higher order functionals exist which are capable of achieving near chemical accuracy for specific physical phenomena, but PBE-GGA is the functional used

consistently throughout all DFT portions of this work so descriptions of higher levels of theory are considered out of scope.

2.1.3 DFT+U Approximation

While the PBE-GGA DFT formalism has proven to be effective in simulating low Z elements, it struggles to accurately model compounds which have partially filled d- and f-shells. The theory fails because electron tunneling may be suppressed by Coulombic repulsion between electrons which causes the motion of electrons to become strongly correlated if the amplitude of tunneling is less than or equal to the Hubbard U term. The Hubbard U term describes the energy of repulsion between electrons occupying the same atomic shell. The +U approximation was initially developed to rectify Coulombic interactions between 5f electrons in uranium oxide and 3d electrons in nickel oxide [34], [35]. To accurately describe Coulombic interactions between f and d electrons, orbital degeneracy must be considered by using the following Hamiltonian:

$$\widehat{H} = \frac{\bar{U}}{2}\sum_{m,m',\sigma} \hat{n}_{m,\sigma}\hat{n}_{m',-\sigma} + \frac{(\bar{U}-\bar{J})}{2}\sum_{m\neq m',\sigma} \hat{n}_{m,\sigma}\hat{n}_{m',-\sigma} \qquad (2\text{-}8)$$

where the sum is taken over projections of the orbital momentum, $\bar{U}$ and $\bar{J}$ are the spherically averaged matrix elements of the screened Coulomb electron-electron interaction [34], [35]. Dudarev et al. [35] derived the matrix for the effective +*U* potential as shown in the following:

$$V_{jl}^{\sigma} \equiv \frac{\delta E_{LSDA+U}}{\delta \rho_{lj}^{\sigma}} = \frac{\delta E_{LSDA}}{\delta \rho_{lj}^{\sigma}} + (\bar{U}-\bar{J})[\frac{1}{2}\delta_{jl} - \rho_{jl}^{\sigma}] \qquad (2\text{-}9)$$

where ρ_{lj}^{σ} is the density matrix of electrons which occupy partly filled shells. The total energy of the system can be expressed in terms of its Kohn-Sham eigenvalues $\{\varepsilon_i\}$.

$$E_{LSDA+U} = E_{LSDA}[\{\varepsilon_i\}] + \frac{(\bar{U}-\bar{J})}{2}\sum_{l,j,\sigma} \rho_{lj}^{\sigma}\rho_{jl}^{\sigma} \quad (2\text{-}10)$$

The Hubbard correction influences the dispersion of electron states which can lead to the introduction of a band gap in an otherwise metallic band structure. This band gap formation is a function of the chosen +*U* parameter. The correction term can also impact the total energy of the system by altering the position of the minimum in the total energy functional from Equation 2-10 which may change the equilibrium geometry of the system. Despite the benefits that the +*U* approximation can provide; it does introduce a new approximation. Typically, the $\bar{U}$ and $\bar{J}$ values are determined by fitting to relevant experimental data for the physical properties of interest.

2.1.4 Plane-Wave Basis Set

The KS-DFT formalism requires basis sets, which represent the electronic wave function, to formulate the underlying physics as a set of algebraic expressions which can be solved numerically. A plane-wave basis is set is typically used for condensed matter applications because they are well suited for periodic boundary conditions. Using the plane-wave basis set scheme requires the addition of a pseudopotential to model the behavior of atomic core electrons (electrons which are not involved in bonding). The pseudopotential implementation used in this work is the projector augmented wave method (PAW) [36], [37]. The PAW one-electron orbitals (Ψ_n) are modeled by the following equation:

$$\Psi_n\rangle = \widetilde{\Psi}_n\rangle + \sum_i(\varphi_i\rangle - \tilde{\varphi}_l\rangle)\langle\tilde{p}_i|\widetilde{\Psi}_n\rangle \quad (2\text{-}11)$$

where the pseudo orbitals ($\widetilde{\Psi}_n$) are variational quantities expanded in plane waves. The all-electron and pseudo partial waves are represented by φ_i and $\tilde{\varphi}_l$ respectively. These waves serve as additional local basis functions that are nonzero valued within the atom-centered PAW spheres. Between two atomic sites, the one-electron and pseudo orbitals

are identical with the pseudo orbital operating as a mathematical tool to approximate the true wave function.

2.1.5 Spin-Orbit Coupling

Spin-orbit coupling (SOC) is defined as the relativistic interaction between a particle's spin and its movement through a potential. This phenomenon has significant implications in modeling the motion of electrons around a charged nucleus. In first principles calculations, we have the option to toggle this effect on or off. In this work, all DFT calculations are spin-polarized and thus include the effect of this interaction. Considering SOC leads to a change in energy as a function of the orientation of each atom's magnetic moment. This allows for the study of magnetic ground states, i.e., probing the favorability of an antiferromagnetic orientation relative to a ferromagnetic one for an identical site geometry.

Under the PAW formalism, the effect of SOC can be reduced to the following all-electron one-center contribution:

$$\widetilde{H}_{SOC} = \sum_{ij} p_i\rangle \langle\varphi_i|H_{SOC}|\varphi_j\rangle\langle p_j \qquad (2\text{-}12)$$

Using the zeroth-order regular approximation [38], the Hamiltonian is given by $H_{SOC}^{\alpha\beta} \propto \vec{\sigma} \cdot \vec{L}$ where $\vec{\sigma}$ is the Pauli spin operator and $\vec{L}$ is the angular momentum operator. The matrix elements of H_{SOC} are calculated in the following way:

$$E_{SOC}^{ij} = \delta_{R_i}\delta_{R_j}\delta_{l_i l_j} \sum_{\alpha\beta} \left\langle \varphi_i \middle| H_{SOC}^{\alpha\beta} \middle| \varphi_i \right\rangle \qquad (2\text{-}13)$$

where R_i represents the center of an atomic site and α and β represent the spin-up and spin-down components of the two-component spinor wave function. Separating into up and down components is required to account for noncollinear magnetism [39].

2.2 Molecular Dynamics

2.2.1 Integrating the Equations of Motion

Molecular dynamics (MD) is an atomistic simulation technique which treats atoms as classical particles and propagates their motion by using an iterative algorithm to solve Newton's kinematic equations at discrete timesteps. This relation can most broadly be described by the following equation:

$$F_i = m_i \frac{dr_i}{dt} = -\frac{\delta \mathrm{U}}{\delta r_i} \quad \text{(2-14)}$$

where F_i is the force acting on atom i, m_i is the mass of atom i, r_i is the position of atom i, and U is the potential energy of the system. While treating atoms as classical particles inherently ignores quantum effects that are impactful on the atomic scale, the computational efficiency of this method allows for simulations on the order of 10^7 atoms when executed on powerful computer clusters. The length and time scales of MD simulations are inaccessible to first principles methods (on the order of 10^2 atoms) which makes it a valuable tool to investigate dynamical processes despite the reduced fidelity.

The form of potential energy as structured in Equation 2-14 scales with the number of atoms in the simulation which makes an analytical integration intractable for systems of sufficient size. Therefore, numerical methods have been developed which are capable of running in parallel on high performance computer hardware to drastically reduce total runtime. To derive a numerically solvable method we begin by using a Taylor series expansion of the current position to predict the position and velocity at the next timestep:

$$r_i(t + \Delta t) = r_i(t) + v_i(t)\Delta t + \frac{1}{2}\Delta t^2 a(t) + \frac{\Delta t^3}{3!}\frac{dr_i}{dt^3} + O(\Delta t^4) \quad \text{(2-15)}$$

we also consider the previous timestep:

$$r_i(t-\Delta t) = r_i(t) - v_i(t)\Delta t + \frac{1}{2}\Delta t^2 a(t) - \frac{\Delta t^3}{3!}\frac{dr_i}{dt^3} + O(\Delta t^4) \qquad (2\text{-}16)$$

where a_i is the acceleration of atom i at time t. Add Equations 2-15 and 2-16 together:

$$r(t+\Delta t) + r(t-\Delta t) = 2r(t) + \Delta t^2 a(t) + O(\Delta t^4) \qquad (2\text{-}17)$$

simplify and discard the quadratic term:

$$r(t+\Delta t) = 2r(t) - r(t-\Delta t) + \Delta t^2 a(t) \quad (2\text{-}18)$$

this form introduces an error in the position at the next timestep of $O(\Delta t^4)$ where Δt is the simulation timestep. This shows that error in the simulation may be reduced by decreasing the timestep, but this comes at the expense of increased computer runtime for simulations of equivalent simulated time. Having established a solution for position, it follows that velocity can be calculated in the following way:

$$v(t) = \frac{r(t+\Delta t) - r(t-\Delta t)}{2\Delta t} \qquad (2\text{-}19)$$

this form has an error of Δt^2. Expanding on this equation, Swope et al. [40] developed the velocity Verlet algorithm as an efficient way to numerically propagate a system of atoms in a MD simulation. The solutions for position and velocity at the first time step are expressed in the equations below:

$$x(t+\Delta t) = x(t) + v(t)\Delta t + \frac{1}{2}a(t)\Delta t^2 \qquad (2\text{-}20)$$

$$v(t+\Delta t) = v(t) + \frac{a(t)+a(t+\Delta t)}{2}\Delta t \quad (2\text{-}21)$$

Propagation of the system then proceeds as follows:

1) Calculate an updated half-step velocity $v\left(t+\frac{1}{2}\Delta t\right) = v(t) + \frac{1}{2}a(t)\Delta t$.
2) Calculate an updated position using the new velocity $x(t+\Delta t) = x(t) + v(t + \frac{1}{2}\Delta t)\Delta t$.

3) Derive an updated acceleration $a(t + \Delta t)$ from the forces predicted by interatomic potentials using the new positions $x(t + \Delta t)$ as input.
4) Finalize the velocity update $v(t + \Delta t) = v\left(t + \frac{1}{2}\Delta t\right) + \frac{1}{2}a(t + \Delta t)\Delta t$.

Note that this implementation assumes acceleration is dependent only on position and cannot be influenced by velocity.

2.2.2 Interatomic Potentials

Interatomic potentials are mathematical functions which are used to predict the potential energy of a system of atoms and the forces acting on those atoms. The simplest formulations take only a pairwise distance between a pair of atoms as an argument, and through the use a few fitted parameters, can be modified to predict the energy and forces for many different materials systems. For the case of a simple pair potential, the total potential energy V has the following form:

$$V = \sum_{i,j=1}^{N} V_{pair}(r_{ij}) \quad (2\text{-}22)$$

where the subscripts i and j index through all N atoms in the system. The function $V_{pair}(r)$ represents the interatomic potential and takes as its argument the pairwise distance between atoms i and j where $i \neq j$. This scheme can be expanded out to account for many-body interactions which typically produces more accurate simulations at the cost of computational resources. The forces acting on the atoms can be evaluated by differentiating the potential energy of the system with respect to the atomic positions as follows:

$$\vec{F}_i = -\nabla_{\vec{r}_i} V \quad (2\text{-}23)$$

where the force $\vec{F}_i$ acting on atom i at position $\vec{r}_i$ is the gradient of the potential energy with respect to the atomic position. A signed value is used to distinguish between repulsive and attractive forces.

2.2.3 Thermostats and Barostats

In isolation from mechanical and thermal influences, a system of atoms will maintain a constant total energy while temperature and pressure fluctuate to maintain equilibrium. However, to address many real-world problems, it is important to maintain a fixed temperature or pressure on a system such that it reflects the physical conditions of the application domain. Such constraints may be useful to investigate material properties such as thermal conductivity or elasticity. These quantities may also need to be controlled in order to initialize a system and find a stable equilibrium to serve as a starting point for further simulation.

Because temperature is a macroscopic measure of the kinetic energy of atoms in a system, one can control the system temperature by rescaling the velocities of its atoms. A direct velocity scaling factor can be calculated using the following equation:

$$\beta = \sqrt{E_k^D / E_k} = \sqrt{T^D / T} \qquad (2\text{-}24)$$

where the desired kinetic energy E_k^D, being proportional to the desired temperature T^D, is simply divided by the current value. While this method may be trivial to implement, it is not recommended for real simulations as it does not correspond to any thermodynamic ensemble and does nothing to resolve the correlated motion of particles [41]. A more physically representative and well-established method to control temperature is the Nose-Hoover thermostat [42], [43]. This method adds a friction term

ζ to the equations of motion which implicitly controls temperature. The method is described by the following adjusted equations of motion:

$$m_i \frac{d^2 r_i}{dt^2} = f_i - \zeta m_i v_i \qquad (2\text{-}25)$$

$$\frac{d\zeta(t)}{dt} = \frac{1}{Q}\left[\sum_i \frac{m_i v_i^2}{2} - N_f k_B T^D\right] \qquad (2\text{-}26)$$

Where Q is a variable parameter which controls the relaxation of the friction term.

A simple barostat, employing a technique similar to that of the velocity scaling thermostat, can be implemented by adjusting the volume of the simulation cell until the calculated pressure is in agreement with a given target value. This volume scaling algorithm is known as the Berendsen barostat [44] which can be described by the following equations:

$$V^{new} = V^{old} \cdot \lambda \qquad (2\text{-}27)$$

$$r_i^{new} = r_i^{old} \cdot \lambda^{1/3} \qquad (2\text{-}28)$$

where λ is a variable scaling parameter which controls how aggressively the volume is scaled. In practice, scaling the volume is analogous to scaling the position of each particle in the system. Therefore, for a three-dimensional system, each position is scaled by the cube root of the scaling factor λ to achieve the desired effect. The scaling factor changes as a function of the difference between the target pressure and actual pressure according to the following equation:

$$\lambda = \left(1 - \frac{k\delta t}{\tau}\left(P(t) - P_{target}\right)\right) \qquad (2\text{-}29)$$

where k represents the isothermal compressibility of the system and τ controls the strength of the coupling between the simulated system and the external pressure bath. This adjustable scaling factor helps to ensure that pressure converges to a stable value.

However, this technique has similar limitations to the velocity rescaling thermostat and thus more sophisticated extended system methods such as the Andersen barostat [45] have been developed. The Andersen barostat introduces an additional degree of freedom to the system which mimics the effect of a piston acting on the system. The simulated piston is designated a mass of Q which controls the frequency of volume oscillations. In both algorithms, the shape of the simulation cell is maintained thus imposing an isotropic constrain on the cell which is not always desirable. The Parrinello-Rahman barostat [46] expands on the design of the Andersen to allow for changes in both simulation cell size and shape when optimizing the pressure.

2.2.4 Thermodynamic Ensembles

Having established the means to control thermodynamic variables such as temperature and pressure in Chapter 2.2.3, it follows that specific combinations of these controls can be arranged to simulate real physical systems. These combinations of system controls are referred to as thermodynamic ensembles. The use of the term ensemble stems from the field of statistical mechanics in which an ensemble represents many virtual copies of a system, that when considered in concert, describe the possible states that a real system could exist in. Three commonly modeled ensembles in MD include the microcanonical (*NVE*), canonical (*NVT*), and isothermal-isobaric (*NPT*). The variables *N*, *V*, *E*, *T*, and *P* correspond to number of particles, volume, energy, temperature, and pressure respectively. In the *NVE* ensemble, no thermostat or barostat is applied and the system remains completely isolated from the outside – unable to exchange energy or particles with its environment. The *NVT* ensemble describes a closed system in which total energy is allowed to fluctuate and temperature is regulated using a thermostat. To remain in equilibrium, the system cannot exchange

particles with the outside but a weak coupling with a heat bath to regulate temperature is allowed. Lastly, the *NPT* ensemble enables volume relaxation through a weak coupling to an external pressure bath though the system remains closed to changes in particle number.

2.3 Convolutional Graph Neural Networks

Machine learning (ML) techniques are quickly growing in popularity as a way to accelerate materials discovery and design. They can offer energy and property predictions with near *ab-initio* accuracy at speeds that are orders of magnitude faster [47], [48], [49]. However, the application of these novel techniques to interesting material systems has not come without challenges. One major challenge for applying ML methods that is unique to the field of materials science is the heterogeneity in both size and shape of crystalline or molecular compounds. Typical ML algorithms operate on uniformly sized matrices of numerical features which do not lend themselves well to describing a periodic crystal that can have any number of atoms on its lattice.

In fact, the problem of developing appropriate ML descriptors to represent atomic systems has a rich literature of its own [50]. Such descriptors must adhere to five basic properties in order to represent a chemical system effectively: invariance with respect to spatial translation, invariance with respect to rotation, invariance with respect to the permutation of atomic indices, uniqueness, and continuity [51]. Translational and rotational invariance are crucial to represent dynamic systems – as the system evolves the descriptors should not change just because of a particle's location or orientation (barring any cooccurring change to the local environment). Atoms are commonly indexed by numerical indices and merely changing the order in which the atoms are referenced should never influence the value of a descriptor. As for uniqueness and

continuity, any rational representation must represent identical systems with identical descriptors and small changes to that system should correspond to a proportionally small change in the value of its descriptor. Additional properties such as memory compactness and computational efficiency are also desirable, but not necessarily required. Early attempts to represent atomic systems in a way that is compatible with the ML machinery include descriptors such as the Coulomb Matrix [52], Sine Matrix [53], Many-body Tensor Representation (MBTR) [54], and Smooth Overlap of Atomic Positions (SOAP) [50]. While each of these descriptors satisfies the five necessary properties, they tend to be limited in the size of the systems they can represent or the scope of unique elements they can operate on within a single model. These limitations motivated a novel way of framing the problem – not with uniform matrices, but with a much more flexible data structure, graphs.

Graphs are ubiquitous in computer science and conveniently offer a very intuitive way to represent molecules or crystals. The nodes of a graph represent individual atoms while the edges connecting nodes represent bonds. Each node and edge can hold a descriptor which represents the atom type and bond character respectively. This type of data structure is interpretable by convolutional neural networks (CNN) which have proven to be highly effective in learning from raw data sources such as the pixel values in an image [55]. The CNN is able to operate on irregularly sized inputs by leveraging two unique features: convolution layers and pooling layers. Convolution layers and hidden layers are applied to each node which output a representation of the local environment from the reference frame of each node. The pooling layers are used to condense the independent local environment representations into a single layer

which describes a global state for the entire graph. After pooling, additional hidden layers are inserted before the final output layer which ultimately provides the property prediction. A similar model architecture has been applied to problems such as computer vision [56], natural language processing [57], and molecular fingerprinting [58]. However, implementing and applying it to the task of material property prediction was first published by Xie and Grossman in 2018 [59]. Since the development of their initial model, other authors have used modified architectures and more expansive datasets to improve performance. The first variation to be released was the iCGCNN in 2020 which incorporates information from the Voroni tessellation of the crystal structure, three-body interactions with neighboring atoms, and optimizations regarding the representation of bonds [60]. Other notable advancements include the OGCNN [61] which encodes the molecular orbitals of each atom as a part of the descriptor and the GeoCGCNN [62] which explicitly considers the bond vector between each atom and its neighbors. In this work we employ a more recent implementation, CHGNet, developed by Deng et al. [63]. This model is pretrained on the entire Materials Project database [64] and is capable of predicting the forces acting on individual atoms in a structure which, by extension, enables direct geometry relaxation. The pretrained model is freely available on GitHub and includes a convenient Python interface.

2.4 Special Quasirandom Structures

Modeling realistic structural disorder is a key component to understanding high entropy material systems which have become an exciting field of research offering promising results in applications ranging from high temperature structural components [65] to energy storage [15]. One might assume that a trivial random choice algorithm to determine lattice site occupancy would be sufficient to represent a disordered phase.

However, this assumption is incorrect because the likelihood of unintentionally creating local correlations in any random cell, especially under periodic boundary conditions, is quite high. Therefore, we rely on a more intentional methodology which specifically minimizes local correlation between atom types known as the Special Quasirandom Structures method (SQS) [66], [67]. This approach has been shown to reproduce much more closely the distribution of site occupancies in real disordered systems.

While a finite representation of a continuous system will always be prone to deviations from complete disorder, the SQS method attempts to minimize this effect by prioritizing neighbors in the first and second shells. These close neighbors have the strongest influence on the central site and by deferring any correlations to distant neighbors, the impact of that correlation is minimized. This technique is particularly effective in minimizing the error of periodic systems.

The SQS algorithm implementation in the *sqsgen* software package [66] employed in this work relies on computing the Warren-Cowley short range order parameter to quantify disorder (Equation 2-30).

$$\alpha_{AB}(\sigma) = 1 - \frac{N_{AB}(\sigma)}{NMx_Ax_B} \qquad (2\text{-}30)$$

Where M represents the number of neighboring sites, N_{AB} represents the number of A-B atom pairs, and x_A and x_B indicate the mole fractions of atom types A and B respectively. A value approaching the limit of 1 corresponds to a clustered alloy system, 0 indicates disorder, and -1 corresponds to periodic ordering. This ordering parameter can be generalized over specific neighbor shells to compute different ordering parameters for each neighbor shell. This is desirable to control the radius within which one is concerned about correlation effects. When considering candidate structures, an

objective function must be defined to quantify the solutions of best fit. This objective function takes the following form:

$$O(\sigma) = \sum_i w^i \sum_{\zeta,\eta} p_{\zeta\eta} \left| \tilde{\alpha}^i_{\zeta\eta} - \alpha^i_{\zeta\eta}(\sigma) \right| \qquad (2\text{-}31)$$

Where w^i is a weighting parameter controlling the influence each neighbor shell has on the disorder parameter, $\tilde{\alpha}^i_{\zeta\eta}$ is the target short range order parameter, and the subscripts ζ and η represent a generalized pair of atom types.

Despite having a quantifiable objective function to minimize, the problem of SQS generation cannot employ robust minimization methods such as steepest descent or conjugate gradient to rapidly find a local minimum. Instead, the algorithm generates a vast number of candidate structures which are all evaluated and screened out of consideration if their objective function is not the lowest yet found. This technique is simple to parallelize, but scales poorly with simulation cell size. Any increase in the number of lattice sites is rapidly outpaced by the growth of the number of neighboring correlations. This necessitates screening a larger number of candidate structures before the user can have confidence that an optimal solution has been found. SQS generation is crucial in the analysis of high entropy Li-oxide cathode materials presented in Chapter 7 of this work.

CHAPTER 3
ENERGETICS AND DIFFUSION KINETICS OF POINT DEFECTS IN $MnCr_2O_4$ SPINEL FROM FIRST PRINCIPLES[*]

3.1 Background

As manufacturers of internal combustion engines strive to achieve greater performance and efficiency, they design their engines to operate at higher temperatures (upwards of 700 °C), which narrows the range of suitable materials. At these elevated temperatures, corrosion damage can lead to mechanical failure even for alloys designed specifically to resist it. This design challenge is exacerbated by the harsh environment, particularly the corrosive gases from incomplete combustion reactions, including water vapor, carbon dioxide, and hydrocarbons. One class of alloy commonly used for applications in this space due to its robust mechanical properties, corrosion resistance, and affordability is the austenitic stainless steels [5], [68], [69], [70], [71]. Austenitic stainless steels contain high concentrations of chromium, which aids in corrosion inhibition, and manganese, thereby stabilizing the austenitic phase over a wider temperature range [71], [72], [73].

Experimental observations have shown that the oxide film which grows on top of these alloys when exposed to elevated temperatures is multilayered and consists of manganese oxide, chromium oxide, and a spinel structured manganese chromate with $MnCr_2O_4$ stoichiometry [7], [74]. The experimental work of Abdallah et al. [7], in which 21-2N alloy samples were exposed to a CO_2 environment at a temperature of 700 ºC, confirms that the spinel layer forms in direct contact with the bulk alloy. This observation

[*] The work described in this chapter has been published in Ullberg, R. S., Wu, X., Tonks, M. R., & Phillpot, S. R. (2023). Energetics and diffusion kinetics of point defects in MnCr2O4 spinel from first principles. *Journal of Physics and Chemistry of Solids*, *181*, 111519.

is consistent with thermodynamic calculations produced as part of the same work which predict $MnCr_2O_4$ to be the most thermodynamically stable oxide out of the possible MnO, Mn_3O_4, MnO_2, Cr_2O_3, and $MnCr_2O_4$ compositions. Thus, oxidation must be mediated by the spinel with either the flow of metallic species from the alloy to react with an oxidant or the flow of the oxidant towards the alloy, or both. In the latter case, the oxidant must first pass through an outermost layer of manganese oxide and an intermediate layer of chromium oxide. Therefore, to fully understand the dynamic process of oxidation in these austenitic steel alloys at the atomic level, we must understand the thermodynamics and kinetics of defects in the $MnCr_2O_4$ spinel phase.

Despite a wide range of published work concerning the thermodynamics and kinetics of point defects in spinel type structures, no study has applied ab-initio methods to perform a comprehensive analysis of the cationic and anionic defect processes relevant to high-temperature corrosion in $MnCr_2O_4$. In fact, much of the available literature is focused on radiation damage induced defect clusters in the canonical $MgAl_2O_4$ spinel [75], [76], [77], [78], [79], [80]. While this work is valuable in its own right, the defect configurations relevant to nuclear applications are not necessarily the most relevant when considering oxidation processes. To examine the behavior of more conventional and generalizable defect configurations in spinel structures, the work of Muhic et al. [81] is particularly relevant in that it focuses on determining relative barrier heights for vacancy mediated diffusion of cations in three ferritic spinels. The only literature focusing on defect behavior expressly in the $MnCr_2O_4$ system is a purely experimental paper by Gilewicz-Wolter et al. [82]. They found that Mn was the most mobile species with nearly twice the self-diffusion coefficient of Cr, and that at a

temperature of 1073 K volume diffusion was the primary mechanism for Mn diffusion, while Cr diffusion utilized grain boundaries and other high-diffusivity pathways. The conclusions drawn from their work help us to understand why the Mn-rich outer oxide layer forms so rapidly atop the spinel, but a detailed understanding of the precise atomistic mechanisms facilitating this behavior is still lacking. Theoretical calculations are well suited in this regard to identify the most favorable defect types in the structure and to evaluate their mobility between specifically curated lattice sites.

In this work, we calculate the formation energies and migration barrier heights of cationic and anionic point defects in $MnCr_2O_4$ spinel using density functional theory. We consider the effect of defect charge state and the influence of temperature as it applies to the thermodynamic favorability of formation and the mobility of each defect type. The results of this study provide a comprehensive account of the dynamic defect behaviors present in this spinel structure with particular relevance to the atomistic mechanisms involved in oxide film formation on austenitic steel substrates.

3.2 Methodology and Crystal Structure

3.2.1 Methodology

All density functional theory (DFT) calculations in this work are performed using the Vienna Ab initio Simulation Package (VASP) [83], [84], [85]. Projector augmented plane wave (PAW) pseudopotentials [86] are used to describe interactions between core and valence electrons. The pseudopotentials for Mn and Cr are partial valence models simulating the 13 and 12 outermost electrons as valence respectively, while the pseudopotential for O includes all 6 electrons in the valence shell explicitly. The generalized gradient approximation (GGA) and Perdew-Burke-Ernzerhof (PBE) functional [23] are used to describe exchange correlation energies. Due to the

limitations of DFT with regards to modeling the localization of *d* electrons [35], GGA+U is employed using U values of 3.7 eV for Mn and 3.9 eV for Cr, adopted from prior works [64], [74], [87]. A plane-wave cutoff energy value of 520 eV is used for all calculations following a convergence study over the range of 300 – 600 eV. The simulation cell for each calculation is selected to be the conventional 56 atom unit cell following a convergence study over supercell sizes which showed a difference of just 0.02 eV in Mn vacancy formation energy for a non-conventional simulation cell of 378 atoms, which was the largest system size tested.

A k-point convergence study found that a Γ-point centered 5 x 5 x 5 Monkhorst-Pack mesh [88] provides reasonable computation speed and appropriate precision. Spin polarization is enabled in all calculations with magnetic moments being initialized to ± 5.0 μ_B for both Mn and Cr (alternating the sign for each atom) and 0.6 μ_B for O to create an antiferromagnetic ordering on both the Mn and Cr sublattices, such that the system has zero net magnetic moment. We found this ordering to be favorable relative to both a layered antiferromagnetic ordering and a ferromagnetic ordering. The initial conditions for magnetic moment values are adopted from Jain et al. [64] and converged to ± 4.57 μ_B, ± 2.97 μ_B, and < 0.07 μ_B for Mn, Cr, and O respectively in the defect-free structure. Geometry relaxations employ a Gaussian smearing scheme with a smearing width of 0.05 eV, as is recommended by the VASP documentation for simulations of insulating materials. Total energy values are computed using single-point calculations of the optimized structures in which the smearing scheme is switched to the tetrahedron method with Blöchl corrections [89].

Defect formation energies in the neutral charge state are calculated using the standard supercell approach:

$$E_F = E_{def} - E_{ref} \pm n\mu \quad (3\text{-}1)$$

Where E_{def} is the total energy of the simulation cell containing the defect, E_{ref} is the total energy of the defect-free simulation cell, n is the number of defects present, and μ is the chemical potential of the defect species. The $n\mu$ term should be added for vacancy type defects and subtracted for interstitial type defects. The effect of charge state on defect formation energies is evaluated using the *sxdefectalign* software tool [90]. This code implements the Freysoldt/Neugebauer/Van de Walle (FNV) method [91], [92] which calculates a correction energy term to counteract the effect of self-interaction for charged defects in a periodic simulation cell. This correction energy term is incorporated in Equation 3-2 and serves as a more generalizable form of the supercell approach for neutral defects presented in Equation 3-1.

$$E_F^q = E_{def}^q - E_{ref} - \sum_i n_i\mu_i + qE_{Fermi} + E_{corr} \quad (3\text{-}2)$$

Here E_{def}^q is the total energy of the simulation cell containing the charged defect, E_{ref} is the total energy of the charge neutral defect-free simulation cell, n_i is the number of atoms of species i which contribute to the defect, μ_i is the chemical potential of each species i, q is the defect charge state, E_{Fermi} is the Fermi energy with respect to the vacuum level, and E_{corr} is the correction energy term computed by the FNV method.

In this work, chemical potentials are adjusted to replicate the conditions of an oxidizing environment at a temperature of 1000 K and an oxygen partial pressure of 0.2 atm. Chemical potentials are determined using the methodology proposed by Finnis et al. [93] which has been widely established as the standard for publications in the field of

ab-initio thermodynamics [94], [95], [96], [97], [98], [99], [100]. The experimentally determined enthalpy and entropy, tabulated as a function of temperature, is taken from the JANAF thermochemical tables [101]. Using these experimental references, ΔG of each chemical species can be calculated directly for the target temperature using Equation 3-3.

$$\Delta G = \Delta H - T\Delta S \quad (3\text{-}3)$$

Because ΔG is equivalent to chemical potential in the context of this work, the value computed from experimental data can be added directly to the ab-initio calculated chemical potential acting as a correction factor which incorporates the effects of finite temperature. One technical detail which has a large effect on the magnitude of the temperature correction is the choice of reference state for the cationic species. For oxygen, it is sensible to use an O_2 molecule to derive the chemical potential of an individual oxygen atom, but for cationic species one may choose to use either the metallic reference state of the pure metal or that metal's most favorable oxide form to derive a chemical potential. The impact of this choice is visualized in Figure 3-1. From inspection, it is clear that choosing the metallic reference state (circular markers) produces a more negative change in chemical potential at elevated temperatures when compared to the oxide reference state (triangular markers). In this work we choose to use the metal's pure metallic reference state to derive chemical potential.

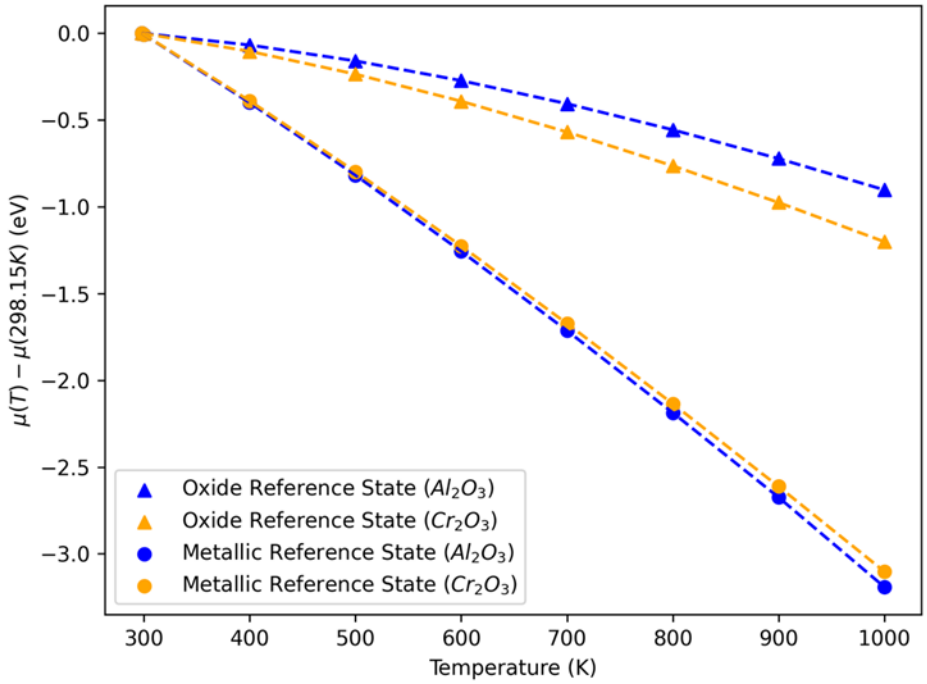

Figure 3-1. Total change in chemical potential of Al_2O_3 and Cr_2O_3 using the oxide reference state and metallic reference state methodologies to treat the cationic species.

Migration energy barriers are determined using the climbing image nudged elastic band method (CI-NEB) as implemented in the VASP transition state tools (VTST) developed by the Henkelman group [102], [103]. Each CI-NEB calculation is interpolated over 7 intermediate images to achieve high resolution diffusion profiles. A spring constant of 5.0 eV/Å^2 assigned to each of the virtual springs connecting the intermediate images proved to be adequately flexible for full relaxation along each migration pathway.

3.2.2 Crystal Structure

The spinel family of structures are classified under the $Fd\bar{3}m$ space group (International Number 227, Schöenflies O_h^7) and have the general formula AB_2O_4. The 56-atom conventional unit cell is composed of 8 formula units which are arranged on a face-centered-cubic (FCC) lattice where each lattice point has a basis of two formula

units. The oxygen sublattice is arranged in a pseudo-cubic close packed configuration. A-site cations occupy 8 of the 64 available tetrahedrally coordinated interstices while B-site cations occupy 16 of the 32 available octahedral interstices. The arrangement of A-site cations forms a diamond cubic sublattice and each is 4-fold coordinated along the <111> directions to oxygen atoms. There are thus 8 A-site centered oxygen tetrahedra, as shown in blue in Figure 3-2. Each B-site cation is 6-fold coordinated to oxygen along the <111> directions [104]. Thus, there are 16 B-centered oxygen octahedra, as shown in green in Figure 3-2. The A-site tetrahedra are arranged such that there is no direct contact between them. Nearest neighbor tetrahedra are separated by octahedral cages with no central cations, lying along <111>. The B-site octahedra are edge-sharing and chain indefinitely in-plane along <110>. The linkage between A-site tetrahedra and B-site octahedra is via corner-sharing with each corner of a tetrahedron being connected to the corner of an octahedron and each corner of an octahedron being connected to a corner of a tetrahedron. A similar analysis of polyhedral connectivity can also be conducted for the unoccupied octahedral and tetrahedral sites. Illustrations which compare the connectivity of the occupied and vacant sublattices are presented in Figure 3-3. We observe that the vacant octahedral sites are edge-sharing along <110> type directions, while the vacant tetrahedral sites have no direct connection with each other but are corner-sharing with the vacant octahedra. When considering the connectivity of both the occupied and unoccupied sites, we find that the vacant tetrahedral sites are face-sharing with Cr-occupied octahedral sites, and that the vacant octahedral sites are both edge-sharing with Cr-occupied octahedral sites and face-sharing with Mn-occupied tetrahedral sites. The vacant octahedral site is larger than the vacant tetrahedral sites

and thus affords greater open volume for atoms migrating through it. It then follows that the Mn-occupied site sharing a face with such a large structural vacancy is expected to have a greater mobility than the Cr-occupied site which is face-sharing with the smaller unoccupied tetrahedra. NEB calculations which support this simple crystallographic argument are presented in Chapter 3.3.5.

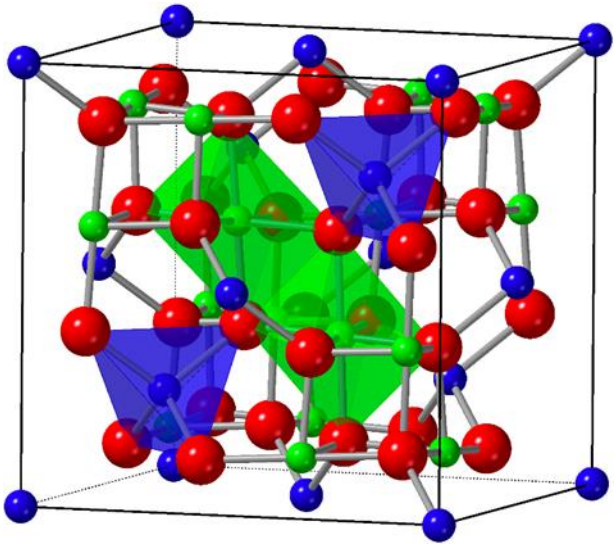

Figure 3-2. Conventional Mn-centered unit cell of $MnCr_2O_4$ displaying the tetrahedrally coordinated Mn (blue), octahedrally coordinated Cr (green) and oxygen (red).

There are two natural choices of origin with high point symmetry, one with $\bar{4}3m$ point symmetry centered on an A site (Mn), the other with $\bar{3}m$ symmetry centered on a structural vacancy. Figure 3-2 depicts the spinel unit cell with the A-centered $\bar{4}3m$ origin centered, which is the convention used throughout this work. Using this reference frame, the Wyckoff positions of A-sites, B-sites and oxygen are respectively 8a, 16d, and 32e.

Depending on the composition of a particular spinel, some degree of cation disorder, often termed inversion, may be supported. A fully inverted spinel is one in which all tetrahedrally coordinated sites are replaced with B cations leaving one half of the octahedrally coordinated sites occupied with A cations and the other half occupied

with B cations. In the canonical $MgAl_2O_4$ spinel, naturally sourced samples contain almost no inversion, but samples which are synthetically grown or are annealed at temperatures above 800 ºC exhibit a high degree of inversion [105]. The distribution of these inverted sites in samples of $MgAl_2O_4$ which do have a high degree of inversion has been shown to be largely disordered in measurements conducted via nuclear magnetic resonance (NMR) and electron spin resonance (ESR) [105], [106]. For the $MnCr_2O_4$ spinel under investigation in this work, the total energy of multiple structures containing various degrees of inversion is evaluated using DFT calculations. We find a monotonic increase in energy with increasing inversion which indicates that there is no support for inversion in the structure under ab-initio conditions. Kjellqvist et al. [107] also arrive at the conclusion that very little inversion is supported in naturally occurring $MnCr_2O_4$. Therefore, the defect-free reference state used for all calculations is non-inverted; that is, 'normal' spinel. A fuller discussion of the crystallography of this structural family can be found in the work of Sickafus et al. [108].

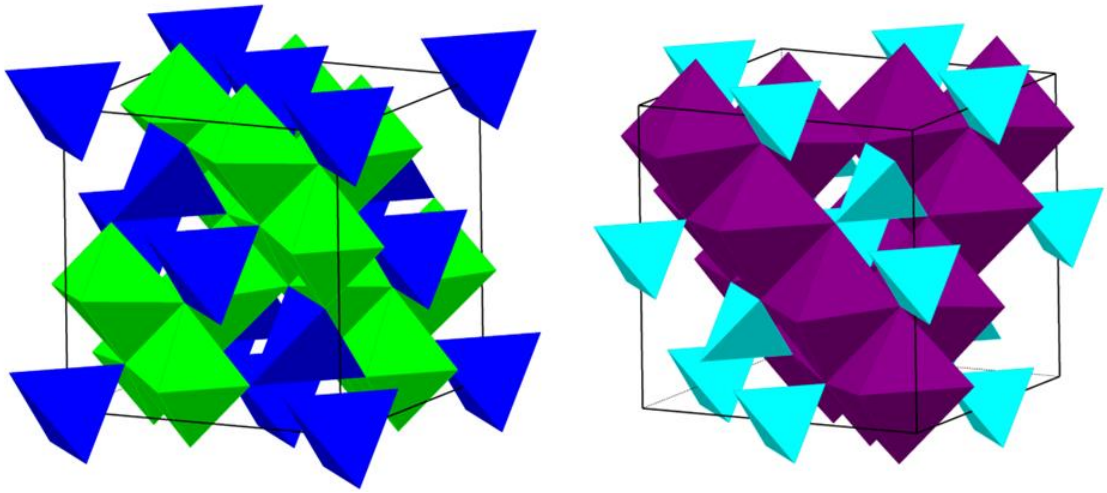

Figure 3-3. (Left) Polyhedral model of the occupied octahedral and tetrahedral lattice sites. Cr displayed in green, and Mn displayed in blue. (Right) Polyhedral model of the unoccupied octahedral and tetrahedral lattice sites. Octahedra displayed in purple and tetrahedra displayed in cyan.

3.3 Results

3.3.1 Bulk Properties

To benchmark our computational methodology, we compare fundamental properties of the bulk $MnCr_2O_4$ crystal with other DFT calculations available in materials databases and experimental literature. The results presented in Table 3-1 show close agreement across all sources, with small differences being attributed to unique choices of functional, k-point mesh density, and convergence criteria.

Table 3-1. Lattice parameter a_0, bond lengths Cr-O and Mn-O, magnetization per ion μ_{Cr} and μ_{Mn}, and band gap E_g of bulk $MnCr_2O_4$ as calculated in this work compared to quantum materials databases and experiment.

Property	**This Work**	**Materials Project** [64]	**Open Quantum Materials Database** [109]	**Experiment** [110]
a_0 (Å)	8.61	8.59	8.50	8.44
Cr-O (Å)	2.04	2.04	2.02	-
Mn-O (Å)	2.07	2.07	2.04	-
μ_{Cr} (μ_B/Cr ion)	2.97	2.97	-	-
μ_{Mn} (μ_B/Mn ion)	4.56	4.57	-	-
E_g (eV)	2.55	2.20	2.50	-

The largest difference between this work and similar theoretical calculations is in the prediction of band gap. Our value of 2.55 eV is in close agreement with the value of 2.50 eV published in the Open Quantum Materials Database (OQMD) but is higher than the Materials Project (MP) prediction by 0.35 eV (14.7 %). Despite this difference, all DFT sources predict that the bulk crystal is an insulator. Although there is no experimental value of band gap available for $MnCr_2O_4$ to compare to, the agreement between multiple DFT sources supports the conclusion that the material is in fact insulating. Additionally, each source predicts the magnetic ordering to be antiferromagnetic, with all cation sites having their magnetic moments oriented in an opposing direction, such that the magnetic moments on both the Mn and Cr sublattices

are zero. To confirm that our electronic structure calculations are well behaved, the total and orbital-projected density of states are illustrated in Figure 3-4. Below the valence band, oxygen's p-orbital dominates the available states while chromium's d-orbital dominates those above the conduction band.

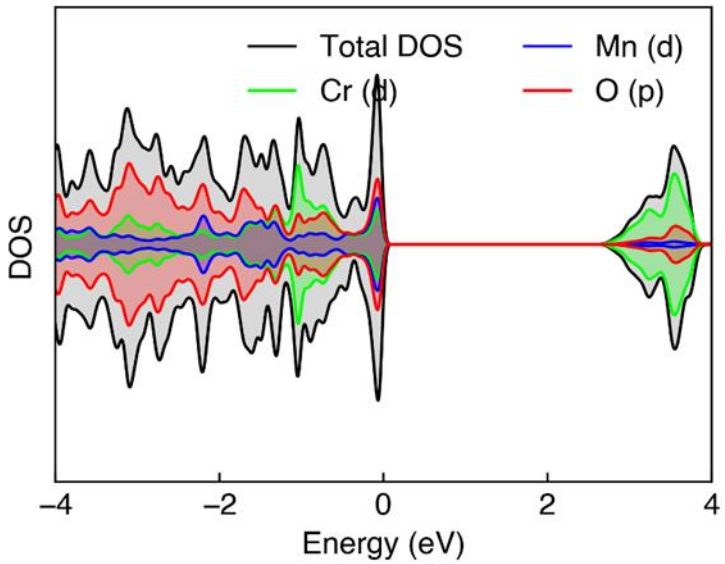

Figure 3-4. Density of states for a conventional $MnCr_2O_4$ unit cell calculated with GGA+U.

3.3.2 Vacancy Defect Formation

Isolated vacancy defects of each chemical species in $MnCr_2O_4$ are evaluated for thermodynamic favorability across all oxidation states up to and including their expected formal charge. The formation energies for the neutral and charged vacancies of Mn, Cr, and O are shown in Table 3-2.

Table 3-2. Formation energies of isolated vacancy defects for each chemical species in $MnCr_2O_4$. The lowest values for each species are bolded.

Defect	Formation Energy at VBM (eV) 0 K / 1000 K	Formation Energy at CBM (eV) 0 K / 1000 K
V_{Mn}^{x}	3.59 / 3.20	3.59 / 3.20
$V_{Mn}^{\prime}$	4.23 / 3.84	1.68 / 1.29
$V_{Mn}^{\prime\prime}$	5.77 / 5.38	**0.66 / 0.27**
$V_{Mn}^{\prime\prime\prime}$	10.2 / 9.77	2.50 / 2.11
V_{Cr}^{x}	3.98 / 3.67	3.98 / 3.67
$V_{Cr}^{\prime}$	4.98 / 4.67	2.43 / 2.12
$V_{Cr}^{\prime\prime}$	6.96 / 6.65	**1.85 / 1.54**
$V_{Cr}^{\prime\prime\prime}$	10.1 / 9.83	2.47 / 2.16
V_{O}^{x}	5.15 / 4.32	5.15 / 4.32
$V_{O}^{\bullet}$	**3.88 / 3.05**	6.44 / 5.61
$V_{O}^{\bullet\bullet}$	4.09 / 3.26	9.19 / 8.36

The dominant regions of each defect charge state reported in Table 3-2 can be seen as defect transition levels in Figure 3-5 below. The abscissa spans the width of the 2.55 eV bandgap from DFT, and each line plots the formation energy of a particular defect charge state at any point in the bandgap. Changes in slope correspond with changes in the most favorable defect charge state.

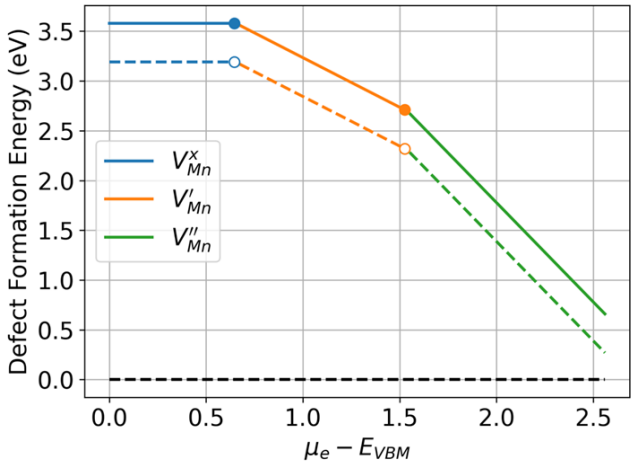

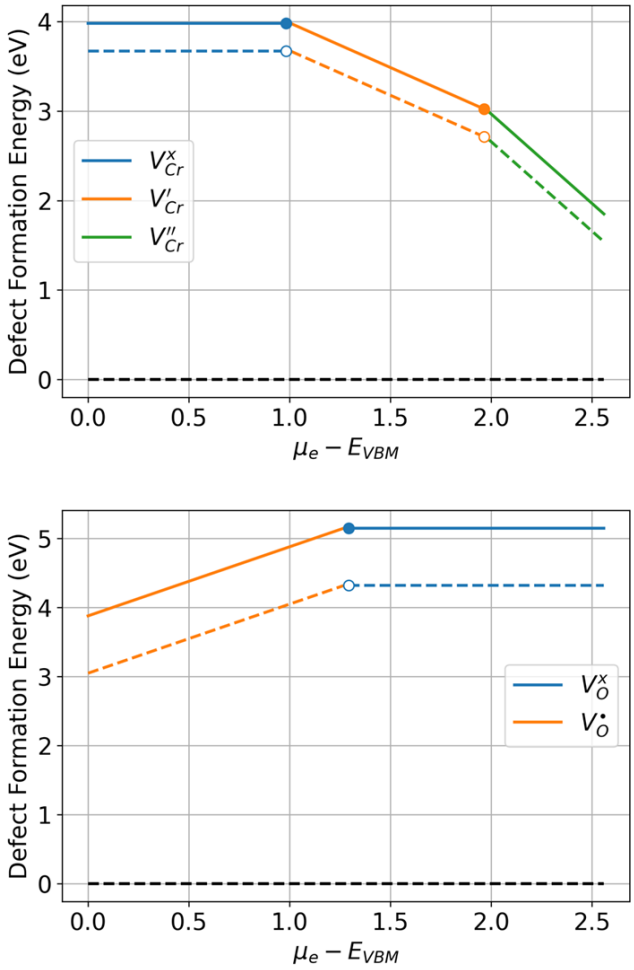

Figure 3-5. Defect formation energy as a function of position in the bandgap for unique charge states of a Mn vacancy (top), Cr vacancy (middle), and O vacancy (bottom). Changes in slope correspond with changes in the most favorable charge state. Solid lines represent the 0 K condition and dashed lines represent the 1000 K condition.

The formation energies of Mn and Cr vacancies as a function of charge state are very similar to each other. Both species experience transitions from the neutral state to the 1^- state near the valence band maximum (VBM) and transitions from the 1^- state to the 2^- state near the conduction band minimum (CBM). In its most favorable charge state and temperature condition, the Mn vacancy has a formation energy of 0.27 eV. This is a reduction of 2.93 eV (92 %) relative to the neutral state. Cr's lowest possible formation energy is 1.54 eV, which occurs under the same charge and temperature conditions,

but is only a reduction of 2.13 eV (58 %) relative to the neutral state. As an anionic species, O vacancy defect transition levels trend opposite to cationic Mn and Cr. The O vacancy has its lowest formation energy at the VBM and transitions from the 1^+ state to the neutral state at 1.3 eV into the bandgap. Based on our methodology to adjust chemical potential as a function of temperature introduced in Chapter 3.2.1, we find that O defects are more sensitive to changes in temperature than cationic defects. Under ab-initio conditions, the lowest O vacancy formation energy value is 3.88 eV, but at an elevated temperature of 1000 K and a partial pressure of 0.2 atm, the formation energy is reduced by 0.83 eV (21 %) to 3.05 eV. Furthermore, it is rather unexpected that the 2^+ defect charge state is never favorable for the oxygen vacancy in this system. To explain this finding, we calculated defect transition levels of oxygen vacancies in similar spinels and other related oxides to identify in which conditions the 2^+ defect charge state disappears. In analyzing these related defect transition levels, we find that it is the occupancy of a spinel's cationic A or B sites by a transition metal which complicates the expected defect behavior. In the case of $MgAl_2O_4$, which contains cations with a consistent valence, we observe that defects of each species are most favorable in their formal charge states. However, once either the A site or B site is replaced with a transition metal, as we tested using $MnAl_2O_4$ and $MgCr_2O_4$ respectively, the 3^- charge of the B site vacancy and the 2^+ charge of the O vacancy disappear.

3.3.3 Interstitial Defect Formation

In addition to isolated vacancy defects, four configurations of interstitial defects were analyzed for each chemical species in $MnCr_2O_4$. Three configurations correspond directly to Wyckoff positions of unoccupied sites in the lattice (8a, 32e, 16d). The fourth configuration is a dumbbell-type interstitial which is centered on a lattice site normally

occupied by the species of the interstitial defect and splits along a <110> type direction. This split type configuration has been reported to be favorable for both cationic and anionic interstitials in prior work on $MgAl_2O_4$ and $MgGa_2O_4$ spinels [75], [78], [80]. The three Wyckoff aligned configurations are shown in Figure 3-6.

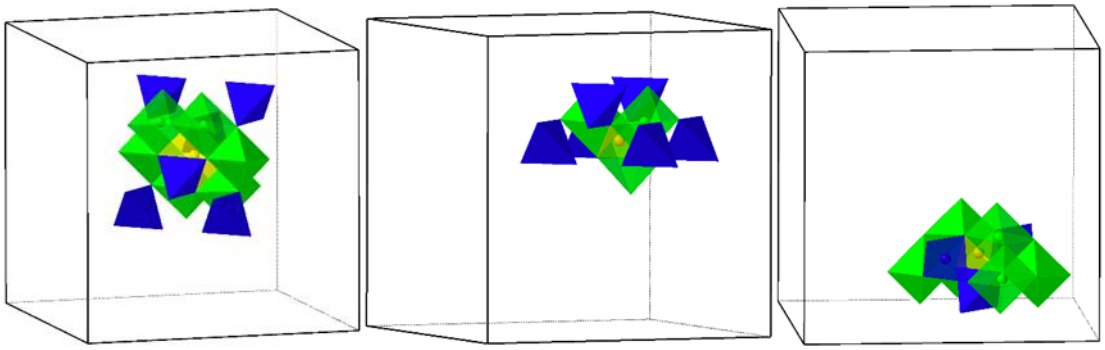

Figure 3-6. Position of the interstitial ion (colored in yellow) corresponding to 8a (left), 32e (center), and 16d (right) Wyckoff positions.

The 8a site lies in the structural vacancy between the faces of two adjacent Mn tetrahedra. The 32e site is positioned on the face of a Cr octahedron and coordinates to form a tetrahedral cage with neighboring O. The 16d site sits directly below the 32e site along the z-axis and occupies a structural vacancy between adjacent Mn tetrahedra, much like the 8a site. However, unlike the 8a site, the 16d site is coordinated more closely with Cr than Mn having nearest neighbors at 1.86 Å (Cr) and 2.15 Å (Mn) relative to 3.04 Å (Cr) and 1.86 Å (Mn) for 8a. The formation energies of each interstitial configuration are presented in Table 3-3.

Table 3-3. Formation energies of isolated interstitial defects for each chemical species in $MnCr_2O_4$. The lowest values for each species are bolded.

Defect	Formation Energy (eV) 0 K / 1000 K
Mn_{8a}^{x}	7.06 / 7.45
Mn_{32e}^{x}	12.9 / 13.3
Mn_{16d}^{x}	9.28 / 9.67
$Mn_{<110>}^{x}$	**6.22 / 6.61**
Cr_{8a}^{x}	**7.43 / 7.74**
Cr_{32e}^{x}	15.9 / 16.2
Cr_{16d}^{x}	11.5 / 11.8
$Cr_{<110>}^{x}$	7.95 / 8.26
O_{8a}^{x}	2.05 / 2.88
O_{32e}^{x}	7.21 / 8.04
O_{16d}^{x}	2.67 / 3.50
$O_{<110>}^{x}$	**1.59 / 2.42**

For Mn and O, the <110> split configuration is preferred relative to any of the single-occupancy configurations. This trend is consistent with prior work on $MgAl_2O_4$ [75], [77]. However, Cr favors forming interstitials in the 8a configuration rather than the <110> by a margin of 0.52 eV. Additionally, it is observed that the formation of O interstitials is strongly favored over cationic interstitials under both ab-initio conditions and at elevated temperature and pressure. The effect of defect charge state for the most favorable interstitial configurations of each species are shown in Table 3-4 and Figure 3-7.

Table 3-4. Formation energies of isolated interstitial defects for each chemical species in $MnCr_2O_4$. The lowest values for each species are bolded.

Defect	Formation Energy at VBM (eV) 0 K / 1000 K	Formation Energy at CBM (eV) 0 K / 1000 K
$Mn^{x}_{<110>}$	6.26 / 6.65	6.26 / 6.65
$Mn^{\bullet}_{<110>}$	4.15 / 4.54	6.52 / 6.91
$Mn^{\bullet\bullet}_{<110>}$	**2.83 / 3.22**	7.58 / 7.97
$Mn^{\bullet\bullet\bullet}_{<110>}$	3.94 / 4.33	11.1 / 11.5
Cr^{x}_{8a}	7.43 / 7.74	7.43 / 7.74
$Cr^{\bullet}_{8a}$	6.11 / 6.42	8.47 / 8.78
$Cr^{\bullet\bullet}_{8a}$	**5.51 / 5.82**	10.3 / 10.6
$Cr^{\bullet\bullet\bullet}_{8a}$	6.14 / 6.45	13.3 / 13.6
$O^{x}_{<110>}$	**1.59 / 2.42**	**1.59 / 2.42**
$O'_{<110>}$	4.89 / 5.72	2.51 / 3.34
$O''_{<110>}$	8.46 / 9.29	3.71 / 4.54

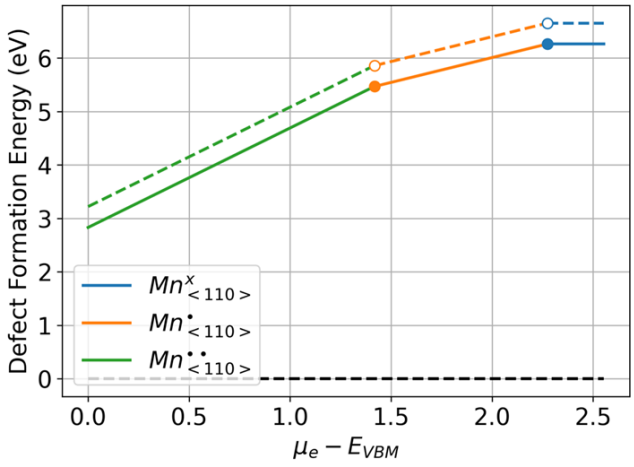

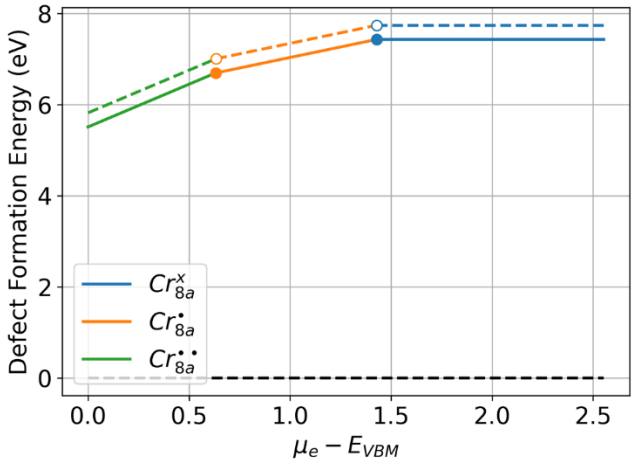

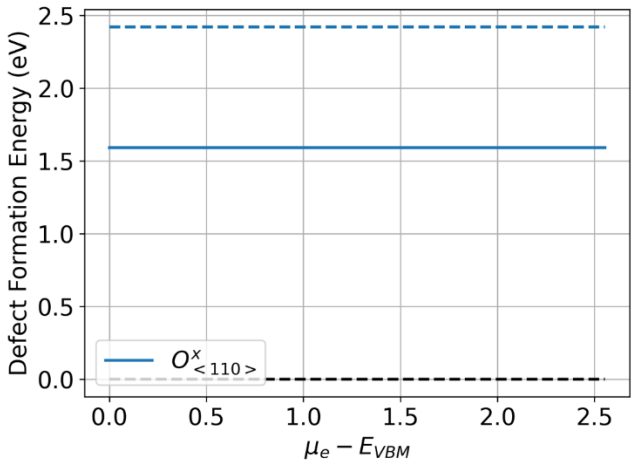

Figure 3-7. Formation energy as a function of position within the bandgap for the $Mn_{<110>}$ split interstitial (top), Cr_{8a} interstitial (middle), and $O_{<110>}$ split interstitial (bottom).

Charged cationic interstitials have lower formation energies than their neutral counterparts. Both Mn and Cr prefer to form interstitials in the 2^+ charge state and achieve a minimum value at the VBM. The interstitial formation energies of Mn and Cr are reduced by 3.43 eV (51.6 %) and 1.92 eV (24.8 %) respectively relative to their neutral conditions under the environmental 1000 K conditions. Additionally, both cations experience transitions in charge state favorability from 2^+ to 1^+ and ultimately from 1^+ to neutral at the CBM. Oxygen forms interstitial defects most readily in the neutral state throughout the bandgap.

3.3.4 Antisite and Substitution Defect Formation

As discussed briefly above, one feature of spinels is their propensity to support cation disorder, otherwise known as structural inversion. This phenomenon of structural inversion refers to the swapping of A and B cation sites without diverging from the nominal AB_2O_4 stoichiometry. In addition to stoichiometrically stable inversion, the chemical complexity of ternary oxides affords more opportunities to form substitution type defects. To assess the likelihood of inversion for the specific case of $MnCr_2O_4$

spinel, we calculate the formation energy of a single antisite defect which represents the lowest degree of inversion. We report antisite defects to have a formation energy of 1.89 eV which increases linearly with the number of antisite defects. This indicates that there is a significant barrier to inversion for this particular spinel composition. In Table 3-5 and Figure 3-8 we report the formation energy of Mn_{Cr} and Cr_{Mn} type substitution defects in their likely charge states as a function of position in the bandgap. Note that because antisite defects retain the stoichiometry of the bulk structure we do not anticipate any non-neutral defect charge state to be more favorable whereas substitution type defects change the composition of the material which can induce net charges on defect sites. Furthermore, we do not report on the effect of elevated temperature and pressure for these defect types because the only change from purely ab-initio conditions would be due to the differences in the adjustment of the chemical potentials of Mn and Cr which is small (< 0.1 eV). In Figure 3-8 it is evident that there is a distinct asymmetry between the favorability of Mn_{Cr} and Cr_{Mn} type substitutions. Interestingly, we observe that the Mn_{Cr} defect has a negative formation energy in the 1^+ charge state which implies that Mn may spontaneously occupy a vacant Cr site. Cr_{Mn} type defects are not spontaneous and are found to be most favorable in the 1^- charge state with a formation energy of 1.29 eV. Additionally, by inspecting the favorable charge states of each defect it can be inferred that the formal charges of Mn and Cr are 2^+ and 3^+ respectively as is expected in this AB_2O_4 composition.

Table 3-5. Effect of charge state on Mn_{Cr} and Cr_{Mn} type substitution defects. The lowest values for each defect type are bolded. All values are presented for the 0 K condition.

Defect	Formation Energy at VBM (eV)	Formation Energy at CBM (eV)
Mn_{Cr}^{x}	0.69	0.69
$Mn_{Cr}^{\prime}$	2.39	**-0.17**
$Mn_{Cr}^{\bullet}$	-0.03	2.52
Cr_{Mn}^{x}	2.01	2.01
$Cr_{Mn}^{\prime}$	4.20	1.65
$Cr_{Mn}^{\bullet}$	**1.30**	3.85

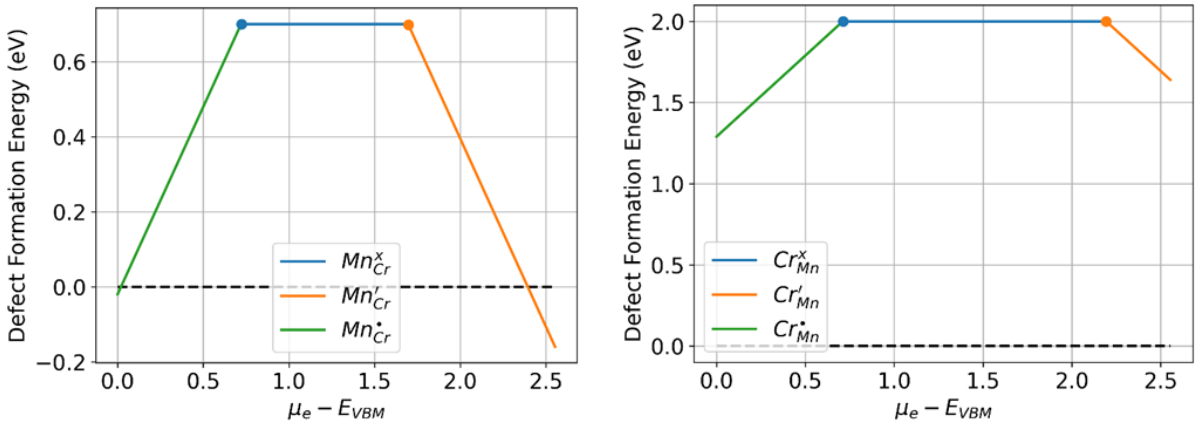

Figure 3-8. Defect formation energy as a function of position in the bandgap for Mn_{Cr} and Cr_{Mn} type substitution defects.

3.3.5 Vacancy Mediated Migration

Based on the results presented in Chapter 3.3.2, the vacancy formation energies of all three species are similar (within 1.5 eV of each other in the neutral charge state), and thus vacancies of each need to be considered when analyzing possible migration mechanisms. The vacancy mediated diffusion pathways for each species moving along its own sublattice are visualized in Figure 3-9.

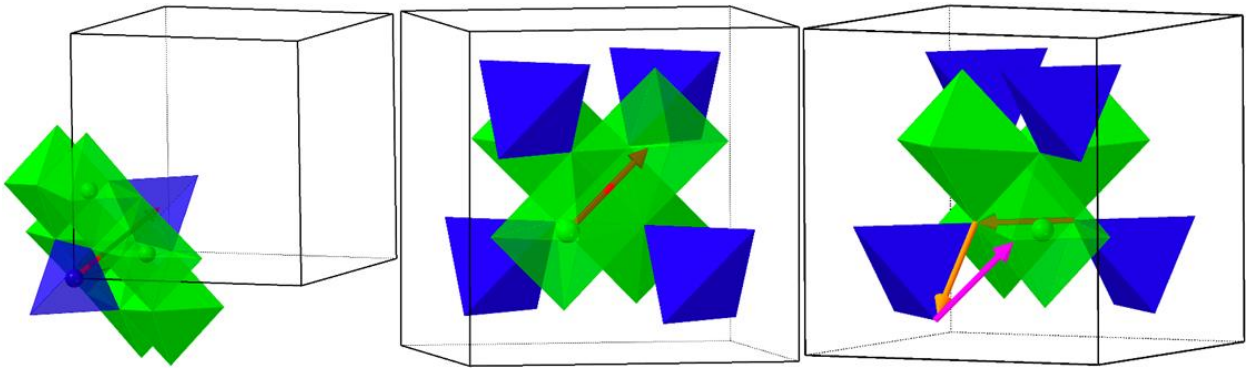

Figure 3-9. Migration pathways for vacancy mediated Mn (left), Cr (middle), and O (right) diffusion.

The migration of Mn along its sublattice to a vacant Mn site passes through the face of two tetrahedra and the center of an unoccupied octahedron along a <111> direction. This pathway is largely unimpeded, which would suggest a low migration barrier. In contrast, the migration of Cr along its sublattice in a <110> direction to an existing Cr vacancy passes through the connected edge of two octahedra creating a steric hindrance at the center of the pathway. The migration of any O atom along its sublattice may proceed in three distinct ways: O can move in the [110] direction along the edge of a Mn tetrahedron, in the [101] direction along the shared edge between two Cr octahedra, or in the [011] direction from the corner of a Mn tetrahedron to the corner of a Cr octahedron.

The NEB migration profiles for all of these Mn, Cr, and O pathways are shown in Figures 3-10 and 3-11. To understand the relative diffusivities of these species it is essential to compare their peak barrier heights. In their most favorable charge states, the barrier of Mn is by far the lowest at 0.45 eV, with Cr the highest at 2.3 eV, and O being slightly lower at 2.1 eV.

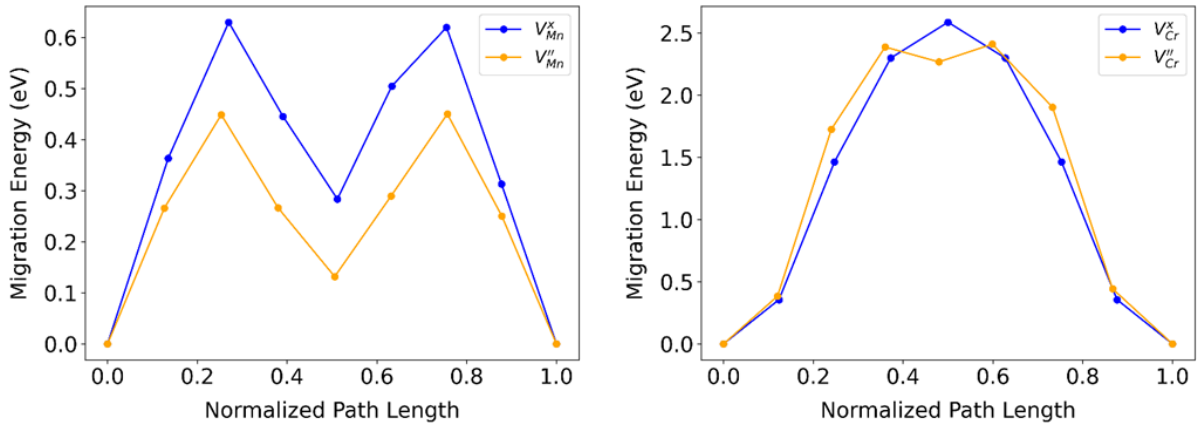

Figure 3-10. Migration energies for vacancy mediated Mn diffusion (left) and Cr diffusion (right).

To provide a rationale for the distinct migration profile shapes, we refer back to Figure 3-9. The two peaks present in the Mn plot occur at relative distances of 0.25 and 0.75 along the total path length. These positions can be seen to correspond to positions on the faces of the initial and final Mn tetrahedra – positions at which the distance to neighboring O atoms reaches its minimum of 1.95 Å as compared to the distance at the endpoints of 2.07 Å. The Cr path shows a much flatter peak region between the path coordinates 0.38 and 0.62. These coordinates straddle the shared octahedral edge through which the migrating Cr atom must pass. Much like the case for Mn, in this region, the Cr-O bond length is reduced from its equilibrium value of 2.04 Å. If the Cr atom were to pass directly through the center of the octahedral edge, the bond length would be reduced to just 1.36 Å. However, our simulations predict a curved path which deviates from the [110] direction by bowing outwards towards the [001] direction. Along this curved path, the minimum Cr-O bond length is 1.79 Å. Using the magnitude of bond distortion as a proxy for migration energy yields a close fit for the trends observed in Mn and Cr migrations. In the most favorable charge states, the Mn migration barrier is only 19.8% that of Cr and similarly the amount of bond distortion 18.2% that of Cr. Both

profiles also differ significantly in the effect that defect charge state has on barrier height. For Mn, the barrier height of the 2^- charge state is 0.18 eV (29%) less than the neutral barrier. No such effect is observed for Cr, with its most favorable formation charge state (2^-) producing a nearly identical barrier height. When considering the migration of O, we must assess the viability of three previously discussed pathways. The NEB profiles of each path are shown in Figure 3-11.

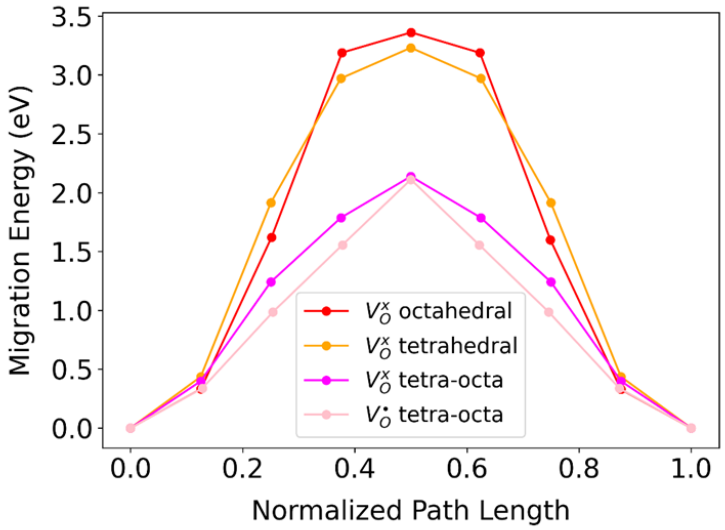

Figure 3-11. (Left) Migration energies for vacancy mediated O diffusion along the shared edge between two Cr octahedra (red), along the edge of a Mn tetrahedron (orange), and from the corner of a Mn tetrahedron to the corner of a Cr octahedron (pink).

The tetrahedral and octahedral edge pathways have nearly identical barrier heights, with a clear preference to migration between the corners of tetrahedra and octahedra. This pathway is favored by a margin of 1.1 eV. Inducing the most favorable charge state for O vacancy formation has a negligible effect on this barrier height.

In addition to simple direct vacancy migration, we identify four additional possibilities of vacancy mediated diffusion which incorporate substitution defects. From Table 3-5, the formation energies of both types of native substitutions are lower than

any vacancy defect. Therefore, in a system which contains vacancies we should also anticipate a larger number of substitutions. To fully understand the possible pathways by which cations may travel through the material, it is thus necessary to evaluate the barrier heights of migration mechanisms which incorporate both defect types. Presented in Table 3-6 are the equations which describe each mechanism.

Table 3-6. Pseudo Kröger-Vink notation of antisite/substitution defect migration mechanisms.

Migrating Species	Kröger-Vink Notation	Description
Mn	V_{Cr} (site 1) + Mn_{Cr} (site 1) → V_{Cr} (site 2) + Mn_{Cr} (site 2)	Vacancy mediated migration of an existing Mn_{Cr} substitution along the Cr sublattice.
Mn	V_{Cr} + Mn_{Mn} → V_{Mn} + Mn_{Cr}	Formation of a Mn_{Cr} substitution via Mn crossover to a vacant Cr lattice site.
Cr	V_{Mn} (site 1) + Cr_{Mn} (site 1) → V_{Mn} (site 2) + Cr_{Mn} (site 2)	Vacancy mediated migration of an existing Cr_{Mn} substitution along the Mn sublattice.
Cr	V_{Mn} + Cr_{Cr} → V_{Cr} + Cr_{Mn}	Formation of a Cr_{Mn} substitution via Cr crossover to a vacant Mn lattice site.

Figure 3-12 depicts the NEB profiles corresponding to rows 1 and 3 in Table 3-6. These two mechanisms follow the same pathways as their direct Cr and Mn counterparts, but the migrating atom is a substitution defect.

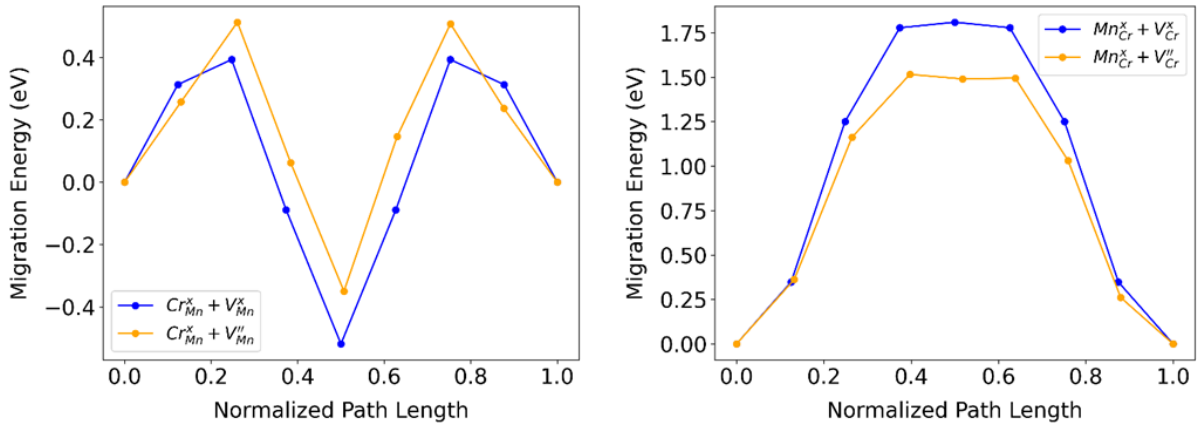

Figure 3-12. Barrier height for a vacancy mediated diffusion of a Cr_{Mn} substitution along the Mn sublattice (left), and a Mn_{Cr} substitution along the Cr sublattice (right).

On the left side of Figure 3-12 is the plot which represents a Cr atom occupying a Mn lattice site migrating along the Mn sublattice. Again, we observe the same double peak structure as was originally presented in the direct vacancy mechanism. However, this profile has a distinct minimum at the center of the path at which the energy is lower than either endpoint. This negative value suggests that when Cr_{Mn} substitution and Mn vacancy defects are in close proximity, the optimal arrangement is to split the vacancy over two Mn lattice sites and position the substituted Cr atom in the center of the structural vacancy between the faces of the two empty tetrahedra. This exact configuration is illustrated in Figure 3-13. From this position, the substituted Cr forms and the octahedron that is corner connected to neighboring Cr octahedra occupy their normal lattice positions. Furthermore, this mechanism serves as the highest mobility pathway for Cr migration with a barrier height of 0.85 eV, which is 1.56 eV lower than that of the direct vacancy mechanism. In the plot on the right of Figure 3-12, Mn sitting on a Cr lattice site migrates to the nearest vacant Cr site. This profile shares a similar shape to that seen in the direct Cr vacancy mechanism, but its 1.52 eV barrier height is lower than that of the direct mechanism by 0.89 eV. Since this mechanism involves migration of Mn, the reduction in barrier height relative to the direct Cr mechanism is inconsequential as it does not approach the 0.45 eV peak of the direct Mn vacancy mechanism. Therefore, this mechanism is unlikely to contribute to any significant amount of Mn diffusion.

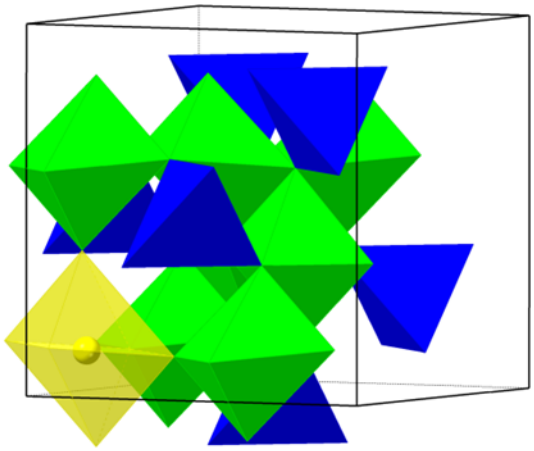

Figure 3-13. A Cr_{Mn} substitution defect in the midpoint of its migration between Mn sites coordinating to form an octahedron which is corner connected with other Cr octahedra.

The NEB profiles presented in Figure 3-14 represent the migration of a cation on its native sublattice crossing over to a vacancy on the adjacent sublattice to form a substitution defect and vacancy pair. The exact equations for these reactions can be found in rows 2 and 4 of Table 3-6. Unlike the previously presented NEB profiles, these are not expected to have equivalent endpoints as the initial and final states are two separate defect complexes.

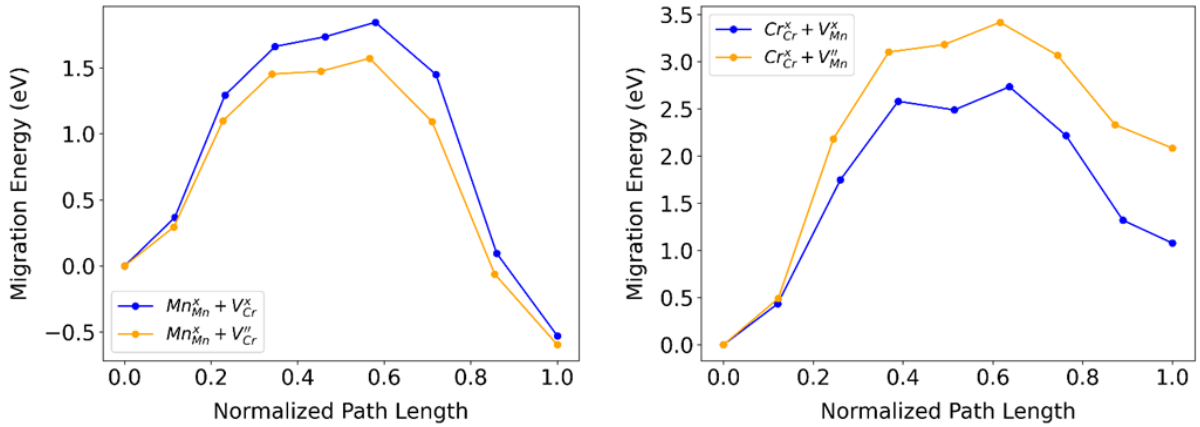

Figure 3-14. Barrier height for vacancy mediated diffusion of Mn crossing over to the Cr sublattice to form a Mn_{Cr} substitution (left) and Cr crossing over to the Mn sublattice to form a Cr_{Mn} substitution (right).

On the left side of Figure 3-14 is the formation of a Mn_{Cr} substitution and vacancy pair. This profile clearly shows the energetic favorability of the final state relative to the initial state (an isolated Cr vacancy). The opposite is true for the formation of a Cr_{Mn} substitution and vacancy pair. In this case, the formation energy of the initial Mn vacancy is less than that of the resulting vacancy + substitution complex. This result is consistent with the findings presented in Table 3-5 that the formation of Mn_{Cr} substitutions is thermodynamically more favorable than Cr_{Mn} substitutions. Considering that the formation energies presented in Table 3-5 are for isolated substitution defects, we can also conclude that the introduction of a vacancy near the substitution site (as is the situation in Figure 3-14) does not affect the ordering of the favorability for Cr_{Mn} and Mn_{Cr} defects. Comparing the barrier heights between the two substitution formation mechanisms it is evident that the formation of Mn_{Cr} is going to dominate kinetically with a barrier height of 1.57 eV relative to 2.73 eV for Cr_{Mn}.

3.3.6 Interstitial Mediated Migration

As shown previously in Chapter 3.3.3, cation and anion interstitials differ significantly in their formation energies. Because $O^{x}_{<110>}$ is more favorable than either cation interstitial at any charge state, only O interstitial migration is considered here. Two modes of interstitial mediated migration for oxygen are considered. In the simplest case, an oxygen atom in the split configuration jumps between two equivalent equilibrium positions on the same lattice site. To make this jump, the oxygen must cross a {101} plane. This mechanism has a very low barrier height at just 0.61 eV. However, because the atom never leaves its original lattice site, this does not contribute to the long-range migration of oxygen. Therefore, we explore an alternative three-body interstitialcy mechanism, illustrated in Figure 3-15. In this case, one oxygen in a split

interstitial configuration migrates off lattice to its nearest neighbor, allowing the other oxygen involved in the split to occupy the starting lattice site alone. The migrating atom pushes the neighboring oxygen off lattice along a <110> direction thus forming a new split-interstitial defect on a neighboring lattice site. The migration profile of this mechanism is shown on the right in Figure 3-15 and has a saddle point energy of 1.91 eV.

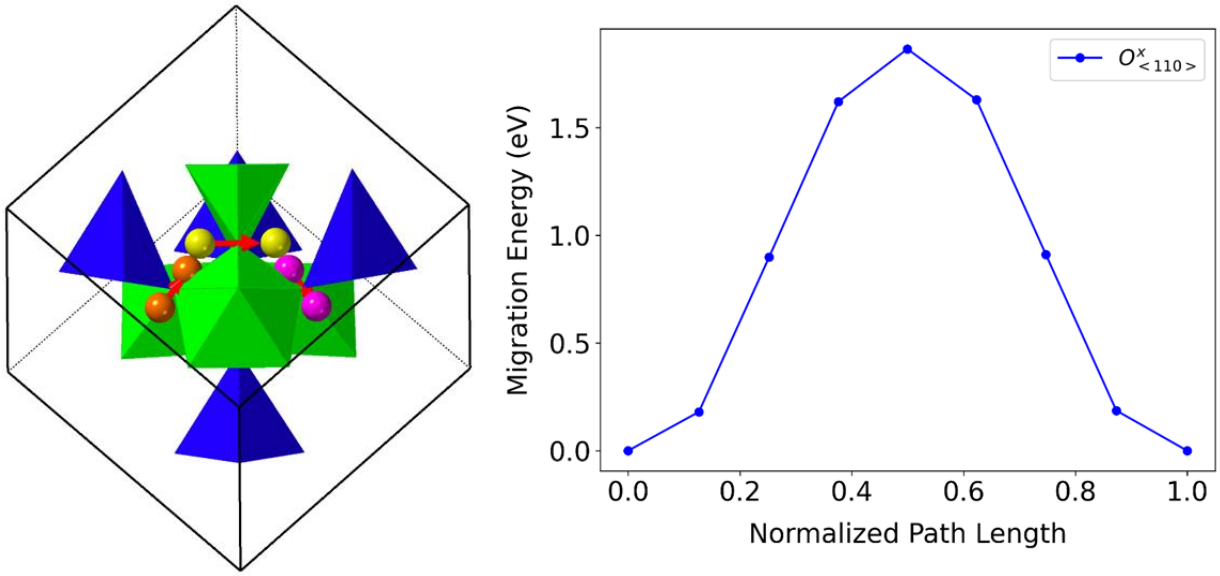

Figure 3-15. (Left) Diagram of the 3-body O interstitialcy mechanism. (Right) 3-body O interstitialcy mechanism NEB profile.

3.4 Discussion and Conclusions

In our analysis of isolated point defects in $MnCr_2O_4$ we find that there is a distinct preference to form cation vacancies over oxygen vacancies regardless of the environmental conditions. Despite this preference, we consider vacancy mediated migration mechanisms for all species. However, when considering interstitial defects, the preference to form O interstitials over cationic interstitials is so strong that we consider O to be the only species which is a viable candidate for interstitial mediated migration. Again, we find that this trend holds regardless of the temperature and

pressure conditions imposed on the system over the range we have investigated. Across four possible interstitial configurations for O, the lowest formation energy is associated with a dumbbell-type split interstitial which spans a direction in the <110> family. Due to the chemical complexity of spinels, it is also necessary to evaluate the favorability of antisite and substitution type defects. We find that inversion is not preferred for the $MnCr_2O_4$ composition due to the relatively high antisite formation energy. However, substitutions of Mn and Cr on their adjacent sublattices have formation energies less than that of vacancy defects indicating that they may play a role vacancy mediated diffusion. Therefore, in addition to evaluating the direct vacancy mediated diffusion pathways of each species, four additional pathways which incorporate substitution defects are also considered. We find that Mn is the most mobile cation with a peak barrier height of 0.45 eV in the 2^+ charge state. The direct vacancy mechanism to diffuse Cr is significantly higher in barrier height, but Cr can diffuse as a Cr_{Mn} substitution defect along the Mn sublattice with a barrier height that is approximately twice that of native Mn. Lastly, we find that O may diffuse via a vacancy mediated mechanism between the corners of Mn centered tetrahedra and Cr centered octahedra or via an interstitialcy mechanism with similar barrier heights.

The corrosion of $MnCr_2O_4$ is a complex process that involves surface reactions and component diffusion. The oxide growth could result from diffusion of the oxygen ions through the oxide to the metal interface or diffusion of metal ions to the oxide surface, or both. For the spinel oxide analyzed in this work, the lowest migration energy for Mn and Cr cations and O anions through $MnCr_2O_4$ are summarized in Table 3-7 Just

from comparing the migration energies, it appears that the Mn and Cr cations are more mobile than the O anions, and so will likely dominate the diffusion.

Table 3-7. Barrier heights of all diffusion mechanisms investigated in this work.

Migrating Species	Kröger-Vink Notation	Barrier Height (eV)
Mn	Mn^{x}_{Mn} (site 1) + V^{x}_{Mn} (site 1) → Mn^{x}_{Mn} (site 2) + V^{x}_{Mn} (site 2)	0.63
Mn	Mn^{x}_{Mn} (site 1) + V''_{Mn} (site 1) → Mn^{x}_{Mn} (site 2) + V''_{Mn} (site 2)	**0.45**
Mn	V^{x}_{Cr} (site 1) + Mn^{x}_{Cr} (site 1) → V^{x}_{Cr} (site 2) + Mn^{x}_{Cr} (site 2)	1.81
Mn	V''_{Cr} (site 1) + Mn^{x}_{Cr} (site 1) → V''_{Cr} (site 2) + Mn^{x}_{Cr} (site 2)	1.51
Mn	V^{x}_{Cr} + Mn^{x}_{Mn} → V^{x}_{Mn} + Mn^{x}_{Cr}	1.84
Mn	V''_{Cr} + Mn^{x}_{Mn} → V''_{Mn} + Mn^{x}_{Cr}	1.57
Cr	Cr^{x}_{Cr} (site 1) + V^{x}_{Cr} (site 1) → Cr^{x}_{Cr} (site 2) + V^{x}_{Cr} (site 2)	2.58
Cr	Cr^{x}_{Cr} (site 1) + V''_{Cr} (site 1) → Cr^{x}_{Cr} (site 2) + V''_{Cr} (site 2)	2.41
Cr	V^{x}_{Mn} (site 1) + Cr^{x}_{Mn} (site 1) → V^{x}_{Mn} (site 2) + Cr^{x}_{Mn} (site 2)	0.89
Cr	V''_{Mn} (site 1) + Cr^{x}_{Mn} (site 1) → V''_{Mn} (site 2) + Cr^{x}_{Mn} (site 2)	**0.85**
Cr	V^{x}_{Mn} + Cr^{x}_{Cr} → V^{x}_{Cr} + Cr^{x}_{Mn}	2.73
Cr	V''_{Mn} + Cr^{x}_{Cr} → V''_{Cr} + Cr^{x}_{Mn}	3.41
O	O^{x}_{O} (site 1) + V^{x}_{O} (site 1) → O^{x}_{O} (site 2) + V^{x}_{O} (site 2)	2.14
O	O^{x}_{O} (site 1) + V^{*}_{O} (site 1) → O^{x}_{O} (site 2) + V^{*}_{O} (site 2)	2.11
O	O^{x}_{i} (site 1) → O^{x}_{i} (site 2)	**1.86**

However, the migration energies only define a portion of the diffusivity. The prefactors are also needed and could be defined in the future using classical molecular dynamics (MD) or ab initio MD. Once prefactors are obtained, it will be possible to determine the dominant migrating species.

Corrosion models must define the growth of the oxide layer and the resultant weight gain. Accelerated diffusion along grain boundaries can significantly impact

oxidation rates, and so grain boundary diffusivities are often important. The migration energies obtained here are for diffusion within grains; future work is needed to investigate grain boundary diffusion. Mesoscale models of corrosion that resolve the microstructure will need these grain diffusivities, as well as grain boundary diffusivities. Macroscale corrosion models ignore the alloy and oxide microstructure and therefore only need an effective diffusion coefficient through the oxide layer. The effective diffusion is typically obtained as a function of the grain and grain boundary diffusivities, and the grain size. Corrosion models would need similar diffusivity values for each oxide type present.

Citing recent experimental data on the high-temperature corrosion of stainless steel alloys, it is evident that the $MnCr_2O_4$ phase dominates the bulk of the resultant oxide film in samples exposed to corrosive conditions although Mn_3O_4 and Cr_2O_3 phases are also formed. [7]. In order to understand the corrosion process of such alloys on an atomistic level, it is imperative that we identify the thermodynamically possible and kinetically probable diffusion mechanisms present within this oxide film. In this work, we have progressed that understanding by providing an in-depth analysis of point defect behavior in $MnCr_2O_4$ with considerations for the effect of corrosive environmental conditions. We find that Mn and Cr cations are the most mobile species when diffusing via vacancy and vacancy + substitution mechanisms respectively. The barrier height for O diffusion via interstitial or vacancy mediated mechanisms is significantly higher indicating that cation diffusion is likely to dominate. Even with a complete understanding of the relevant defects in the $MnCr_2O_4$ phase which contribute to corrosion, a unified corrosion model capable of predicting the evolution of the entire oxide film will be

incomplete without similar data for each constituent oxide phase. Therefore, in future work we aim to conduct a similar analysis of the Mn_3O_4 and Cr_2O_3 phases to provide the accurate diffusivity parameters required by such a model.

CHAPTER 4
ENERGETICS AND DIFFUSION KINETICS OF POINT DEFECTS IN Cr_2O_3 FROM FIRST PRINCIPLES

4.1 Background

Austenitic stainless steel alloys are ubiquitous in high-performance industrial applications due to their unique combination of robust mechanical properties and corrosion resistance at a reasonable cost [68], [70], [71]. The high Cr content in such alloy systems is known to form a passivating film which insulates the underlying structure from further oxidation [73]. However, this Cr-rich film can become a liability at long exposure times when the underlying alloy becomes so depleted of Cr that a brittle ferrite phase forms at the interface making the material susceptible to fracture [111], [112]. Fortunately, additional alloying elements can mitigate this effect by changing the energetics, kinetics, and composition of the resulting oxide film [113].

To develop a mechanistic understanding of this oxidation process, it is necessary to characterize the defect behavior in each oxide component. In the widely used 21-2N alloy, the oxide phases which are observed to develop in a high-temperature dry atmosphere include $MnCr_2O_4$, Cr_2O_3, and Mn_3O_4 [7]. We have previously investigated the $MnCr_2O_4$ spinel phase in this context [114]. Cr_2O_3 is next of interest due to its mediating position between the spinel and outermost Mn_3O_4 layer. Prior DFT work has been conducted to characterize the formation and migration of native Cr and O defects [100], [115], though there is a knowledge gap relating to the behavior of foreign cations which is of paramount importance in understanding how the multilayer oxide film evolves over the course of its development under corrosive conditions.

Therefore, in this work we evaluate the thermodynamic favorability of forming both native Cr and foreign Mn defects. Defects with low formation energy are assessed

for their mobility along a set of elementary migration pathways compatible with long-range diffusion. The effects of defect charge state and environmental conditions are considered to model the process with the physical context in which it occurs. Lastly, the results of this work and prior studies are compiled to inform a mechanistic understanding of the experimentally observed oxide evolution at long exposure times.

4.2 Computational Methodology

The density functional theory (DFT) calculations in this work are performed with the Vienna Ab initio Simulation Package (VASP) [83], [84], [85]. Projector augmented plane wave (PAW) pseudopotentials [86] are used to describe the interactions between core and valence electrons. The generalized gradient approximation (GGA) and Perdex-Burke-Ernzerhof (PBE) functional [23] are used to describe exchange correlation energies. Due to limitations of DFT in regards to accurately modeling localized d electrons [35], GGA+U is employed and the value of U is set to 3.5 eV for Cr [74]. A plane-wave cutoff energy of 500 eV is chosen following a convergence study over the range of 300 – 600 eV. The simulation cell for defect formation and migration calculations is a 2 x 2 x 1 supercell of the trigonal $R\bar{3}c$ corundum-like Cr_2O_3 unit cell. The defect-free system contains 120 atoms total and the relaxed lattice parameters are as follows: $a = b = 10.09$ Å, $c = 13.93$ Å, $\alpha = \beta = 90^o$, $\gamma = 120^o$. A k-point convergence study found that a Γ-point centered 3 x 3 x 2 Monkhorst-Pack mesh [88] provides a reasonable balance between computation speed and precision. Spin polarization is enabled for all calculations and magnetic moments on the Cr sublattice are initialized to ± 5.0 μ_B to create an antiferromagnetic (AFM) ordering. The sign of the magnetic moment alternates based on each atom's position along the *c*-axis of the simulation cell

to create a layered-AFM configuration. Structure relaxations employ a Gaussian smearing scheme with a smearing width of 0.05 eV as is recommended for insulating materials in the VASP documentation. Total energy values are extracted from single-point calculations of the optimized structure with the smearing scheme switched to the tetrahedron method with Blöchl corrections [89].

Defect formation energy calculations in this work consider the effect of defect charge state by employing the *sxdefectalign* package [90] to compute Freysoldt/Neugebauer/Van de Walle (FNV) correction energy [91], [92]. This correction term is required to counteract the effect of self-interaction for charged defects in a periodic simulation cell. The defect formation energy is calculated via Equation 1:

$$E_F^q = E_{def}^q - E_{ref} - \sum_i n_i \mu_i + qE_{Fermi} + E_{corr} \quad (4\text{-}1)$$

Where E_{def}^q is the total energy of the simulation cell containing the charged defect, E_{ref} is the total energy of the charge neutral defect-free simulation cell, n_i is the number of atoms of species i which contribute to the defect, μ_i is the chemical potential of each species i, q is the defect charge state, E_{Fermi} is the Fermi energy with respect to the vacuum level, and E_{corr} is the FNV correction energy.

This work also considers the effect of environmental conditions on defect formation energy. The oxidizing environment in which this corrosion process takes place can be approximated in an ab-initio framework by adjusting the chemical potentials of the defect species to simulate thermodynamic conditions of 1000 K and an O_2 partial pressure of 0.2 atm. Adjustments to the chemical potential are determined using the methodology of Finnis et al. [93] which has been widely used to conduct ab-initio thermodynamics studies [94], [95], [96], [97], [98], [99], [100]. For greater detail on the

implementation of this method we direct the reader to our prior work which utilizes the same technique [114].

Migration energy barriers are determined using the climbing image nudged elastic band method (CI-NEB) as implemented in the VASP transition state tools (VTST) developed by the Henkelman group [102], [103]. Each CI-NEB calculation is interpolated over 7 intermediate images to achieve high resolution diffusion profiles. A spring constant of 5.0 eV/Å^2 assigned to each of the virtual springs connecting the intermediate images proved to be adequately flexible to achieve full relaxation along each migration pathway.

4.3 Results

4.3.1 Point Defect Formation

Isolated vacancy, interstitial, and substitution type defects in the Cr_2O_3 lattice are assessed at varying charge states up to and including their expected formal charge to identify key defect transition levels within the bandgap. The valence band maximum (VBM) and conduction band minimum (CBM) values required to define the span of the bandgap are calculated using the same GGA+U functional used throughout this work. The predicted band edges are 3.32 eV and 6.77 eV for a bandgap of 3.45 eV.

The formation energy of an isolated Cr vacancy is plotted in Figure 4-1. It can be seen that the expected formal charge state (V_{Cr}''') is indeed predicted to have the lowest formation energy at the CBM. Interestingly, the formation energy is negative which suggests that some concentration of vacancy defects should be expected very near to the conduction band edge. Furthermore, three distinct transition levels are observed at 1 eV, 1.6 eV, and 2.2 eV into the bandgap. The exact values for each charge state are reported in Table 4-1.

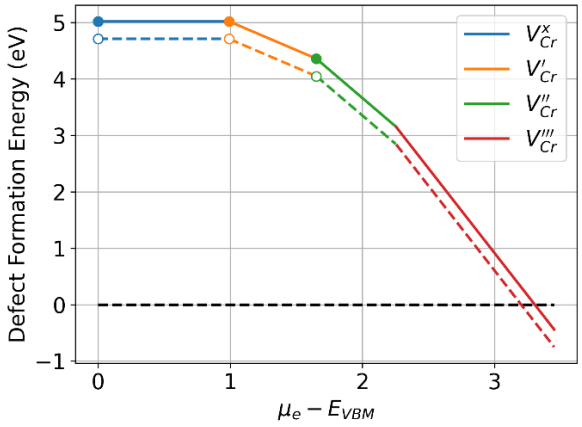

Figure 4-1. Cr vacancy defect formation energy at different charge states as a function of position in the bandgap. Solid lines represent the 0 K condition and dashed lines represent the 1000 K condition.

Table 4-1. Tabulated Cr vacancy formation energy of each charge state at the VBM and CBM. The lowest formation energy is in bold.

Defect	Formation Energy at VBM (eV) 0K/1000K	Formation Energy at CBM (eV) 0K/1000K
V_{Cr}^{x}	5.02/4.17	5.02/4.71
$V_{Cr}^{\prime}$	6.01/5.7	2.56/2.25
$V_{Cr}^{\prime\prime}$	7.66/7.35	0.76/0.45
$V_{Cr}^{\prime\prime\prime}$	9.92/9.61	**-0.44/-0.75**

Interstitial defects of both Cr and Mn are compared to identify possible preferences for non-native cation intercalation. Only one interstitial configuration, Wyckoff site 6b, is considered because our tests show that it is energetically equivalent to the alternative 36f site. Figure 4-2 compares the defect transition levels of Cr_{6b} (Figure 4-2a) and Mn_{6b} (Figure 4-2b) interstitials. The Cr interstitial is higher in energy than the comparable vacancy defect throughout the width of the band gap indicating a higher likelihood of vacancy formation and a low population of native interstitial defects. In contrast, Mn interstitial formation is more favorable than Cr by a margin of 0.22 eV at the lowest point. Additionally, Mn does not exhibit a transition to the expected formal charge ($Mn_{6b}^{\bullet\bullet\bullet}$), and instead favors the $Mn_{6b}^{\bullet\bullet}$ state from the VBM up until a transition to

$Mn_{6b}^{\bullet}$ at 2.3 eV into the bandgap. The exact formation energy for each species at each charge state is reported in Table 4-2.

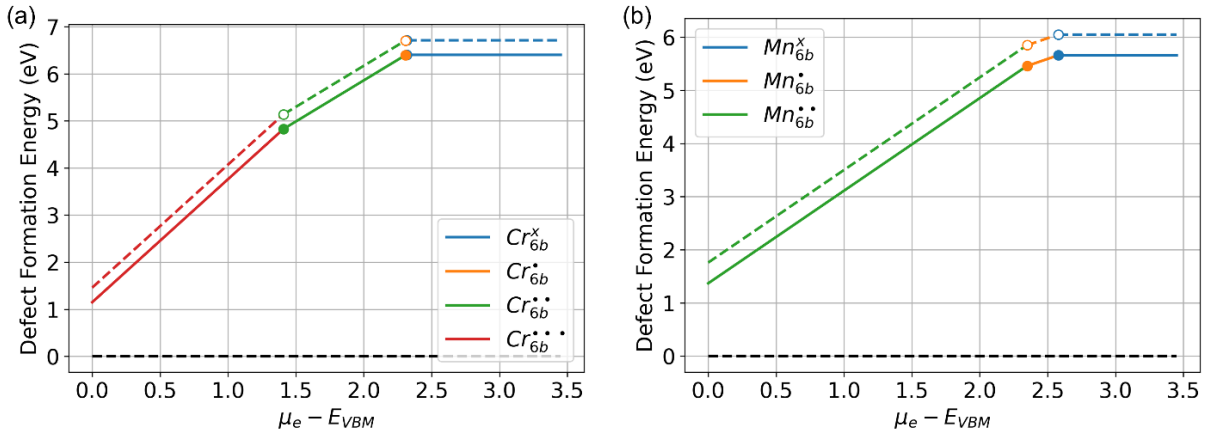

Figure 4-2. Interstitial formation energy at different charge states as a function of position in the band gap. Each subplot represents a different species: Cr (a), Mn (b). Solid lines represent the 0 K condition and dashed lines represent the 1000 K condition.

Table 4-2. Tabulated interstitial formation energy values of each charge state at the VBM and CBM. The lowest formation energy for each species is in bold.

Defect	Formation Energy at VBM (eV) 0K/1000K	Formation Energy at CBM (eV) 0K/1000K
Cr_{6b}^{x}	6.40/6.71	6.40/6.71
$Cr_{6b}^{\bullet}$	4.38/4.69	7.39/7.70
$Cr_{6b}^{\bullet\bullet}$	2.37/2.68	8.39/8.70
$Cr_{6b}^{\bullet\bullet\bullet}$	**1.15/1.46**	10.16/10.47
Mn_{6b}^{x}	5.66/6.05	5.66/6.05
$Mn_{6b}^{\bullet}$	3.41/3.80	6.42/6.81
$Mn_{6b}^{\bullet\bullet}$	**1.37/1.76**	7.38/7.77
$Mn_{6b}^{\bullet\bullet\bullet}$	2.31/2.70	11.33/11.72

Due to the interest in mapping out likely diffusion mechanisms across different oxides, the substitution of Mn for Cr is a crucial defect type to understand in the context of a Mn/Cr oxide interface. In Figure 4-3, the Mn_{Cr} substitution defect is plotted for charge states ranging from -1 to +1. From inspection, the Mn_{Cr}' state dominates most of

the bandgap and has a highly favorable formation energy at the CBM. The fact that this defect is predicted to form spontaneously suggests that existing Cr vacancies can be readily occupied by incoming Mn cations. Additionally, the strong preference to form the Mn'_{Cr} state is consistent with the results presented in Figure 4-2 which indicate a difference in preferred charge state between Cr and Mn interstitials. By replacing a Cr^{3+} with a Mn^{2+}, as is the situation in a Mn_{Cr} substitution, it follows that the charge on the defect site should be -1 which is indeed the result reported here. For exact values of each charge state at the VBM and CBM, refer to Table 4-3.

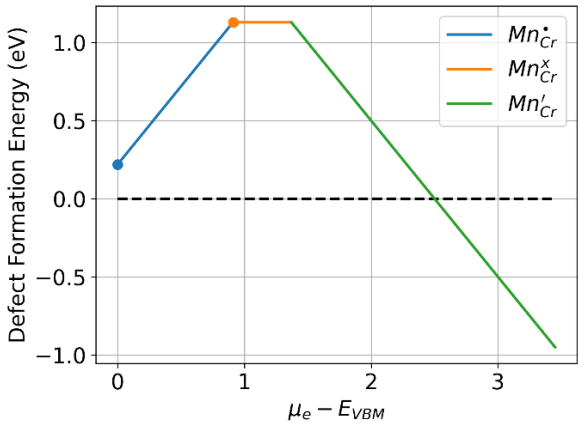

Figure 4-3. MnCr substitution formation energy at different charge states as a function of position in the bandgap. Only the 0 K condition is shown because the effect of temperature is negligible for substitution defects.

Table 4-3. Tabulated MnCr substitution formation energy values of each charge state at the VBM and CBM. The lowest formation energy is in bold.

Defect	Formation Energy at VBM (eV)	Formation Energy at CBM (eV)
$Mn^{\bullet}_{Cr}$	0.22	3.67
Mn^{x}_{Cr}	1.13	1.13
Mn'_{Cr}	2.50	**-0.95**

4.3.2 Point Defect Migration

Having established a basis for understanding the relative thermodynamic favorability between the defect types under consideration, we proceed to evaluate the kinetic barriers associated with those that are predicted to be most prevalent. Specifically, migration reactions consisting of both vacancy and substitution type defects are analyzed due to their low formation energies. Interstitial type defects are excluded from this analysis because the corresponding vacancy type defect is dominant throughout the bandgap.

Four unique migration pathways, first introduced by Gray et al. [100], are considered for each defect type. To remain consistent with their original naming convention we adopt the names V_1-V_2, V_1-V_3, V_2-V_4, and V_3-V_4 to indicate that each path is vacancy mediated but can be traversed by either Cr or Mn. Path V_1-V_2 (Figure 4-4a) is limited to in-plane migration within the purely cationic (001) plane. Path V_1-V_3 (Figure 4-4b) is aligned with the [001] direction and crosses through a single plane of O atoms. Path V_2-V_4 (Figure 4-4c) is also aligned with the [001] direction but passes through two planes of O atoms. Lastly, path V_3-V_4 (Figure 4-4d) is not axially aligned, but bridges across one layer of O atoms. Taken together, these elementary paths can be chained together indefinitely to enable long-range diffusion.

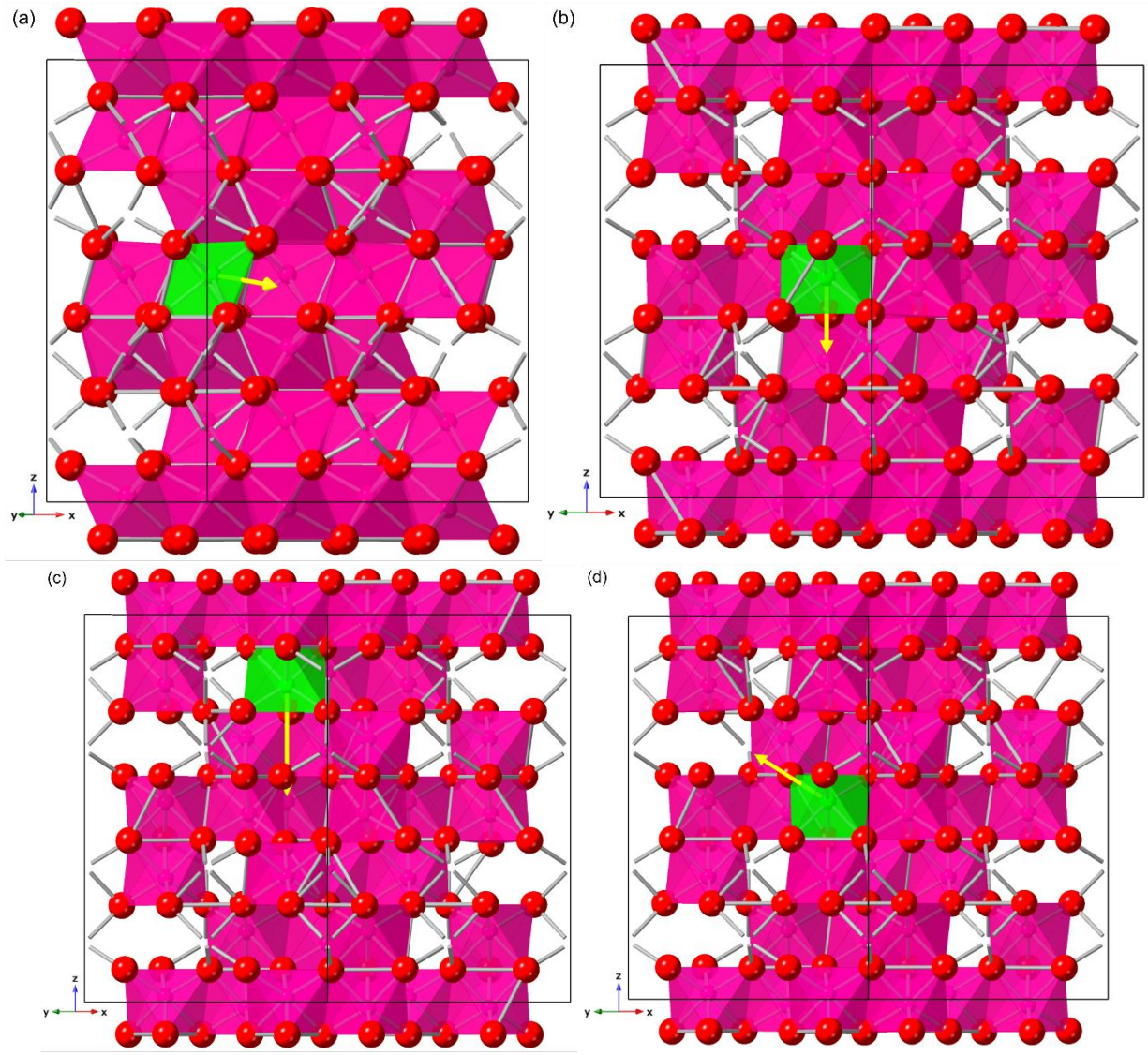

Figure 4-4. Schematics of different vacancy mediated diffusion pathways. The yellow vector represents the direction of travel. Each subplot corresponds to a different pathway: V_1-V_2 (a), V_1-V_3 (b), V_2-V_4 (c), and V_3-V_4 (d).

The migration profiles associated with each of the elementary paths are shown in Figure 4-5. In all instances, the migration of Mn as a Mn_{Cr} substitution defect has a significantly lower barrier height than the corresponding native Cr migration. Additionally, treating the mediating Cr vacancy as its most stable charge state (V_{Cr}''') consistently results in a reduced barrier height for both Cr and Mn migration. Path V_1-V_2 produces the lowest barrier height for all defect types and charge states indicating that

diffusion through purely cationic layers is more rapid than crossing anionic O layers. However, to achieve long-range diffusion, V_1-V_2 must be chained with a path that crosses O layers. The only O bridging path directly compatible with V_1-V_2 is V_2-V_4 which has a barrier height of 1.46 eV for Mn diffusion and 2.73 eV for Cr diffusion. Alternatively, the V_1-V_3 + V_3-V_4 pair is also viable for long-range diffusion. The rate limiting step for this combination is the V_3-V_4 jump for Mn (1.58 eV) and the V_1-V_3 jump for Cr (2.37 eV). Therefore, the most efficient path to long-range diffusion for Mn is via the V_1-V_2 + V_2-V_4 pair which is rate limited by the V_2-V_4 O-bridging jump at 1.46 eV while the diffusion of Cr proceeds along the V_1-V_3 + V_3-V_4 pair which is rate limited by the V_1-V_3 O-bridging jump at 2.37 eV. The barrier height associated with the most efficient combinations of elementary jumps to achieve long-range diffusion are enumerated in Table 4-4 for each species.

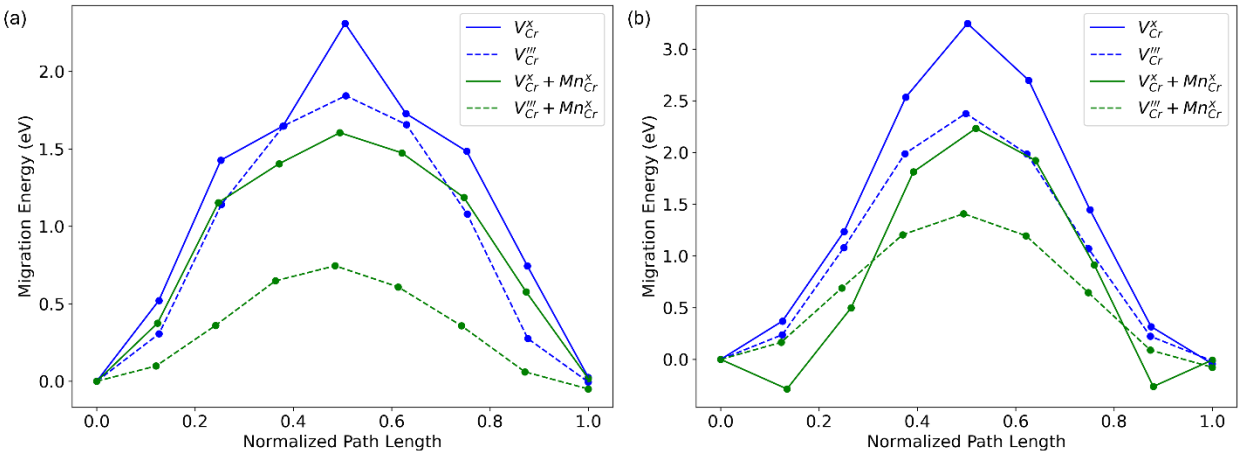

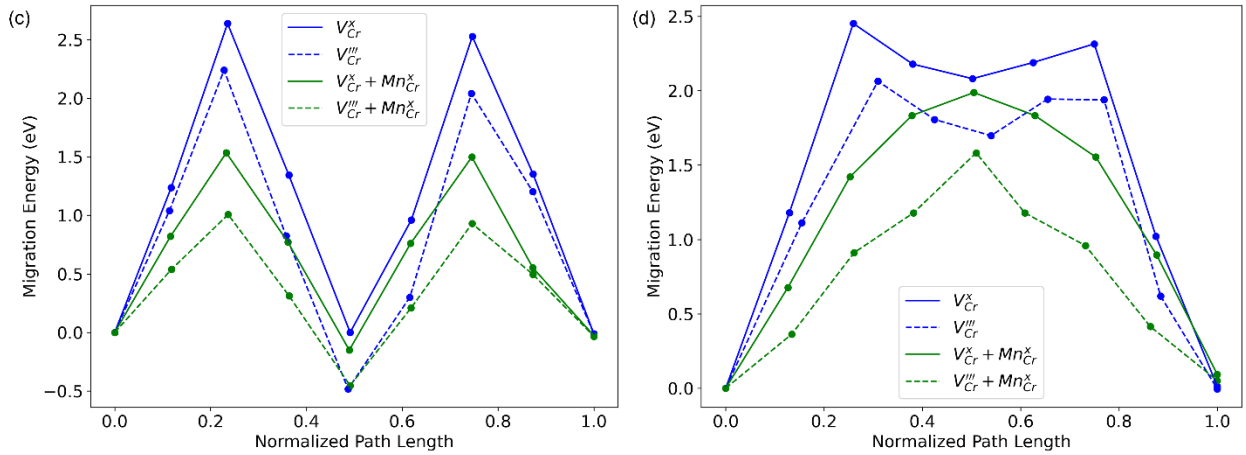

Figure 4-5. Vacancy mediated migration profiles for Cr and Mn at different charge states. Each subplot corresponds to a different migration pathway: V_1-V_2 (a), V_1-V_3 (b), V_2-V_4 (c), and V_3-V_4 (d). Profiles which diffuse Cr are blue, and profiles which diffuse Mn are green. Solid lines represent the V_{Cr}^{x} charge state and dashed lines represent the $V_{Cr}^{'''}$ charge state.

Table 4-4. Tabulated barrier heights of the most efficient elementary jump combinations to achieve long-range diffusion for each species. Rate limiting barrier heights are in bold.

Migrating Species	Mediating Defect	Path	Barrier Height (eV)
Cr	$V_{Cr}^{'''}$	V_1-V_3	**2.37**
Cr	$V_{Cr}^{'''}$	V_3-V_4	2.06
Mn	$V_{Cr}^{'''} + Mn_{Cr}^{x}$	V_1-V_2	0.75
Mn	$V_{Cr}^{'''} + Mn_{Cr}^{x}$	V_2-V_4	**1.46**

4.4 Discussion and Conclusions

In this work, the formation and migration of point defects relevant to oxide evolution in Cr_2O_3 are assessed to inform a mechanistic model of the growth process in a multilayer oxide film. Vacancy type defects are found to be more favorable than interstitials regardless of charge state or environmental conditions. Additionally, the incorporation of Mn cations into the Cr_2O_3 lattice as Mn_{Cr} substitutions is found to have a low energy barrier, even becoming spontaneous at the CBM indicating facile uptake of Mn into Cr vacancy sites. Four elementary vacancy mediated migration pathways are

evaluated using NEB calculations to identify the most efficient combinations capable of long-range diffusion for both Mn and Cr. Diffusion of Mn through the Cr_2O_3 lattice as a Mn_{Cr} substitution is consistently found to have a lower barrier height than native Cr. The effect of defect charge state on migration barrier height is also investigated resulting in the finding that treatment of the mediating Cr vacancy defect as its most stable charge state (V_{Cr}''') significantly reduces barrier height for both Cr and Mn migration.

Combining these findings with our prior work on the $MnCr_2O_4$ spinel [114], which is also found to be a component of the multilayer oxide film that forms atop 21-2N steel alloy, enables deeper insights into the mechanisms controlling the oxide evolution process. Specifically, it is instructive to consider the results presented by Abdallah et al. [7] between the period of 900 and 1925 hours of exposure time during which the total thickness of the film remains constant, but the relative thickness of layers within the film continues to change. To illustrate this process, Figure 4-6 presents a schematic of the oxide evolution during that period along with annotations indicating potential atomistic mechanisms. The proposed mechanisms are evaluated in the context of the kinetics presented in this work to identify those which are most likely and the specific interfaces at which growth occurs for each component of the film.

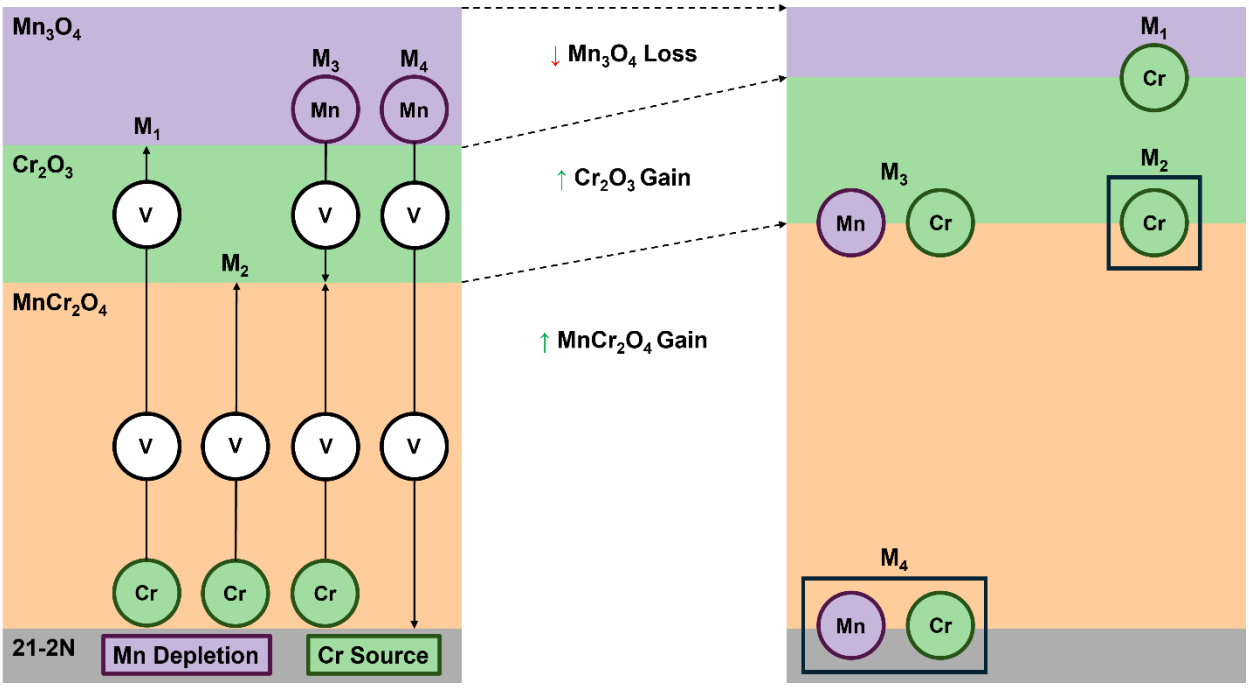

Figure 4-6. Schematic of four possible mechanisms that explain the oxide film evolution between 900 and 1925 hours of exposure time under the conditions described by Abdallah et al. [7]. The most likely mechanisms are denoted with a black bounding box.

The most notable change observed in Figure 4-6 corresponds to the increasing thickness of $MnCr_2O_4$ spinel and Cr_2O_3 at the expense of Mn_3O_4 resulting in a net zero change in total oxide thickness. Some additional context important in understanding the logic behind each mechanism is the fact that the underlying 21-2N alloy forms a Mn depletion zone just beneath the $MnCr_2O_4$ layer as the oxide forms due to the low concentration of Mn (8.5 wt%) relative to Cr (20.25 wt%) [7] and Mn's rapid diffusivity through the alloy [116]. This creates the boundary conditions that Mn_3O_4 is the primary source of Mn while the alloy is still capable of providing Cr. Under these conditions, we propose four possible mechanisms for consideration: Cr from the alloy migrates via vacancy mediated diffusion through $MnCr_2O_4$ and Cr_2O_3 meeting with O at the Cr_2O_3/Mn_3O_4 interface to produce more Cr_2O_3 (M_1), Cr from the alloy migrates via vacancy mediated diffusion through $MnCr_2O_4$ meeting with O at the $MnCr_2O_4/Cr_2O_3$

interface to produce more Cr_2O_3 (M_2), Cr from the alloy migrates via vacancy mediated diffusion through $MnCr_2O_4$ and Mn from Mn_3O_4 migrates through Cr_2O_3 via vacancy mediated diffusion to meet with O at the $MnCr_2O_4$ /Cr_2O_3 interface and produce more $MnCr_2O_4$ (M_3), lastly, Mn from Mn_3O_4 migrates through Cr_2O_3 and $MnCr_2O_4$ via vacancy mediated diffusion to meet with Cr and O at the alloy/$MnCr_2O_4$ interface and produce more $MnCr_2O_4$ (M_4).

Mechanisms M_1 and M_2 relate to the growth of Cr_2O_3. For M_1 to be most likely, Cr diffusion through Cr_2O_3 must be faster than O diffusion through both Mn_3O_4 and Cr_2O_3. In this work, we have identified that the lowest possible barrier height for long-range Cr diffusion through Cr_2O_3 is 2.37 eV and our prior work predicts Cr to have a minimum barrier height of 0.85 eV through $MnCr_2O_4$ [114]. A DFT study of O migration in Cr_2O_3 reveals that O is highly mobile as O_i'' with a barrier height ranging from 0.29 to 0.58 eV depending on the direction of travel [115]. Unfortunately, there is insufficient literature on O migration barriers through Mn_3O_4 to draw a direct comparison. Therefore, we make an approximation that O migration through Mn_3O_4 likely has a lower bound of 0.29 eV as predicted in Cr_2O_3 [115] and an upper bound of 1.86 eV as predicted in $MnCr_2O_4$ [114]. Even at the upper end of this range, O through Mn_3O_4 outpaces Cr in Cr_2O_3. However, due to the high diffusivity of Cr through $MnCr_2O_4$, it is important to consider the total diffusion distance required for each species to meet at the interface. Because the outermost Mn_3O_4 layer is so thin relative to $MnCr_2O_4$, 0.5 μm vs. 1.2 μm at the 900 hours mark [7], it is reasonable to predict that O would reach the Cr_2O_3 layer before Cr does. Furthermore, as the evolution proceeds, the loss of Mn_3O_4 and growth of $MnCr_2O_4$ produces even more favorable conditions for O to arrive first. Upon reaching

Cr_2O_3, the diffusivity of O dominates leading to both species meeting at the $Cr_2O_3/MnCr_2O_4$ interface thus satisfying M_2. However, this conclusion is at odds with the findings of a phase-field study of the same oxide film which predicts Cr_2O_3 growth at the outer interface with Mn_3O_4 [117], [118]. This discrepancy could be due to error in our approximation of O diffusivity through Mn_3O_4 or perhaps evidence of a transition between dominant growth mechanisms that is dependent on the relative thicknesses of Mn_3O_4 and $MnCr_2O_4$ over the course of oxide growth. This finding highlights the need for an in-depth analysis of point defect migration in Mn_3O_4 as well as the possibility of identifying different growth mechanisms dependent on the stage of the growth process.

Mechanisms M_3 and M_4 relate to the growth of $MnCr_2O_4$. For M_3 to be most likely, the diffusion of Cr through $MnCr_2O_4$ must be faster than the diffusion of Mn through both Cr_2O_3 and $MnCr_2O4$. In this work, we have found that Mn diffuses through Cr_2O_3 as a Mn_{Cr} substitution defect even more readily than native Cr with a minimum barrier height for long-range diffusion of 1.46 eV. Our prior work predicts a barrier height of just 0.45 eV for Mn diffusion through $MnCr_2O_4$ [114]. As stated previously, the barrier height for Cr diffusion through $MnCr_2O_4$ is 0.85 eV. Although Cr migrates through $MnCr_2O_4$ more rapidly than Mn through Cr_2O_3, the thickness of Cr_2O_3 at 900 hours is just 0.08 μm. Therefore, diffusion through the 1.2 μm $MnCr_2O_4$ layer controls the mechanism. The barrier height of Mn for this process is approximately half that of Cr which results in Mn being able to rapidly reach the alloy/$MnCr_2O_4$ interface and satisfying M_4. In this instance, our predictions agree with the phase-field model [117], [118]. The fact that the two methods agree when the mechanism does not need to incorporate an estimated value for O diffusivity further highlights the value of a future study on migration barriers

in Mn_3O_4. Furthermore, to extend our prior comment on the influence of relative layer thickness on preferred mechanism, it is interesting to observe that if Cr_2O_3 continues to grow at a rate greater than or equal to $MnCr_2O_4$ then inward Mn diffusion will be hindered relative to outward Cr diffusion thus opening the possibility of a mechanism reversal.

In conclusion, this work has investigated the defect energetics and kinetics of point defects involved in the growth of Cr_2O_3 and $MnCr_2O_4$ as components of a multilayered oxide film which is observed to form atop 21-2N stainless steel when exposed to corrosive conditions. The diffusivity of Mn as a Mn_{Cr} substitution defect is found to be more mobile than native Cr via a vacancy mediated diffusion mechanism. These results are incorporated with other works on the same multilayered oxide film to predict the atomistic mechanisms driving the change in relative layer thickness observed after the total thickness of the oxide film has stabilized. $MnCr_2O_4$ is predicted to grow at the interface with the bulk alloy and Cr_2O_3 is predicted to grow at the interface with $MnCr_2O_4$. However, a reversal in either mechanism is recognized as a possibility as the relative thickness of each layer changes during the corrosion process. Future work to identify the modality and barrier height of O diffusion through Mn_3O_4 could be incorporated to make the mechanistic predictions more comprehensive.

CHAPTER 5
PREFERENTIAL INTERLAYER ADSORPTION SITES IN PHYLLOSILICATE CLAY EDGE MODELS BY MOLECULAR DYNAMICS SIMULATION[*]

5.1 Background

Nuclear energy production is an attractive way to satiate the growing energy demands of our society due to its low carbon footprint relative to fossil fuels [8], [9], [119]. However, the radioactive high-level waste (HLW) and used nuclear fuel (UNF) generated as byproducts in nuclear reactor facilities poses a challenge to the health and safety of surrounding communities and the environment at large. One solution for safe disposal of these dangerous byproducts proposed by multiple national agencies is to use deep geological repositories [10], [11], [120], [121], [122]. These repositories are the final stage of the nuclear fuel cycle and as such must remain stable and performant on the timescale of one million years [12]. Clay minerals are stable over these geological timescales and offer additional beneficial properties that make them excellent candidates as buffer materials for these proposed repositories, including high sorption and ion exchange capacity, swelling to limit permeability in water, and high availability in the Earth's crust [123], [124], [125], [126]. In addition to protecting the waste package from its surroundings, the buffer material must be capable of sequestering radionuclides in the event of a container breach [10], [127]. Fission products such as iodine-129 and technetium-99 are critical targets for sequestration due to their high mobility in water and tendency to form a variety of polyatomic ions [128], [129], [130].

[*] The work described in this chapter is under review for publication R. Seaton Ullberg, An T. Ta, and Simon R. Phillpot. "Preferential Interlayer Adsorption Sites in Phyllosilicate Clay Edge Models by Molecular Dynamics Simulation." *Applied Clay Science* (Under Review).

Atomic resolution calculations and simulations have proven to be a valuable tool in developing an understanding of engineered buffer materials for HLW and UNF disposal [131], [132], [133]. In particular, molecular dynamics (MD) simulations are capable of probing the dynamical behavior of these materials at the nanoscale. Prior works have used MD simulation in the context of evaluating possible clay buffer materials to predict anion exclusion from hydrated interlayers [134], the diffusivity of solvated ions [135], [136], [137], and the structure of edge terminations [138].

To address the phenomenon of anion exclusion, which is particularly impactful when considering the sequestration of anionic radionuclides such as iodate (IO_3^-) and pertechnetate (TcO_4^-), Tournassat et al. [134] simulated a (110) terminated montmorillonite nanoparticle adjacent to a region of dilute NaCl solution, referred to as the mesopore. $Mg_{Al}^{'}$ substitutions in their system were randomly distributed throughout three montmorillonite sheets to produce a mean layer charge density of -0.1 Cm^{-2}, approximately -0.29 electrons per unit cell (e/u.c.), with the stipulation that substitutions could not be located near edge surfaces. The authors used three simulation cells which differ in interlayer water content (and by extension interlayer spacing) to assess the accessibility of the interlayer. The two water-layer system, which was the lowest degree of hydration tested, was found to completely exclude Cl^- ions from the interlayer while both three- and five-layer systems were found to accommodate the anion. In all three systems, Na^+ ions were found to occupy the interlayer at a higher concentration than the mesopore.

Kosakowski et al. [135] advanced our understanding of interlayer dynamics by determining water and ion diffusivities in mixed Na-Cs-montmorillonite from Monte Carlo

and MD simulations. They found that in interlayers with low hydration (monolayer water coverage) Cs^+ ions are immobilized and tend to adsorb to the hexagonal cavities present in the tetrahedral layer of the montmorillonite clay sheet. The diffusivities of water and Na^+ ions were found to be similar to each other at all levels of hydration, approaching their bulk values beyond tetralayer water coverage. The clay model used in that study included no edge terminations and had an ordered arrangement of charged substitution sites which limits its applicability to only highly idealized interlayer structures.

Greathouse et al. [136] expanded upon the work of Kosakowski et al. [135] by analyzing the effects of layer charge, cation species, water content, and temperature in a similar montmorillonite interlayer system. They reported that a layer charge on the lower end of experimentally reported results, -0.375 e/u.c. produces a more hydrophobic interlayer condition which leads to increased diffusivity of both water and ions relative to a highly charged (-0.75 e/u.c.) clay sheet. Interlayer hydration was only found to have a significant impact on diffusivity in the monolayer water coverage condition. At 2- and 3-layer water coverage, ions are fully hydrated and move more freely through the interlayer. The diffusivity of ions in the interlayer was found to be almost the same as that in bulk electrolyte solutions of the same concentration. Furthermore, diffusion behavior in the interlayer fluid maintained the trend observed in bulk solution that higher concentrations of electrolyte produce lower diffusion coefficients. However, this study was conducted using an infinite interlayer representation which is a limited analog to real clay nanoparticle systems, which contain edge terminations.

While Kosakowski et al. [135] and Greathouse et al. [136] have conducted extensive work characterizing the effects of interlayer composition and environmental conditions on ion diffusivity, one structural variable left unevaluated by the authors is the effect of substitutional disorder in the montmorillonite clay sheet. Ngouana W. and Kalinichev [137] addressed this limitation by introducing three unique models for montmorillonite. Their most uniform model, referred to as Uni, contains only octahedral substitutions arranged on a uniform rectangular grid. Two disordered models, RanO and RanTO, contain a random distribution of substitutions limited to the octahedral layer or mixed between the octahedral and tetrahedral layers respectively. Restrictions were applied to the RanO and RanTO models to ensure that there is at least one Al site between every substitution site. They reported that the interlayer spacing is similar across all three models and that the same four distinct binding sites for ions on the tetrahedral layer of the clay sheet are active in each model. These findings suggested that substitutional disorder has a negligible impact on the behavior of interlayer ions, However, they did not consider the effect of edge surfaces which, when paired with varying degrees of substitutional disorder, may impact interlayer composition and ionic diffusivity.

In contrast to the previously introduced works which focus their efforts on characterizing behaviors of the interlayer region, Newton et al. [138] used a combination of ab-initio and classical MD simulations to develop an atomistic model of the montmorillonite edge surface. They found that excess negative charge at edge terminations due to solvent accessible octahedral substitutions tends to produce more disordered edge structures than models with bulk octahedral substitutions. While the

work is thorough in its analysis of clay edge surface structures, it did not consider charge-compensating ions which are likely to behave differently in the near-edge and bulk substituted models.

Through our review of this relevant literature, we have identified a significant knowledge gap relating specifically to the behavior of ions in the presence of edge-terminated montmorillonite sheets as a function of the arrangement of their octahedral substitution sites. To close this gap, we have conducted a series of MD simulations on clay edge models with substitutions placed specifically to create unique, representative, chemical environments at the edge surfaces and in the deep interlayer region. We use the resulting simulated trajectories from each model to assess how the presence of excess negative charge in different locations relative to the edge termination influences the favorable adsorption sites, interlayer composition, and dynamical behavior of ions.

5.2 Simulation Cell and Computational Methodology

5.2.1 Clay Edge Structures

In this work we consider two structurally similar dioctahedral clays: pyrophyllite and montmorillonite. Both clays have a 2:1 layered structure in which the outer layers are silicon tetrahedrally (T) coordinated to oxygen and the inner layer is aluminum octahedrally (O) coordinated to oxygen. Each of these aluminum octahedral cages contains one oxygen atom that is also bound to a hydrogen atom to form a structural hydroxyl group. These hydroxyl groups are connected to either the top or bottom of the octahedron in a regular alternating pattern. These layers arrange as repeating TOT sheets which weakly coordinate across a hydrated interlayer region via van der Waals interactions. Pyrophyllite, an aluminosilicate with the formula $AlSi_2O_5(OH)$, differs from montmorillonite only in the occupancy of its cationic sites. In montmorillonite, partial

substitutions of magnesium in the place of octahedral aluminum induce a net negative charge on the structure which is counterbalanced by aqueous cations in the interlayer. In this work, we choose to use Na^+ as the counterion, but also include equally proportioned Na^+/Cl^- pairs to provide a statistically viable sample of ion trajectories to analyze. Montmorillonite can also exist with aluminum substitutions in the tetrahedral silicon layer, but the effect of $Al_{Si}^{'}$ substitutions is outside the scope of this work. Experimentally, both clays are observed to be monoclinic, but prior works have shown that they can be approximated as orthorhombic in simulation without significantly impacting the dynamics of the system[136], [137]. Single crystal X-ray diffraction data by Lee and Guggenheim [139] measures the *a* and *b* lattice parameters of pyrophyllite to be 5.16 Å and 8.97 Å respectively. The *c* axis spans the width of the interlayer region and is thus sensitive to water content; for a dehydrated system the measured value is 9.35 Å.

To best understand the interactions between ions and clay edges in a variety of local environments, we devise four unique simulation cells: three montmorillonite systems with unique arrangements of isomorphic $Mg_{Al}^{'}$ substitutions and a pyrophyllite system which serves as a charge neutral reference state. Each system consists of three layers of trans-vacant dioctahedral (empty octahedral site situated on the mirror plane) phyllosilicate clay sheets, three water-saturated interlayers, and a central bulk water mesopore which, in addition, contains all the Na^+ and Cl^- ions at system initialization (Figure 5-1). The clay sheets are cleaved to expose the 110A termination described by Lavikainen et al. [140]. This termination is consistently reported as one of, if not the most, favorable edge termination by prior theoretical works [138], [141], [142], [143],

[144], [145], [146]. However, unlike prior works on phyllosilicate edge structures [134], [143], we do not apply additional -OH or -H groups to heal the undercoordinated edge atoms. We instead rely on the Na^+ and Cl^- ions in the system to neutralize any localized charge on the edge surfaces. After equilibration, the (100) d-spacing between clay sheets is measured to be 18.9 +/- 0.1 Å, the length of the simulation cell measured along the width of the mesopore is 96.5 +/- 0.2 Å, and the depth measured parallel to the edge surfaces is 46.7 +/- 0.2 Å. These dimensions are comparable to the 3WL system analyzed by Tournassat et al. [134]. Each montmorillonite system contains 96 $Mg_{Al}^{'}$ substitutions, which corresponds to a net charge of -0.33 e/u.c.. A unit cell consists of two $Al_{0.833}Mg_{0.167}Si_2O_5(OH)$ formula units and has the same lattice dimensions as pyrophyllite. Recent experimental characterization work by Qiu et al. [147] has shown the unit cell charge density of montmorillonite to be in the range of -0.69 to -0.38 e/u.c. Increasing the number of substitutions to create a charge density which is representative of the experimental value would require substitution sites to be placed outside of the distinct locations that are of interest in this work. Therefore, we choose to use a substitution scheme which produces a charge density that is as close as possible to the experimental range but still allows for analysis of the effect of the substitutions' precise location. The pyrophyllite system contains 180 Na^+/Cl^- ion pairs and 5978 water molecules to form a concentration of 1.47 mol/dm^3 which is equivalent to 37% of the solubility limit in water at 298.15 K [148]. In the montmorillonite systems, an additional 96 Na^+ ions are included to neutralize the net negative charge induced by $Mg_{Al}^{'}$ substitutions which brings the total concentration up to 45% of the solubility limit. This corresponds to individual ion concentrations of 1.47 mol/dm^3 for Cl^- and 2.25 mol/dm^3

for Na^+. A higher concentration than is necessary for charge neutralization is chosen to provide ample data in the resulting simulated trajectories.

The three montmorillonite systems under investigation in this work are referred to as MMT-central, MMT-edge, and MMT-equidistant. The suffix describes the arrangement of $Mg_{Al}^{'}$ substitutions within the clay sheet. In the MMT-central system all substitutions are localized to the center of the interlayer region, i.e., as far away as possible from the mesopore edge. In the MMT-edge system the opposite scenario is investigated as substitutions are placed directly on the terminated clay edges. The MMT-equidistant system represents an intermediate case in which the substitutions are evenly spaced throughout the sheets so as not to create a highly localized charge density at the edge or in the center.

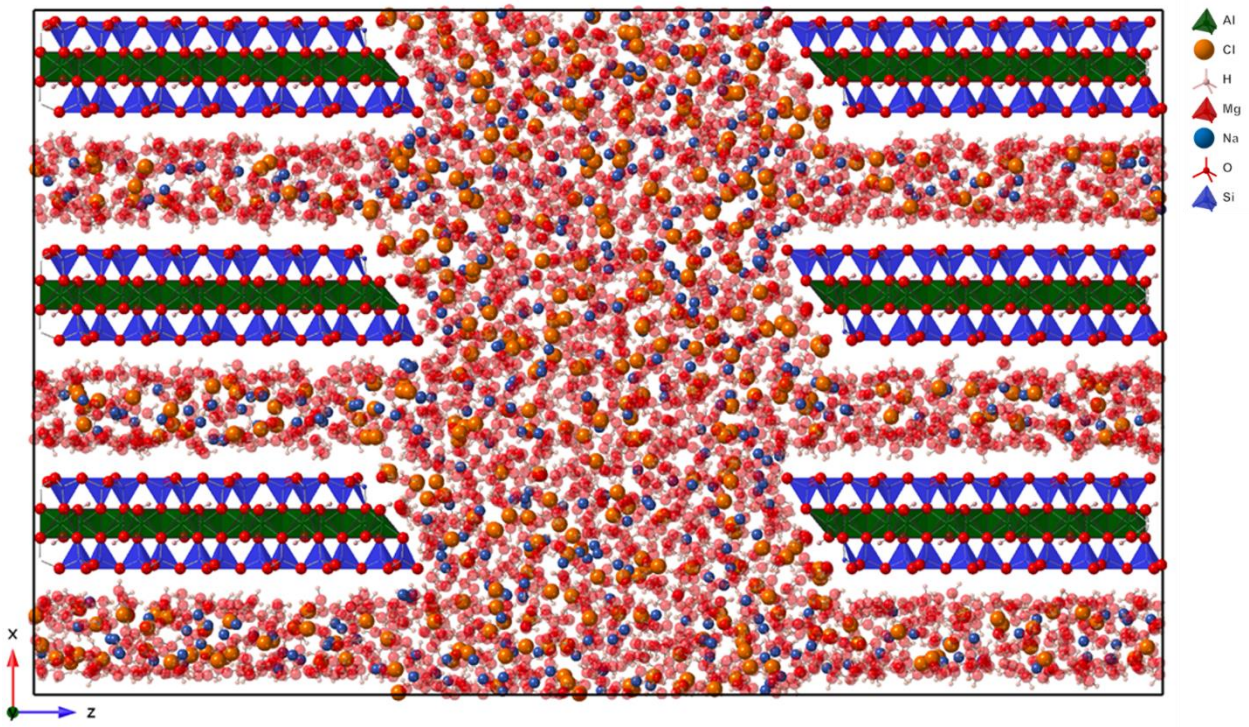

Figure 5-1. Snapshot of the fully equilibrated pyrophyllite simulation cell. For clarity, the water molecules are rendered with low opacity. Atom types illustrated as follows: Na^+ (blue), Cl^- (orange), O (red), Octahedral Al (green), Tetrahedral Si (blue), H (pink).

5.2.2 Molecular Dynamics Simulations

All molecular dynamics simulations in this work were executed in LAMMPS [149], [150] and all initial atomic coordinate files were generated using the Moltemplate software package [151]. The mesopore and interlayer regions were packed with 1.0 g/cm^3 of water and the Na^+/Cl^- ions were arranged on a grid in the mesopore and allowed to diffuse out during equilibration so as not to preemptively bias the composition of the interlayers. Interactions within the clay sheet were modeled using the CLAYFF potential developed by [152]. Water in the mesopore and interlayer regions was modeled using the SPC/e potential of [153] with the SHAKE algorithm [154] turned off. Our preliminary benchmark calculations showed that disabling SHAKE results in better agreement with experimental measurements of bulk water diffusivity. Lennard-Jones parameters for aqueous Na^+ and Cl^- ions were adopted from the work of Smith and Dang [155]. Non-bonded interactions between dissimilar species were fit using LAMMPS' arithmetic mixing strategy. Coulombic contributions were evaluated using the Ewald sum method. The boundaries of the simulation cell were treated as periodic in all dimensions. Therefore, when we describe phenomena occurring in the "center" of the clay sheet, they will appear on the far left and right of the visible simulation cell because the cell is centered on the mesopore.

Equilibration was carried out in multiple phases. The first was an energy minimization step in which the total energy is converged to a tolerance of 10^{-6} kcal/mol. Using the energy minimized system as a starting point, a simulation in the NVT ensemble was run for 2.0 ns with a timestep of 0.5 fs and a target temperature of 300 K. During this first NVT phase only water molecules were allowed to move. Then, a second 2.0 ns phase was conducted in which both ions and water molecules were allowed to

move freely. Following the NVT phase, an NPT simulation was conducted for another 2.0 ns, again using a timestep of 0.5 fs, with a pressure target of 1 atm and a temperature target of 300 K. During the NPT phase the volume of the cell was allowed to relax anisotropically. Throughout all equilibration phases the clay sheets were made rigid using the LAMMPS fix *setforce,* following the precedent set by similar works [156], [157], [158]. This implementation allows the constant pressure algorithm to optimize the interlayer spacing without shifting atoms in the clay sheet relative to each other. Benchmark calculations showed that when the rigid constraint was not applied during equilibration the clay sheets would oscillate in a wave-like motion that did not settle down over the course of the equilibration. It is expected that this effect is an artifact of system size, and the simulations would eventually stabilize if a wider clay sheet were investigated; however, the computational cost of such large simulations is prohibitive. After equilibration the *setforce* restriction was applied only to the octahedral sheet to allow more flexibility in the basal planes. The production simulations were conducted in the NVT ensemble for a duration of 10 ns using a timestep of 0.5 fs and a temperature target of 300 K.

5.3 Results

5.3.1 Spatial Distribution of Na^+ and Cl^- Ions

In this chapter, we provide a qualitative overview of the features in each clay model that are evident from visual inspection of the ionic trajectories. In subsequent chapters, we build upon these observations with quantitative analyses to robustly characterize the behavior of ions across each environment. Figure 5-2 illustrates the MD trajectories of the Na^+ (blue) and Cl^- (orange) ions over the course of a 10 ns production simulation in NVT. Green points highlight the position of the octahedral Al

layer. In montmorillonite systems, red ‘X’s denote the positions of Mg_{Al}' substitution sites within the octahedral layer. All other species have been excluded from this visualization. Vertical dashed lines delineate the interlayer/mesopore boundary (IMB) which we defined as the position of the outermost oxygen on the clay edge termination. The figure is composed by superimposing the *xz*-plane projected positions of each ion in 200 snapshots exported every 50ps. The positions are plotted with low opacity at each snapshot so that regions which accumulate ions appear as bright hotspots and regions with a lower ion density appear to be more dispersed. Each subplot corresponds to a unique system.

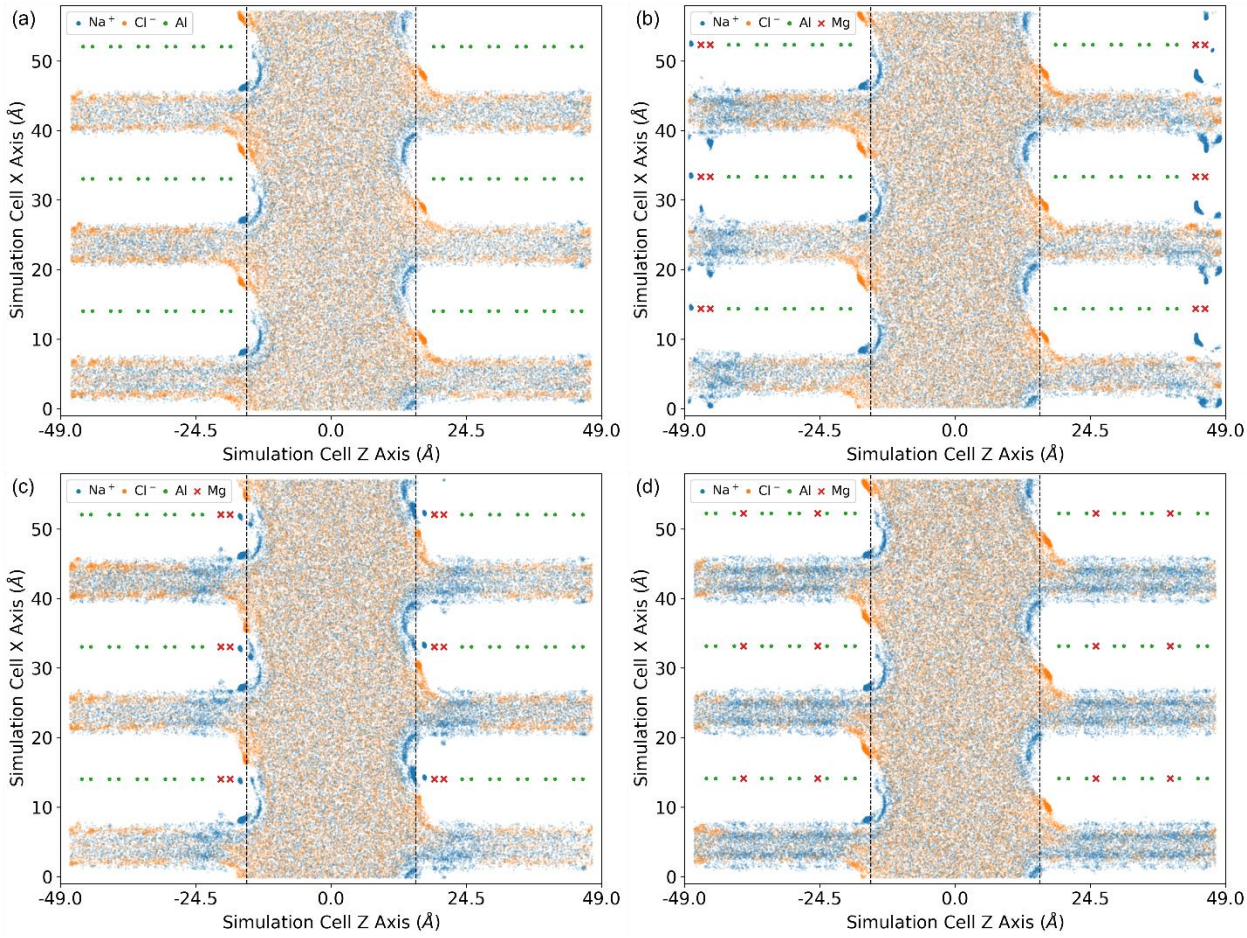

Figure 5-2. Positions of Na^+ (blue) and Cl^- (orange) ions projected onto the *xz*-plane of the simulation cell. Positions taken from 200 snapshots over the course of a 10 ns NVT simulation are superimposed. Octahedral Al is shown in green and $Mg_{Al}^{'}$ substitutions are denoted by red 'X's. The vertical dashed lines represent the interlayer mesopore boundary. Each subplot corresponds to a unique system: (a) Pyrophyllite, (b) MMT-central, (c) MMT-edge, (d) MMT-equidistant.

One feature evident in all subplots of Figure 5-2 is the agglomeration of both Na^+ and Cl^- ions on each edge termination, just outside of the IMB. This feature is most clearly illustrated in Figure 5-2a which depicts pyrophyllite. A symmetrical split of Na^+ density around the leading edge (projecting into the mesopore) and Cl^- density near the trailing edge is consistent with our choice to leave any dangling bonds created during the edge cleavage unhealed. This finding is also supported by prior work from Ta et al. [146] in which density functional theory calculations report a negative partial charge on

the undercoordinated oxygen on the leading edge and a positive partial charge on the undercoordinated Si on the trailing edge. In Figures 5-2b-d, the impact of $Mg_{Al}^{'}$ substitutions on the distribution of ions can be clearly contrasted with their distribution in the charge neutral pyrophyllite system.

Figure 5-2b illustrates the MMT-central system. This system has the highest charge density (four substitutions in close proximity due to periodic boundary conditions) and its substitutions are located furthest from the IMB. In this system we observe Na^+ ions adsorbing onto the outer tetrahedral layer of the clay sheet. Visualizations of a typical arrangement of the adsorbed Na^+ ions in this cluster in MMT-edge are provided in Figure 5-3. Note that because the simulation cell is periodic in all dimensions, there are four substitution sites directly adjacent along the *z*-axis in each clay sheet. We observe that the ions are drawn towards the basal oxygen nearest each substitution site and occasionally penetrate the basal plane in the center of the four aligned substitutions where charge density is highest. Furthermore, it is evident that in the interlayer region adjacent to the adsorbed Na^+ ions, small but dense clusters of Cl^- ions form to neutralize the localized charge density. However, these anions remain solvated in the interlayer.

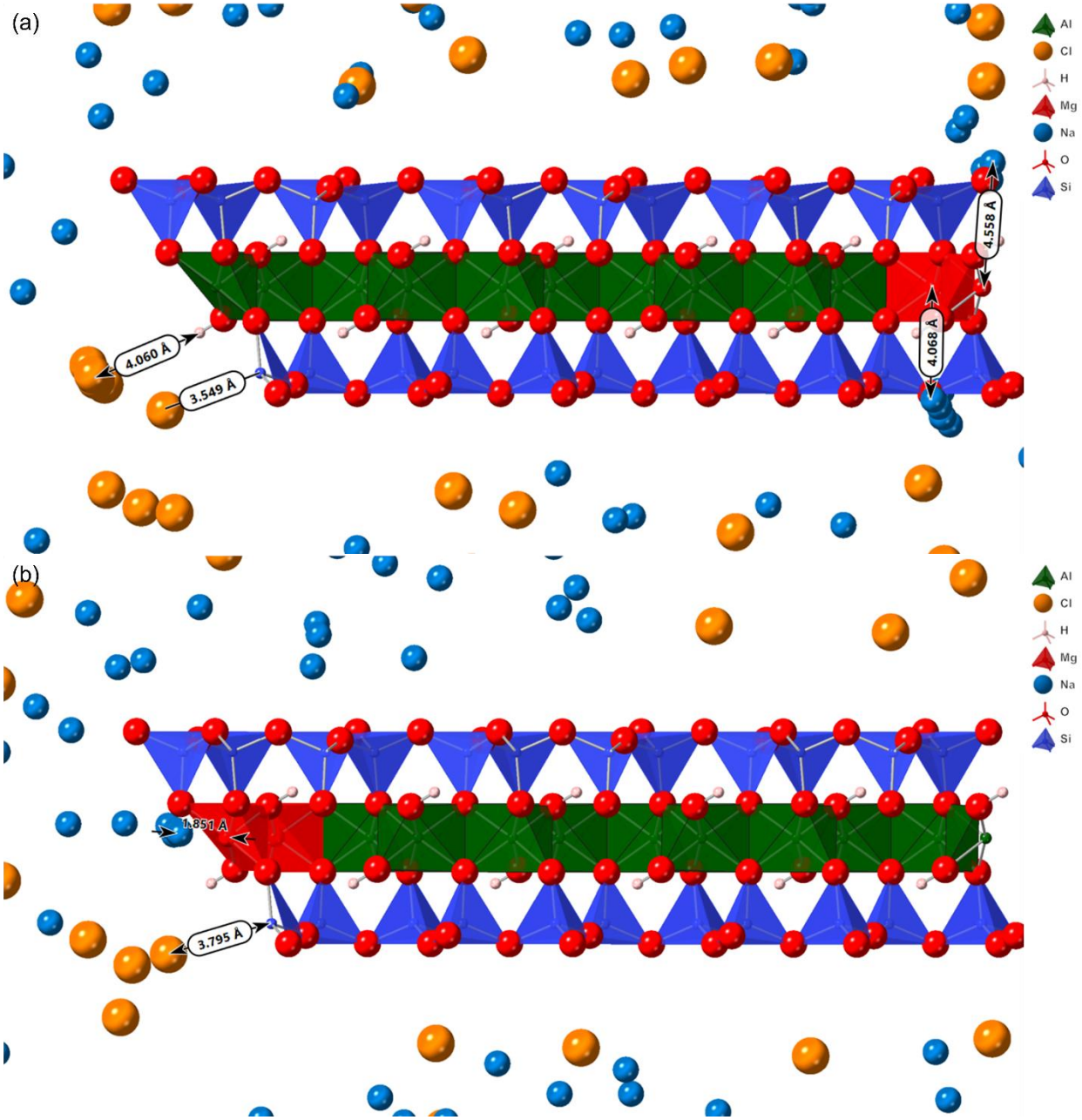

Figure 5-3. Snapshot of MMT-central (a) and MMT-edge (b) during the production simulation. Distances between dense clusters of ions and local sources of charge have been annotated.

Figure 5-2c, which details the MMT-edge system, is the opposite to the previously discussed MMT-central system in that its substitution sites are as close as possible to the IMB. This arrangement results in a lower charge density because the substitutions on each side of the mesopore are no longer adjacent through the periodic

boundary, but similar features are identifiable. Clusters of Na^+ ions along the basal plane in the interlayer nearest to the Mg_{Al}' substitution sites are still evident. These cations undergo a similar adsorption process in which they densely cluster around the basal oxygen atoms nearest each substitution site, but full penetration into the tetrahedral sheet is never observed. The interior interlayer regions adjacent to these surface adsorbed ions do not form the same dense charge-compensating clusters of Cl^- ions observed in the MMT-central system. Additionally, there is a markedly diminished amount of Na^+ ions in the deep interlayer region on account of the lack of electrostatic driving force past the IMB.

The third montmorillonite system we considered, MMT-equidistant, is presented in Figure 5-2d. Although having the same overall number of substitutions, this case represents the lowest charge density (aside from neutral pyrophyllite) due to the large distance between substitution sites. Additionally, this system's substitutions are evenly spread between the IMB and central interlayer region which offers an interesting opportunity to study the behavior of ions outside the range of influence of the edge termination. Perhaps most evident in Fig. 5-2d is the lack of Na^+ adsorption onto the clay's basal planes which is seen in other montmorillonite systems. Na^+ ions in this system tend to form a diffuse cloud in the interlayer region centered around each substitution site rather than converging to a fine point. There is no agglomeration of Cl^- ions in the interlayer to counterbalance the presence of Na^+ and the distribution of ions near the edge terminations is not visually distinguishable from that of pyrophyllite.

5.3.2 Relative Abundance of Na^+ and Cl^- Ions

To complement the explicit ion trajectories presented in Chapter 5.3.1, Figure 5-4 offers a more quantitative view of each system of interest by plotting the difference

between the populations of Na^+ and Cl^- ions across the span of the simulation cell. This is accomplished using kernel density estimation (KDE) to produce a probability density function (PDF) for each ionic species. More specifically, Gaussian distributions are centered on each ionic position and summed together to create a function defined over the range of the simulation cell which when integrated between appropriate bounds returns the probability of finding an ion of that species in those bounds. To indicate a relative excess of one species or another, we subtract the PDF representing Cl^- from that of Na^+ to get a single curve which is positively valued when more Na^+ is present and negatively valued when more Cl^- is present. One technical detail which is important to note is that the values have been weighted relative to the bulk Na^+:Cl^- ratio. This does not impact pyrophyllite where the bulk ratio is 1:1, but in the montmorillonite systems where Na^+ outnumbers Cl^- 1.53:1 to charge balance the $Mg_{Al}^{'}$ substitution sites, this normalization has a significant effect. In summary, for Na^+ to appear in excess of Cl^- in Figures 5-4b-d, the Na^+:Cl^- ratio must exceed 1.53:1.

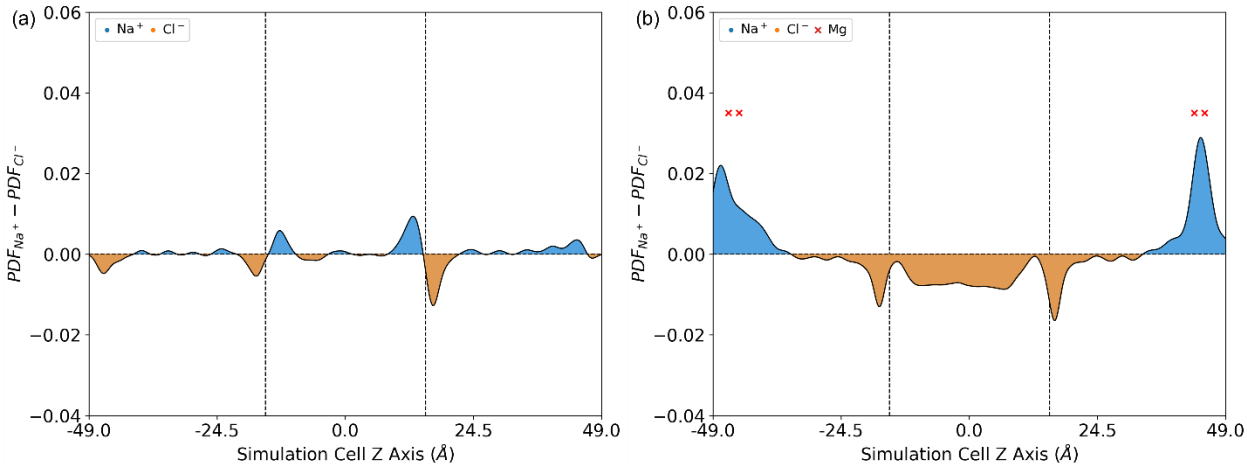

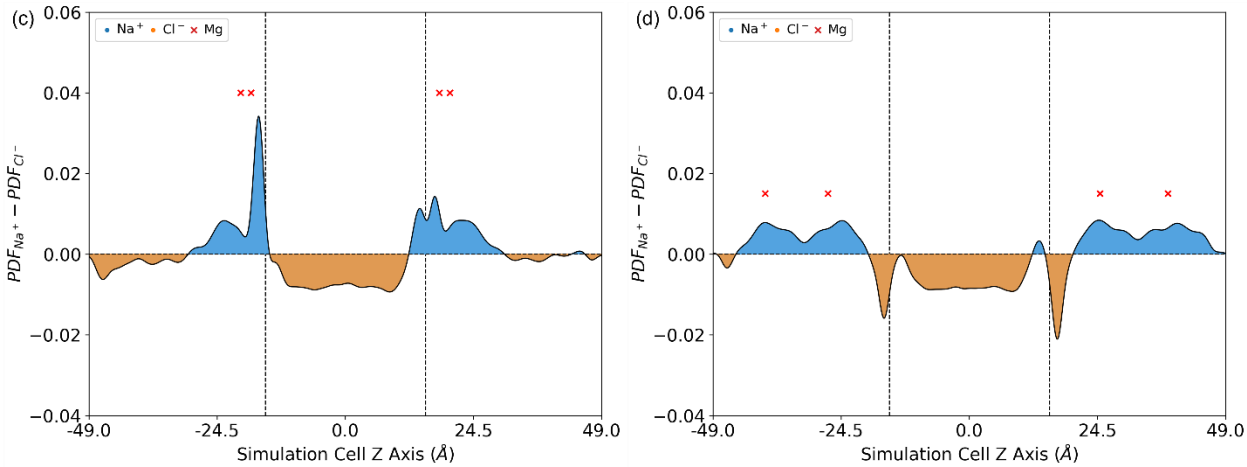

Figure 5-4. Relative amounts of Na^+ and Cl^- ions projected along the *z*-axis of the simulation cell. Regions shaded in blue denote an excess of Na^+ while regions shaded in orange denote excess Cl^-. Vertical dashed lines indicate the IMB and red X's represent the positions of Mg_{Al}' substitution sites. Each subplot corresponds to a unique system: (a) pyrophyllite, (b) MMT-central, (c) MMT-edge, (d) MMT-equidistant.

In Figure 5-4a, it is evident that deviation from the bulk Na^+:Cl^- ratio in pyrophyllite only occurs near the edge terminations. Around the IMB, symmetrical peaks are observed for both ionic species. Na^+ (blue) tends to congregate on the outer edge nearest the mesopore while Cl^- (orange) tends to favor the inner edge nearest the interlayer. This arrangement is expected because the outer edge exposes a negatively charged undercoordinated basal oxygen and the inner edge exposes a positively charged undercoordinated tetrahedral silicon. Small fluctuations around zero occur in both the interlayer and mesopore which is the expected behavior due to a lack of any electrostatic driving force that may otherwise bias the distribution. These small fluctuations would be expected to decrease in magnitude even further with longer time averaging.

The MMT-central system, illustrated in Figure 5-4b, contains a significant excess of Na^+ in the deep interlayer, consistent with our qualitative analysis of Figure 5-3b. Intense peaks centered at the substitution sites reflect the necessity to neutralize the

high local charge density in that region. This accumulation of Na^+ at substitution sites leads to a net exclusion of Cl^- ions from the interlayer region, as can be seen by the excess of Cl^- present throughout the mesopore. Additionally, a change in the ion distribution around the IMB is expressed as an elimination of the Na^+ peaks present in the neutral pyrophyllite system. The Cl^- peaks in the same region, however, are similar in magnitude to those found in pyrophyllite and the mesopore contains excess Cl^-.

In Figure 5-4c, a significant increase in the magnitude of Na^+ peaks near the IMB can be observed for the MMT-edge system. Interestingly, the size of the peaks centered on the interlayer side of the substitution sites are quite small relative to those found in MMT-central, but their location near the edge termination seems to have an outsized effect on the height of Na^+ peaks at the IMB. This system produces sharp spikes in excess Na^+ similar to those found near Mg_{Al}' substitutions in the MMT-central system. Cl^- is again found to be in excess throughout the mesopore, however, small peaks can be found to favor the anion in the deep interlayer region outside of the influence of the edge termination and substitution sites, indicating that there is not total exclusion.

Lastly, Figure 5-4d depicts MMT-equidistant as having a more diffuse distribution of Na^+ in the interlayer relative to other montmorillonite systems. The short broad peaks reflect the same diffuse presence of Na^+ ions centered around substitution sites as is observed in Figure 5-2d. The interlayer is almost entirely devoid of regions which favor Cl^- indicating a strong tendency for anion exclusion. This tendency is further supported by the sharp Cl^- peaks near the IMB which are larger in magnitude than similarly located peaks in all other systems.

5.3.3 Localized Concentration of Na^+ and Cl^- Ions

To further characterize the composition of each system, the concentration of both Na^+ and Cl^- are projected along the width of the simulation cell in Figure 5-5. Concentration is plotted relative to the baseline value of pyrophyllite and montmorillonite systems respectively. Recall that the pyrophyllite system is packed with ions to achieve 37% of the solubility limit of water, but in montmorillonite systems additional Na^+ ions are needed to neutralize $Mg_{Al}^{'}$ substitution sites, bringing the concentration to 45% of the solubility limit. This type of analysis differs from the Na^+:Cl^- discussed in Chapter 5.3.2, because it also takes into consideration the presence of water throughout the system. The prior analysis is valuable in highlighting regions where there is distinct charge polarity due to an excess of a single ion type, but an analysis of concentration helps identify regions that tend to accumulate or exclude both ion types. Crucially, concentration profiles can identify regions as being more or less concentrated than the bulk solution which is a conclusion that could not be drawn directly from the data in Chapter 5.3.2. Measurements of concentration are discretized by dividing the simulation cell into 25 bins along its *z*-axis and calculating the concentration for each volume element.

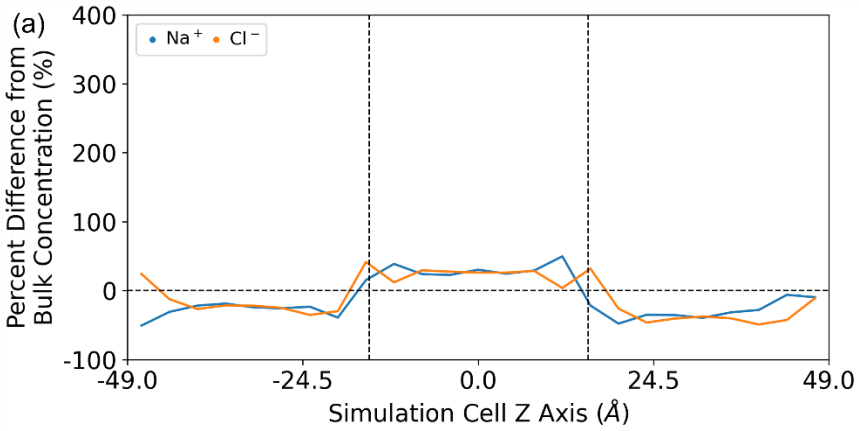

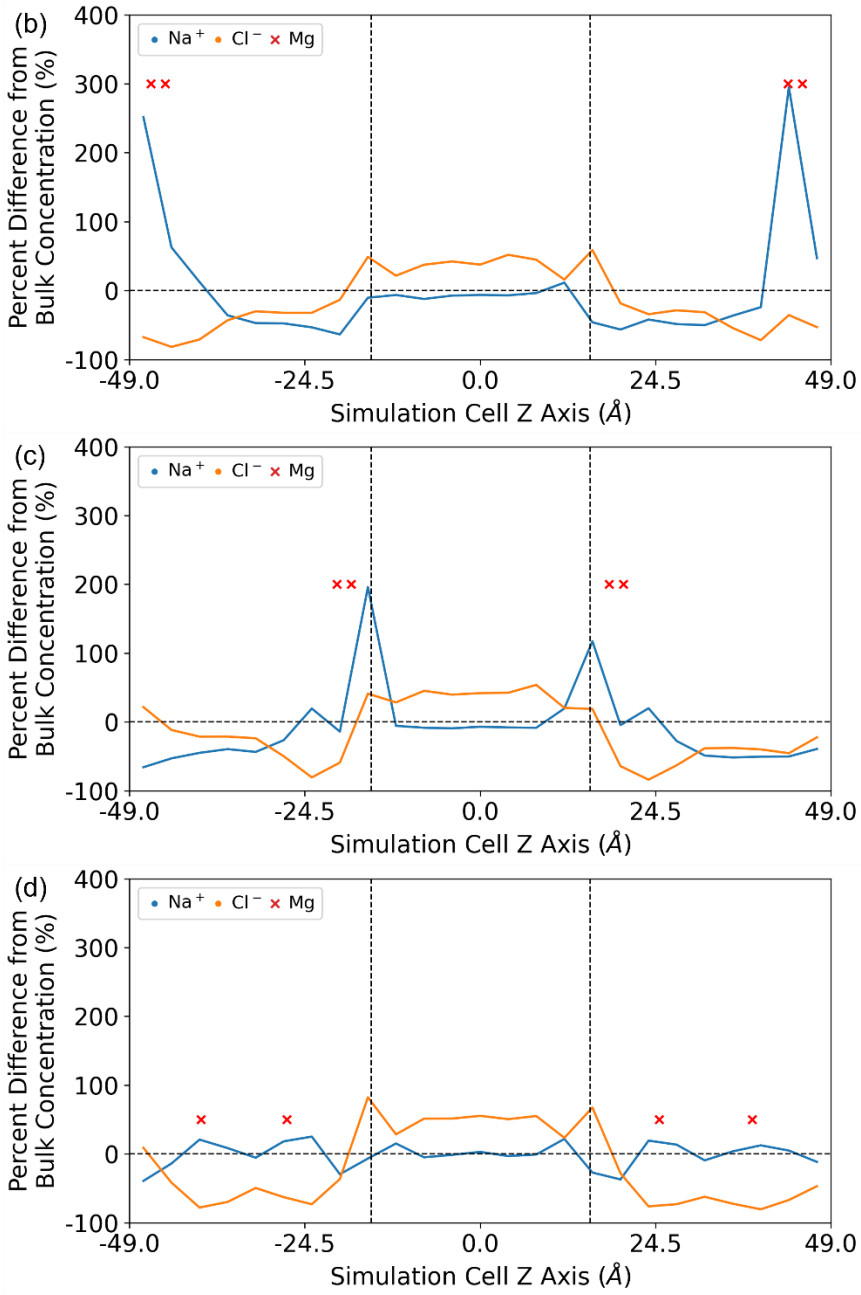

Figure 5-5. Concentration of Na^+ (blue) and Cl^- (orange) ions relative to their bulk values projected along the *z*-axis of the simulation cell. Vertical dashed lines denote the IMB and red 'X's represent the positions of Mg_{Al}' substitutions. Each subplot corresponds to a unique system: (a) pyrophyllite, (b) MMT-central, (c) MMT-edge, (d) MMT-equidistant.

One trend which becomes evident from inspection of Figure 5-5a is the tendency for the ion concentrations in the interlayer to be lower than in the mesopore. The concentration of the two ions is nearly identical throughout the simulation cell except for

the near-IMB region where Na^+ and Cl^- peaks separate and reach concentrations far greater than the bulk value. This behavior closely resembles that identified in Figure 5-4a where the Na^+ peaks are closer to the mesopore on the leading edge of the IMB and the Cl^- peaks are positioned closer to the interlayer.

Concentration profiles in the MMT-central system (Figure 5-5b) retain the strong Na^+ peaks around Mg_{Al}' substitution sites found in Figure 5-4b. However, this visualization shows that Cl^- concentration rises only slightly in the same region indicating that the observed compensating clusters in the adjacent interlayer are more diffuse. Throughout the remainder of the interlayer, concentrations of both ions remain below the bulk concentration. In the mesopore, Na^+ is found to be at bulk concentration levels while Cl^- is in excess.

The MMT-edge concentration profiles presented in Figure 5-5c display sharp peaks of both Na^+ and Cl^- near the IMB. On the interior side of the IMB, directly adjacent to the Mg_{Al}' substitution sites, a significant drop in the concentration of Cl^- is observed. This finding contrasts with the behavior of the MMT-central system where Cl^- accumulates with Na^+ at the substitution sites to neutralize local charge density. This behavior is likely due to the presence of strongly adsorbed Na^+ ions on the edge surface which act as a sink for incoming Cl^- anions that would otherwise be drawn deeper into the interlayer. Throughout the interlayer, the concentration of both ions remains below the bulk value although Cl^- tends to be higher than Na^+ after the initial drop at the substitution sites. In the mesopore, Cl^- concentration is found to be in excess of the bulk value.

In Figure 5-5d, the MMT-equidistant concentration profile is unique in that the Na^+ concentration in the interlayer is only slightly greater than the bulk value near substitution sites. Despite the presence of Mg_{Al}' substitution sites which provide an electrostatic driving force for Na^+ to cluster in the interlayer, the cation is found in nearly equal proportion within the mesopore and near the edge terminations. The behavior of Cl^- near substitution sites is like that of the MMT-edge profile; Cl^- is clearly disfavored near substitutions and has a significant decrease in concentration where Na^+ concentration rises. The concentration of Cl^- rises higher than Na^+ near the IMB although the peaks are identical in location to those found in pyrophyllite.

5.3.4 Residence Time of Adsorbed Na^+ and Cl^- Ions

In order to capture the dynamical behavior of these phyllosilicate clay systems at edge surfaces and substitution sites, Figure 5-6 reports the distribution of residence times of ions in equally sized slices along the simulation cell. Residence times are derived from ion trajectories exported every 1ps over the course of the final 1ns of simulation time. A residence event begins when an ion enters a bin it did not occupy in the prior snapshot and continues until the ion moves to another bin. Each event for each ion is reported in Figure 5-6. which means that there are more data points than ions because most ions pass through multiple bins over the course of the simulation. When interpreting these results, it is important to consider how the geometry of the simulation cell intersects with the boundaries of each bin. For bins in the interlayer, the clay sheets reduce the total traversable volume. This reduction in traversable volume is not present for mesopore bins. The effect of this difference is that residence times in the interlayer are artificially lower than those in the mesopore because ion motion in the interlayer is primarily two dimensional while ions in the mesopore have a full range of motion. We do

not expect this effect to hinder the analysis of residence times because it is not strong enough to mask the electrostatic interactions between ions and substitution/edge sites as evidenced in Figure 5-6. Furthermore, it is important to note that the dominant residence time in all bins is just 1 ps because that is the minimum step size and the ions are flowing freely. To highlight the more interesting longer residence events, a curve is superimposed over each subplot which represents the 95th percentile residence time for each ion type in each bin.

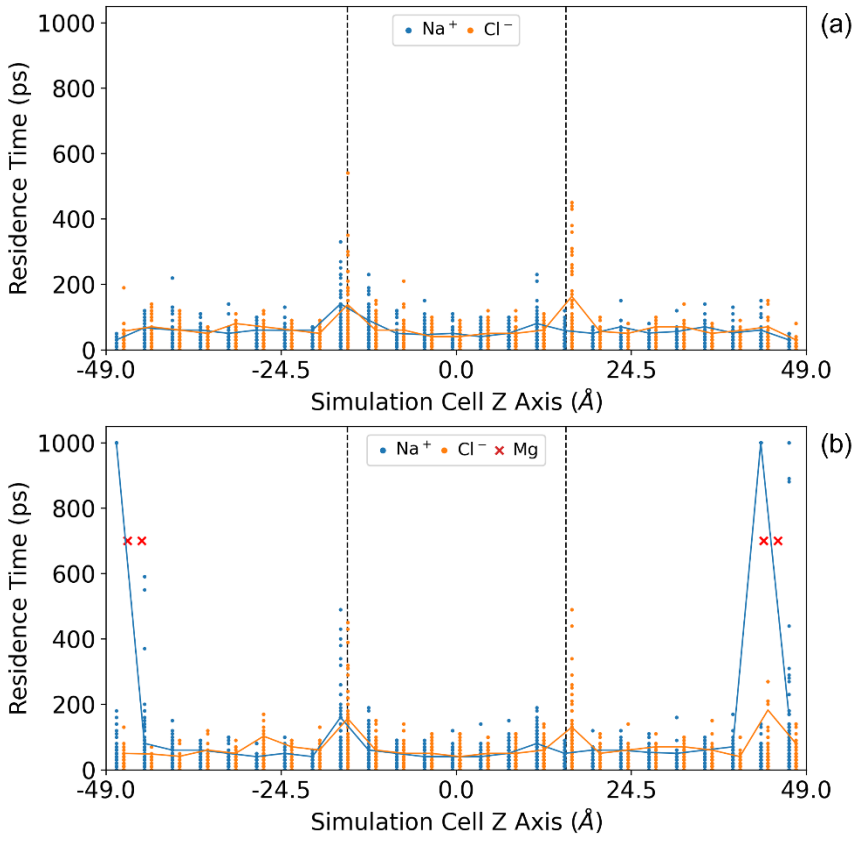

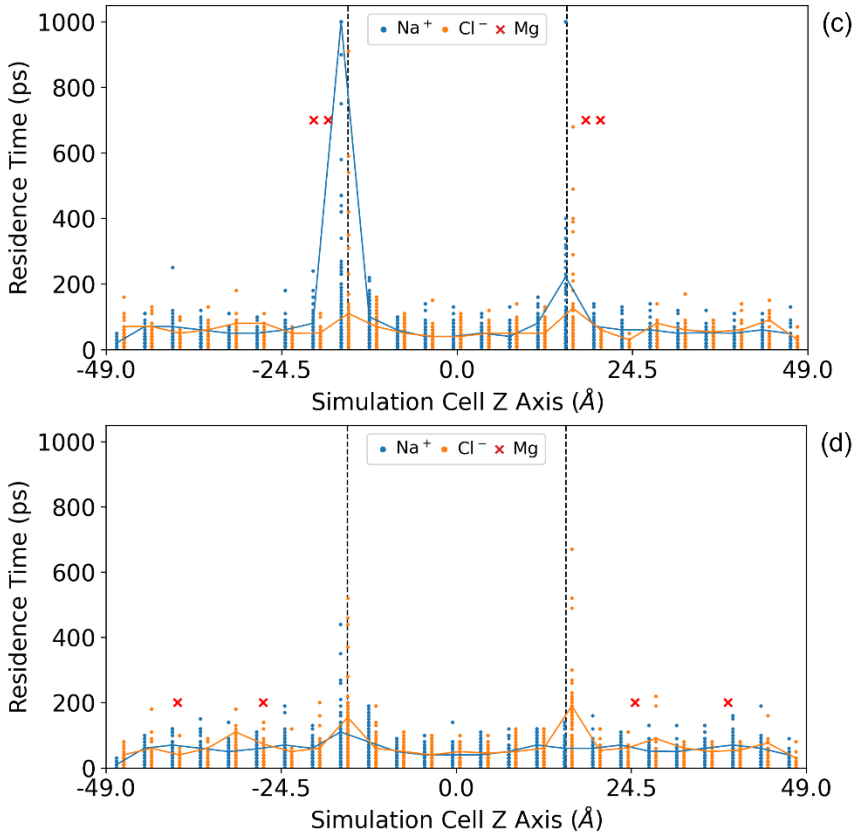

Figure 5-6. Residence times of Na^+ (blue) and Cl^- (orange) ions projected along the *z*-axis of the simulation cell. Residence times are calculated in 25 equally sized bins. For clarity, Na^+ and Cl^- data points have been offset from each other about the center of each bin. Vertical dashed lines denote the IMB and red 'X's represent the positions of $Mg_{Al}^{'}$ substitutions. Each subplot corresponds to a unique system: (a) pyrophyllite, (b) MMT-central, (c) MMT-edge, (d) MMT-equidistant.

In all subplots of Figure 5-6 we find that a small number of Cl^- ions remain adsorbed to the edge surface for at least 400 ns. This finding is consistent with the bright hotspot of Cl^- on the trailing edge of each clay sheet presented in Figure 5-2. Interestingly, the residence times of both ions are not always equal despite similar hotspots for each shown in Figure 5-2. While it is expected that both Na^+ and Cl^- will tend to congregate at edge surfaces to heal the undercoordinated oxygen and silicon atoms respectively, we propose that the difference in residence times between Cl^--Si and Na^+-O pairs is due to geometric features of the edge structure. Based on the

CLAYFF parameters which drive these simulations, the magnitude of the partial charge on the undercoordinated basal oxygen and the undercoordinated tetrahedral silicon are equivalent. Pairing this with the fact that equilibrium distances between both pairs are similar, we can eliminate differences in electrostatic interaction strength as a contributing factor. Recalling the arrangement of the edge structure from Figure 5-3, it can be seen that the undercoordinated oxygen projects out into the mesopore and is highly exposed to water while the undercoordinated silicon is largely insulated by the overhanging edge of the clay sheet and is accessible only through a small concave region adjacent to the interlayer. Therefore, it follows that Na^+ ions being drawn to the undercoordinated oxygen would be more frequently carried away by highly mobile water molecules than their less exposed Cl^- counterparts.

In the pyrophyllite system (Figure 5-6a), residence times throughout the interlayer and mesopore are consistently less than 200 ps. It is only near the IMB that prolonged residence is observed. Aside from the small set of strongly interacting Cl^- outliers, Na^+ ions tend to reside on the edge for a maximum of 300 ps and less strongly bound Cl^- ions for a maximum of 500 ps. Furthermore, it is evident that residence times of both species are elevated in the mesopore bins directly adjacent to those centered on the IMB. However, the same effect is not observed on the interlayer side of the IMB. This suggests that the electrostatic influence of the edge terminations extends approximately 4 Å into the mesopore and asymmetrically affects mesopore ions.

Figure 5-6b illustrates how $Mg_{Al}^{'}$ substitutions in the MMT-central system significantly increase the residence times of Na^+ ions in the interlayer. A small number of Na^+ ions adjacent to substitution sites remain static for the full 1 ns duration of the

data collection period. In addition to this small group of strongly interacting ions, Cl^- ions in the same region are observed to also increase in residence time to over 200 ps – more than twice the value recorded throughout the rest of the interlayer. This increase in Cl^- residence time reflects the presence of the charge compensating clusters of Cl^- ions adjacent to Na^+ interlayer adsorption sites shown in Figure 5-2b. Near the IMB, residence times are consistent with those observed in pyrophyllite.

When substitutions are placed on the edge surface, the differences in residence time profiles relative to the neutral pyrophyllite system can only be distinguished along the IMB. Along the edge surface, a select number of Na+ cations are observed to remain adsorbed for the full 1 ns data collection period. In Figure 5-6c, residence times for both ionic species are observed to peak near the IMB and remain below 200ps throughout the rest of the system. A more subtle difference from Figure 5-6a is that the increased residence times near the IMB are no longer asymmetrically distributed on the mesopore side, but now extend into the interlayer side as well. This behavior is expected due to the presence of the $Mg_{Al}^{'}$ substitutions driving cations to congregate in the interlayer just past the trailing edge of each clay sheet termination. Another difference from the pyrophyllite case is that the ions in the MMT-edge system tend to produce a wider range of residence times. In pyrophyllite, there are very few points above 300ps aside from the IMB adjacent Cl^- ions, but in MMT-edge the distribution is split more evenly between 0 and 1000ps for both ionic species.

In Figure 5-6d, the presence of evenly distributed substitution sites in the MMT-equidistant system produces a profile of residence times that are almost identical to those found in pyrophyllite. Even in bins containing $Mg_{Al}^{'}$ sites, the residence times for

either ion do not exceed 200ps Near the IMB, the same trends are observed where a select few Cl^- ions tend to remain adsorbed at the edge surface for over 500 ps while Na^+ ions are more mobile and have a peak residence time of approximately 400 ps. Figure 5-6d illustrates that the low charge density associated with this arrangement of substitutions is insufficient to retain ions in the interlayer.

5.4 Discussion and Conclusions

Comparing the results across each system of interest, we observe that localized charge density is the primary driving force controlling the distribution of ions. Two sources of charge, unhealed edge terminations and $Mg_{Al}^{'}$ substitution sites, control the electrostatics in each system. The distribution of ions around edge terminations is broadly consistent with Na^+ favoring the leading edge of each termination (closest to the mesopore) and Cl^- congregating on the tailing edge (closest to the interlayer). However, the magnitude of ion clusters at clay edges can be influenced by the presence of $Mg_{Al}^{'}$ substitutions. As evidenced by Figures 5-4c and 5-5c, the MMT-edge system sequesters a greater amount of Na^+ ions at edge terminations than all other systems due to the presence of charged substitutions in close proximity. In other montmorillonite systems where substitution sites are placed far from the edges, the distribution and number of ions adsorbed on the edge facets is close to that of the charge neutral pyrophyllite system. Substitution sites, alternatively, may be positioned in order to drive an influx of ions into the interlayer. High charge density in the MMT-central systems leads to not only an influx of Na^+, but also a secondary cluster of Cl^- which serves to counterbalance the cations adsorbed to the tetrahedral layer of the clay sheet. In the MMT-equidistant system, which is lower in charge density, such strong accumulation of Na^+ is not observed which in turn eliminates the need for a secondary cluster of

compensating Cl^-. In fact, from inspection of Figures 5-4d and 5-5d, the MMT-equidistant system is found to exclude Cl^- from the interlayer more so than any other. When residence times are considered, it becomes clear that both the pyrophyllite (Figure 5-6a) and MMT-equidistant (Figure 5-6d) systems fail to capture ions in the interlayer for any significant duration. Alternatively, the MMT-central system is capable of drawing ions into the interlayer and sequestering them on the order of 1ns as can be seen in Figure 5-6b. Interestingly, MMT-central is capable of retaining not only Na^+ as we would expect from simple electrostatic interactions, but also Cl^- which is observed to have elevated residence times approaching 200ps. This suggests that a higher layer charge may be necessary to adsorb ions using a montmorillonite clay base if special care is not taken to design the sheet in such a way that substitutions tend to be clustered.

In the context of clay buffer materials, these results help us better understand the criteria to consider when manufacturing or modifying the base clay. We have shown that even without any octahedral substitutions in the clay sheet, exposed edge surfaces are able to consistently sequester both cations and anions from solution. This finding suggests that during processing, it may be optimal to minimize the volume of individual clay particles in a suspension so that the maximal amount of surface area is exposed and available for ions to adsorb to. However, strides may still be made to improve sequestration performance within the interlayer. Our simulations predict that an even distribution of substitution sites throughout a clay sheet significantly underperforms a sheet in which the substitutions are clustered close together despite both sheets having the same net layer charge. While this may be a more difficult variable to tune from a

synthesis perspective, the finding opens the door to future research into methodologies that can offer better control over the precise arrangement of substitutions in the octahedral layer. Furthermore, this work does not consider how Al_{Si}' substitutions in the tetrahedral layer may change the sequestration performance of the clay. In future work, an investigation into this additional substitution type or a combination of both tetrahedral and octahedral substitutions may paint a fuller picture of ion capture in hydrated phyllosilicate clay edge models.

By comparing simulations of distinct clay edge models with varying electrostatic environments, the effect of both unhealed edge surfaces and Mg_{Al}' substitution sites on ion sequestration can be characterized. It is evident that regardless of the distribution or presence of octahedral substitution sites, edge terminations can effectively retain both anionic and cationic species. In the absence of additional local charge from substitution sites these edge terminations can adsorb ions for durations on the order of 400 ps. However, the inclusion of nearby substitutions drastically increases the performance to 1 ns which was the longest duration tested. Furthermore, particular arrangements of octahedral substitutions can contribute to varying levels of ion concentration and selectivity in the interlayer. The arrangement found to limit Cl^- penetration most was the evenly distributed MMT-equidistant which was found drastically reduced Cl^- concentration in the interlayer relative to the mesopore. An alternative high local charge density configuration, MMT-central, was found to draw both Na^+ and Cl^- into the deep interlayer and effectively retain Na^+ ions for up to 1 ns. As expected, charge neutral pyrophyllite was identified as the least selective in controlling specific ion concentrations in the interlayer.

These findings are valuable in the context of radionuclide sequestration. Building on the results of this work, two key design considerations for clay buffer materials have been identified: maximizing exposed surface area can result in enhanced sequestration performance under any substitution conditions, and evenly distributed substitutions in the interlayer enhance anion exclusion relative to systems with high localized charge density.

CHAPTER 6
CHARACTERIZATION OF THE INTERLAYER STRUCTURE OF ALKYLAMMONIUM FUNCTIONALIZED ORGANOCLAY FROM MOLECULAR DYNAMICS SIMULATION

6.1 Background

Clay buffer materials have been proposed as a solution to limit radionuclide transport through nuclear waste containers [159]. Montmorillonite, a member of the smectite group, has desirable properties for this application including high surface area, low permeability, and significant swelling capacity [160]. However, due to the net negative charge of montmorillonite induced by Mg_{Al}' substitutions in the octahedral sheet, functionalization is required to modify the surface charge and promote the capture of anions [159]. Anion capture is a requirement in this application because of the specific interest in capturing pertechnetate (TcO_4^-). The Technetium-99 in pertechnetate is a long-lived fission product in waste generated by plutonium production [162]. The pertechnetate anion is highly water soluble (11.3 M) and mobile in the environment due to its negative charge which largely prevents capture via sediment or mineral sorption [163]. One functionalization strategy which has been shown to drastically improve anionic radionuclide sequestration relative the base clay is organoclay synthesis [14]. Organoclays substitute the charge neutralizing inorganic interlayer cations for larger organic cations such as alkylammonium. The driving force behind this improved radionuclide sequestration is proposed to be an ion exchange method whereby a reversal in surface charge displaces hydrated metal ions thus changing the hydrophilicity of the interlayer [12], [164].

Characterizing the structure of these functional alkylammonium cations upon saturating the clay interlayer can provide valuable insight into the mechanisms driving radionuclide adsorption. Two prior MD studies consider the confinement of linear

alkylammonium cations of varying chain length into a montmorillonite interlayer [165], [166]. Both studies observe that the interlayer structure evolves from lateral monolayer at low %C to paraffin monolayers at the highest %C tested. Zeng et al. [167] consider a dioctadecylmethyl ammonium cation under similar circumstances and find that a pseudoquadrilayer structure develops when the concentration of alkylammonium is chosen to be 1:1 with the cation exchange capacity. In each of these prior works, only one class of alkylammonium is investigated. However, recent experimental results using quaternary chained alkylammonium display high Tc sequestration performance suggesting that the branchedness of the alkylammonium may change the interlayer structure even between molecules with the same total carbon content [14]. Therefore, in this work, we address a knowledge gap in the literature by using MD simulation to compare the equilibrium interlayer structure across different alkylammonium configurations and concentrations. The impact on interlayer spacing, alkylammonium orientation relative to the basal plane, and interlayer ordering are all considered to develop a comprehensive understanding of the role that carbon content, chain length, and branching have in controlling the interlayer structure.

6.2 Simulation Cell and Computational Methodology

6.2.1 Simulation Cell

The simulation cell used in the work contains a single sheet of montmorillonite consisting of 100 unit cells arranged in a 10 × 10 grid. The dimension of the sheet measures 54.9 Å by 47.5 Å along the *x* and *y* axis, respectively. The sheet contains a total of 60 near-uniformly distributed Mg_{Al}^{-} substitution sites producing a net charge of –0.6 e/u.c. which is consistent with recent experimental measurements [147]. Alkylammonium molecules were packed in the interlayer region at ratios of 0.5:1,

0.75:1, 1.0:1 alkylammonium molecules per Mg_{Al}^{-} substitution site to assess the effect of interlayer carbon content on interlayer spacing and alkylammonium orientation. In the 0.5:1 and 0.75:1 systems, the excess charge was neutralized by adding bare Na^{+} cations into the interlayer region. Water molecules were intentionally excluded from the interlayer to reflect experimental measurements indicating that little to no water is found in the interlayer [168]. This system treatment is also commonly used by prior MD studies on montmorillonite-alkylammonium interactions [165], [166], [167], [169].

6.2.2 Computational Methodology

All molecular dynamics simulations were performed using LAMMPS [149], [150]. The initial atomic coordinate files were prepared using the Moltemplate and PACKMOL software packages [151], [170]. The CLAYFF potential was employed to model interactions within the clay sheet while the GAFF2 potential was used to parameterize alkylammonium molecules [152], [171]. The charge compensating Na^{+} ions were treated with the Lennard-Jones parameters of Smith and Dang [155]. Lorentz-Berthelot mixing rules were used for the cross-terms. Simulations were broken into multiple stages proceeding in the following way: an energy minimization step with a tolerance of 1×10^{-6} kcal/mol, 10 ns in the *NVT* ensemble at a constant temperature of 500 K and a pressure of 1 atm, a *NPT* quench from 500 K to 300 K lasting 1 ns, and finally another 1 ns in the *NPT* ensemble at the final temperature of 300 K. Interlayer spacing was taken to be the average value during the final 1 ns of simulation time. After the volume had been fully relaxed in the final *NPT* stage, an additional 1 ns in the *NVT* ensemble at 300 K was conducted during which atomic trajectories were exported every 10 ps to determine the orientations of alkylammonium molecules.

6.3 Results

6.3.1 Interlayer Spacing

The interlayer spacing was calculated for each organoclay using MD and compared to experimental XRD measurements to provide insights into the alkylammonium molecules within the clay structure. *NPT* simulations were conducted to relax the total cell volume. The (001) interplanar distance values can be extracted from the relaxed cells and compared to experimental measurements as shown in Table 6-1. XRD and FTIR measurements from literature cannot provide quantitative information on how many alkylammonium chains are present in the clay interlayer, therefore, MD was used to determine the interlayer spacing as a function of different alkylammonium to Mg_{Al}^{-} ratios (Table 6-1).

Table 6-1. Simulated interlayer spacing as a function of alkylammonium:Mn_{Al}^{-} substitution ratio compared to experimental values. All values reported in nm.

Ammonium Cation	0.5:1 Ratio	0.75:1 Ratio	1.0:1 Ratio	Experimental
1 × 4	1.44	1.43	1.42	1.42
3 × 4	1.51	1.60	1.76	1.44
5 × 4	1.82	1.92	2.25	1.78
9 × 1	1.48	1.51	1.79	1.42
16 × 1	1.53	1.89	2.21	1.82

For longer chained molecules, the 1.0:1 alkylammonium to Mg_{Al}^{-} ratio tends to result in a larger interplanar distance than experimental measurements. Overall, the 0.5:1 ratio yields interplanar distances closest to the experimental measurements, suggesting that the clay is not achieving full charge neutrality from alkylammonium incorporation alone, and must rely on additional ions in solution to compensate for the Mg_{Al}^{-} substitutions in the clay sheet. The long-chained 16 × 1 alkylammonium deviates from this trend, with the ratio of 0.75:1 resulting in a simulated interplanar distance that is closest to the experimental measurement. As with the experimental values, the predicted interplanar

distance for the organoclay with the 1 × 4 alkylammonium cation (1.42 nm) is very similar to that for the unfunctionalized SWy-3 (1.45 nm), and the d_{001} does not change significantly with extent of substitution. This is different from the trend observed for larger alkylammonium ions, where a higher extent of alkylammonium substitution results in a narrower interlayer. The consistency between experiment and simulation suggests that, at low chain lengths, the alkylammonium molecules constrict the interlayer region. This could be caused by hydrogen bonding between the alkylammonium cation and the basal oxygen present in the clay sheet. At higher chain lengths the increased molecule size dominates - driving the interlayer to expand.

6.3.2 Alkylammonium Orientation

To understand the arrangement of alkylammonium molecules in the interlayer environment, MD trajectories were used to calculate the angles formed between alkyl chains and the montmorillonite clay sheet. A unit vector normal to the surface of the clay sheet is used as a reference vector. Carbon chains that are parallel to the surface have a calculated orientation angle of 90° when compared to the reference vector. A vertical chain would be at 0° or 180° depending on if the carbon or nitrogen side faces down, respectively. This scheme is depicted visually in Figure 6-1.

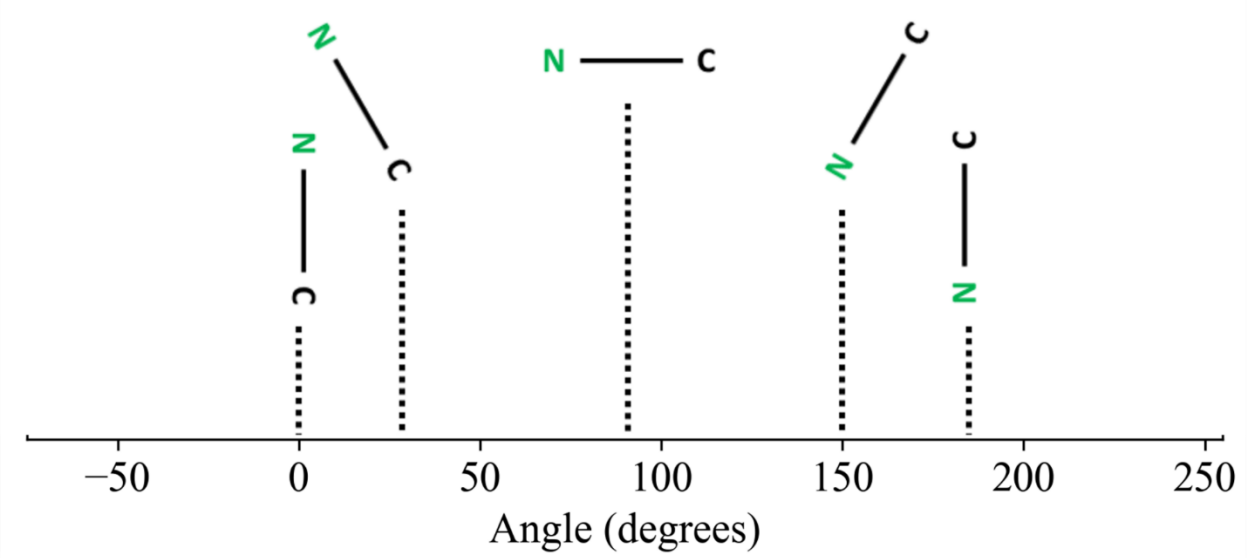

Figure 6-1. Diagram depicting the relationship between the calculated orientation angle and physical carbon chain orientation.

To provide a comprehensive picture of these orientations, we construct a distribution of angles from each carbon chain in each alkylammonium molecule over 100 snapshots exported 10ps apart during 1ns of NVT simulation at 300K. One technical challenge that arises from this analysis is the uniformity of carbon chains in each molecule. If one were to simply average all angles from all chains in all molecules together, the resulting distribution loses information associated with the particular arrangement of a single chain. To address this, we sort the orientation angles from high to low on a per-molecule basis before adding them to the distribution which is associated with their sorting rank. Put more simply, the lowest angle chains of each molecule are members of the same distribution and the highest angle chains are members of the same distribution, but those two distributions are entirely distinct from each other. This solution produces a number of distributions equal to the number of longest chains in each alkylammonium under consideration.

The organoclay with 9 × 1 alkylammonium molecules is representative of the behavior observed with linear configuration, and the organoclay with 5 × 4 organoclays alkylammonium molecules is representative of the behavior observed for a quaternary branched configuration. The chain orientation angles for both the 1.0:1 (solid) and 0.5:1 (dashed) alkylammonium to Mg_{Al}^{-} ratio are shown for the 5 × 4 alkylammoniums (Figure 6-2) and 9 × 1 alkylammoniums (Figure 6-3).

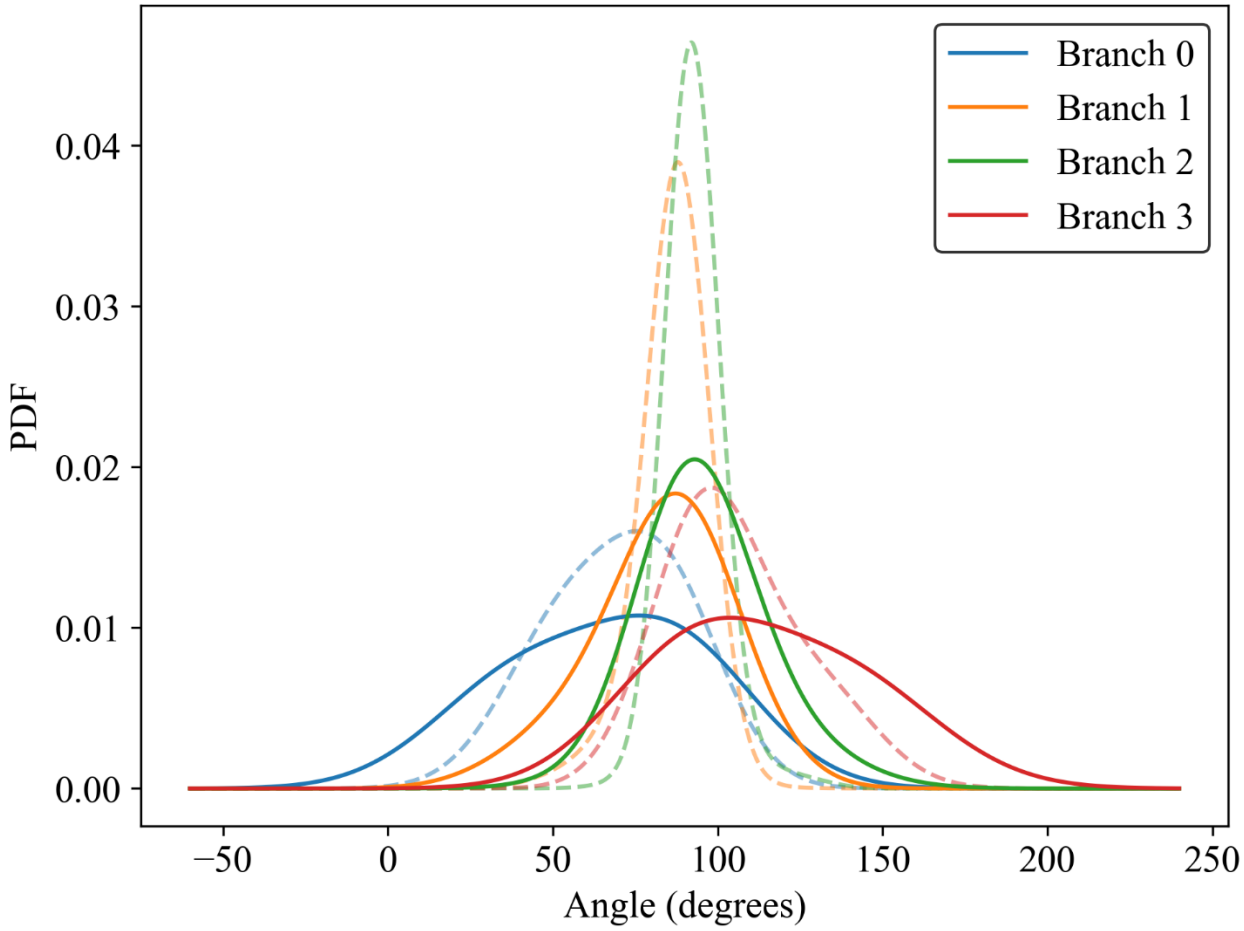

Figure 6-2. Distribution of carbon chain orientation angles relative to a vector normal to the surface of the clay sheet for the 5 × 4 alkylammonium. An angle of 90° indicates that the chain is parallel to the surface while an angle of 0° or 180° indicates verticality. The solid lines plot data from the 1.0:1 ratio system and the dashed lines plot data from the 0.5:1 ratio system.

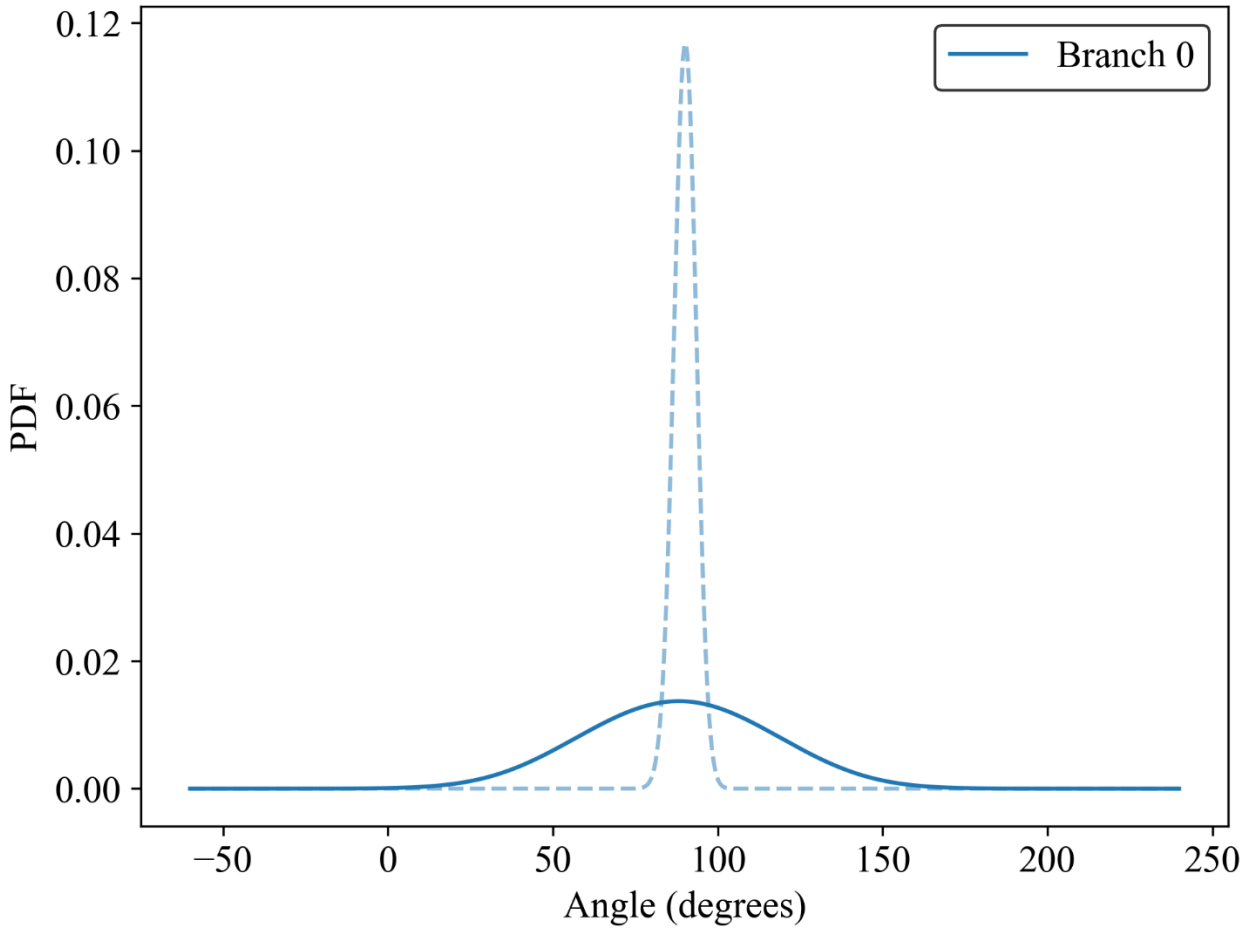

Figure 6-3. Distribution of carbon chain orientation angles relative to the surface of the clay sheet for the 9 × 1 alkylammonium. An angle of 90° indicates that the chain is parallel to the surface while an angle of 0° or 180° indicates verticality. The solid lines plot data from the 1.0:1 ratio system and the dashed lines plot data from the 0.5:1 ratio system.

Figure 6-2 exhibits segmentation of the four chains into two groups: one parallel chain centered at 90° and one vertical distribution with equal preference for either the C or N to be facing the clay sheet. The distribution suggests that, for the 5 × 4 alkylammonium, two alkyl chains are flat in the interlayer plane, with the remaining two chains oriented diagonally across the interlayer. The alkylammonium concentration alters the orientation angle, with the 0.5:1 resulting in the angle distributions producing a narrower peak at 90°. The different orientation at a lower concentration suggests that steric effects drive the alkylammonium molecules to shift from a horizontal arrangement

at low concentration to a vertical arrangement with increased packing density at a higher concentration. The MD derived mass density measurements of the interlayer volume for each system are presented in Table 6-2 and support the conclusion that higher alkyl content results in a more densely packed interlayer.

Table 6-2. Density of the interlayer region as a function of alkylammonium:Mg_{Al}^{-} substitution ratio from MD simulation data. All values reported in g/cm^3.

Ammonium Cation	0.5:1 Ratio	0.75:1 Ratio	1.0:1 Ratio
1 × 4	0.07	0.13	0.22
3 × 4	0.14	0.26	0.37
5 × 4	0.15	0.29	0.40
9 × 1	0.14	0.29	0.37
16 × 1	0.20	0.29	0.39

The distribution of orientation angles for the linear 9 × 1 alkylammonium is illustrated in Figure 6-3, with one chain per molecule. In both the 1.0:1 and 0.5:1 systems the chains are oriented parallel to the clay sheet. Similar to the 5 × 4 system, a tighter distribution around 90° exists for the 0.5:1 ratio compared to the 1.0:1 ratio. The distribution indicates the linear alkylammonium undergoes horizontal ordering at low concentrations and is forced in a higher concentration system to be diagonally oriented to increase the packing density.

6.3.3 Interplanar Layer Ordering

The tendency for the alkylammonium molecules in the interlayer to form monolayer or bilayer configurations has been evaluated using XRD and MD [169], [172]. A distribution of nitrogen positions along the *z* axis of the simulation cell that corresponds to the direction spanning the interlayer was collected with 100 snapshots exported 10 ps apart during 1 ns of *NVT* simulation at 300 K after volume relaxation. The distributions of nitrogen for the 5 × 4 and 9 × 1 alkylammoniums are presented in Figure 6-4 and Figure 6-5, respectively.

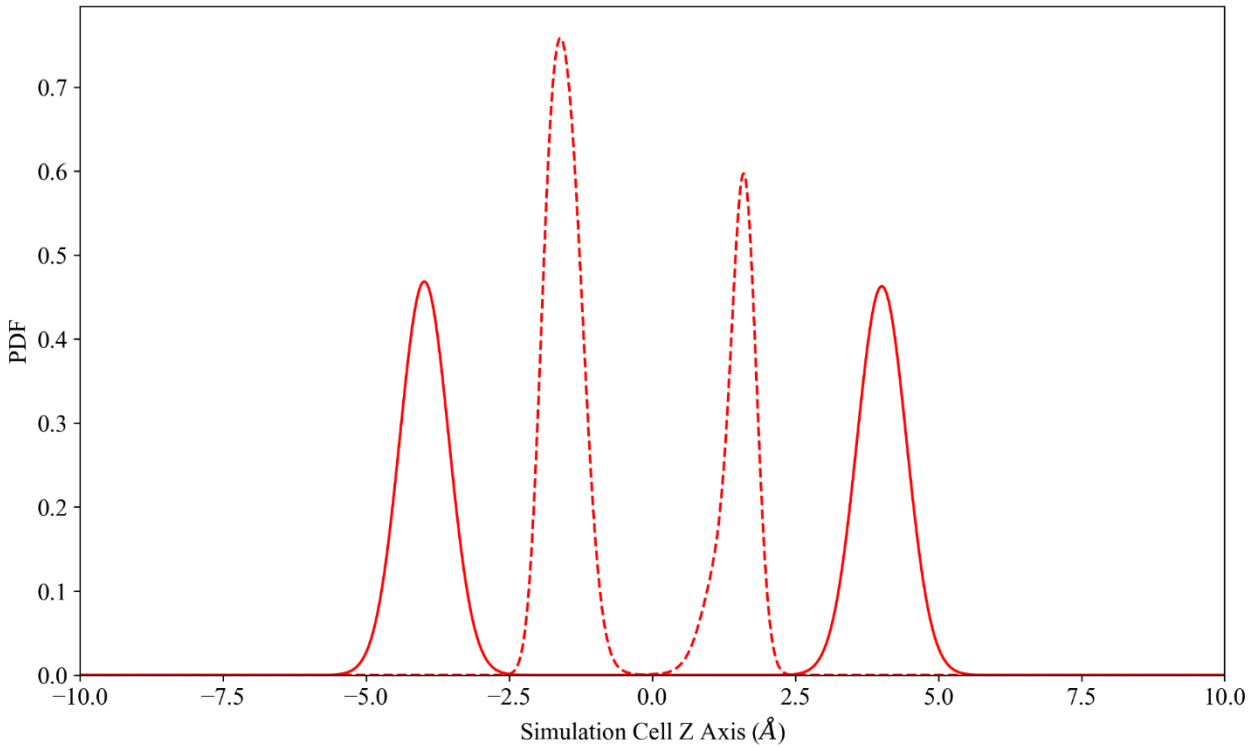

Figure 6-4. Distribution of nitrogen within the interlayer for the 5 × 4 alkylammonium. The solid lines plot data from the 1.0:1 ratio system and the dashed lines plot data from the 0.5:1 ratio system.

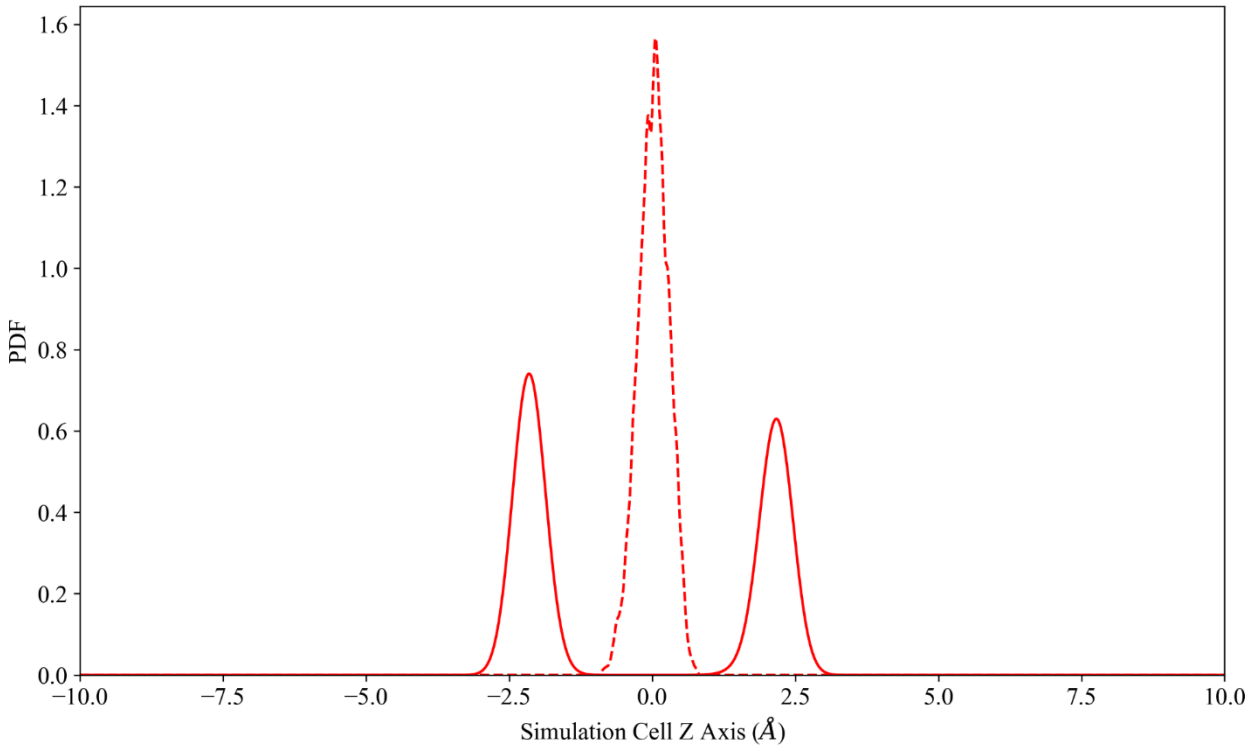

Figure 6-5. Distribution of nitrogen within the interlayer for the 9 × 1 alkylammonium. The solid lines plot data from the 1.0:1 ratio system and the dashed lines plot data from the 0.5:1 ratio system.

Figure 6-4 indicates that the 5 × 4 alkylammonium tends to form a bilayer at both low (0.5:1) and high (1.0:1) concentrations. At low levels of substitution, the two layers are closer together than the high levels of substitution. However, distance between alkylammonium N centers and the basal O plane remains fairly constant as shown in Table 6-3.

Table 6-3. Average distance between alkylammonium N centers and the nearest basal O as a function of alkylammonium:Mg_{Al}^{-} substitution ratio from MD simulation data. All values reported in nm.

Ammonium Cation	0.5:1 Ratio	0.75:1 Ratio	1.0:1 Ratio
1 × 4	0.37	0.33	0.34
3 × 4	0.36	0.41	0.38
5 × 4	0.37	0.35	0.33
9 × 1	0.36	0.39	0.30
16 × 1	0.41	0.32	0.31

The tendency for bilayer formation is expected, as the 5 × 4 alkylammonium has a large surface area that prevents molecules from packing into a single plane, even at low levels of substitution. The linear 9 × 1 alkylammonium molecules tend to form a monolayer at low levels of substitution, and a bilayer at high levels of substitution. This can be interpreted from the nitrogen distribution presented in Figure 6-5 or the simulation snapshot illustrated by Figure 6-6. The change in layer orientation of the linear alkylammonium molecules as the substitution increases is consistent with the lower surface area of the linear alkylammonium. The computational designation of mono– and bi–layer ordering is consistent with the experimental XRD and FTIR data.

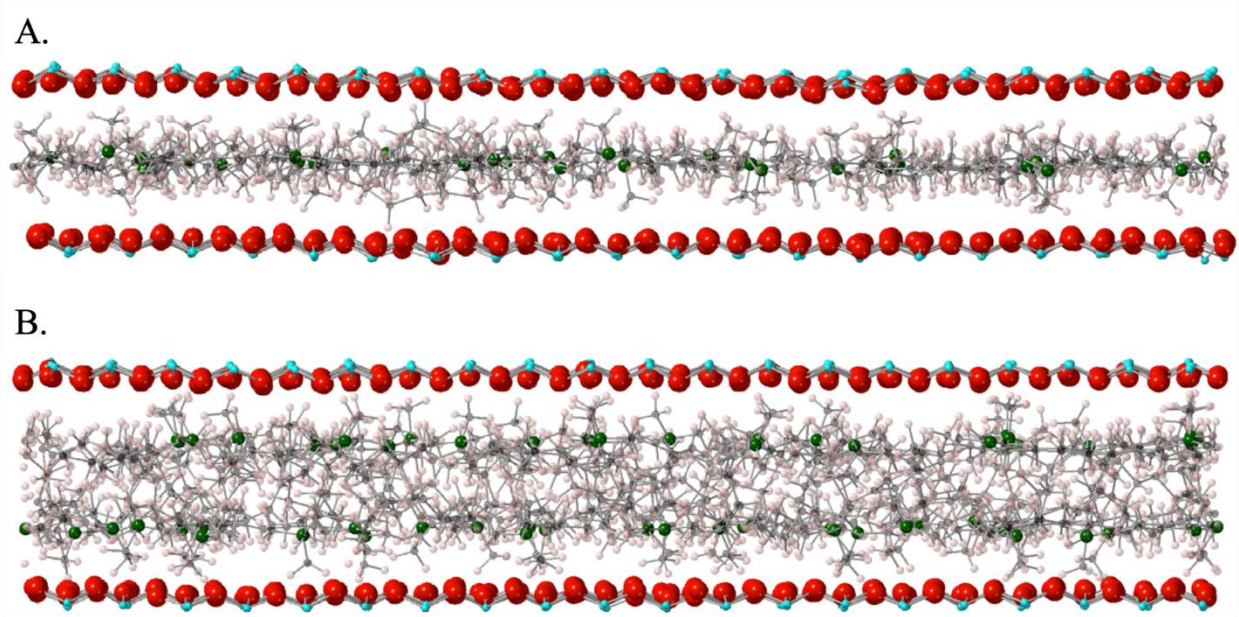

Figure 6-6. Visualization of monolayer (A.) and bilayer (B.) alkylammonium orientation in the montmorillonite interlayer for the 9 × 1 alkylammonium using data gathered from MD simulations. Red atoms are oxygen, blue atoms are silicon, green atoms are nitrogen, black atoms are carbon, and pink atoms are hydrogen. Opacity of hydrogen and carbon have been reduced for clarity and only the basal layer of clay has been included.

6.4 Discussion and Conclusions

The current work uses well-established MD methods to investigate the interplay of alkylammonium chain length, branching, and total carbon content on the interlayer

structure of a montmorillonite clay. Simulations of equilibrated interlayer spacing as a function of alkylammonium content are consistent with prior MD literature which expectedly predicts a positive correlation between interlayer spacing and %C. Unique to this study is the finding that the interlayer spacing as simulated by MD is closest in agreement to experimental measures of the same alkylammonium system when the simulations contain 50% of the alkylammonium content required for charge neutralization. This suggests that alkylammonium in the synthesized organoclay is not fully saturating the interlayer or exchanging every available inorganic cation. This effect may partially be explained by the presence of locally charged clay edge surfaces that act as sinks for the incoming alkylammonium molecules. Measurement of orientation angle relative to the basal plane offers a high-resolution view into the arrangement of different alkylammonium systems. At low concentrations, the carbon chains tend to flatten out and align themselves parallel to the basal plane. As more alkylammonium molecules are incorporated into the interlayer, the carbon chains deviate from parallel to produce a broader distribution of orientation angles. In quaternary chained alkylammonium systems at higher concentrations, the molecules assume a distinct “tilt” arrangement whereby two of the chains remain close to horizontal and the remaining two extend outwards towards the basal plane on one side and the central interlayer on the other. This change in orientation coincides with an increase in interlayer density revealing that the clay sheet is rigid enough to impose some degree of order on the alkylammonium molecules despite accommodating significant interlayer swelling. Characterization of mono/bilayer ordering in each system agrees with prior MD works which all observe an evolution from monolayer to bilayer and beyond as %C increases.

In this work specifically, we identify a pseudo-trilayer ordering at the highest alkylammonium concentration. This ordering scheme is characterized by N-centers segregating to the basal planes and carbon chains extending out into the interlayer to form a densely overlapping network in the center. Chain size is observed to have a significant impact on ordering with the 16 x 1 alkylammonium assuming a bilayer arrangement even at the 0.25:1 concentration.

In conclusion, a variety of linear and quaternary alkylammonium molecules of specific sizes which have not been previously studied are simulated in a montmorillonite interlayer environment and characterized with regards to their equilibrium interlayer structure. Trends in interlayer spacing agree with prior MD work on other linear alkylammoniums, but direct comparison to experiment suggests that the organoclay as synthesized does not contain fully saturated interlayers. Orientations of carbon chains relative to the clay basal plane predict a strongly parallel arrangement at low concentrations with a shift to a unique “tilted” orientation which crowds the interlayer as alkylammonium concentration increases. Ordering for all but the largest alkylammonium structures is favored to be monolayer at the lowest concentration measured. As alkylammonium content increases to full saturation, a pseudo-trilayer is observed for quaternary and long-chained linear alkylammonium molecules. Although a high-quality potential for pertechnetate was not available for this work, a future study analyzing the (TcO_4^-)-alkylammonium interaction in the presence of a confining montmorillonite interlayer could significantly advance the mechanistic understanding of the radionuclide sequestration process.

CHAPTER 7
PREDICTING SHORT RANGE ORDER IN HIGH ENTROPY Li-OXIDE CATHODE MATERIALS WITH DENSITY FUNCTIONAL THEORY AND CRYSTAL GRAPH CONVOLUTIONAL NEURAL NETWORKS

7.1 Background

Improvements in the energy density of Li-ion batteries are hindered by a lack of reliable high-capacity cathode materials [16], [173]. Current battery designs depend on a limited set of layered transition metal oxides [174], but recent literature has demonstrated that Li-excess disordered rocksalt (DRX) materials enable rapid Li transport and offer a much broader compositional space for cathode design [15], [175], [176], [177], [178]. This discovery has been bolstered by the emerging field of high-entropy (HE) materials development. The concept of combining multiple elements in equimolar proportion to form an entropy stabilized single phase was first applied to metallic alloys [179], [180]. However, the concept can also be applied to oxide materials as a method of stabilizing a disordered cation sublattice [181], [182]. While the theoretical performance of these DRX cathode materials is promising, short-range ordering (SRO) induced by cycling at high current density has been shown to significantly degrade long-range Li transport [183], [184], [185], [186]. To combat this effect, prior works have employed a HE design scheme to create novel Li-excess DRX cathodes and demonstrated success in limiting SRO formation and improving reversible capacity [15], [18], [177].

The negative impacts of SRO formation on Li transport have motivated a rich body of work seeking to identify the local structure of SRO and the mechanisms by which it develops. Recent work by Li et al. [187] introduces an original approach of combining scanning transmission electron microscopy, electron diffraction, and Monte

Carlo simulation to derive a real space representation of the atomic arrangements in SRO which had previously been convoluted behind reciprocal space projections. The authors reveal that the local structure of SRO in a model $Li_{1.2}Ti_{0.4}Mn_{0.4}O_2$ DRX cathode can be described as a combination of three distinct cation clustering types: tetrahedron, octahedron, and cube. Furthermore, the authors state that the character of the identified SRO can be manipulated via anion doping or heat treatment which ultimately modifies the electrochemical properties of the cathode. In an earlier work by Jones et al. [17], the structure of SRO in a similar DRX cathode model ($Li_{1.25}Nb_{0.25}Mn_{0.5}O_2$) is characterized using powder diffraction techniques. In this work the authors do not identify individual types of cation clustering but rather a distinct crystal structure associated with SRO. Diffraction patterns of the cathode material which contains SRO are shown to closely fit a γ-$LiFeO_2$ structure.

Motivated by a surge in research on factors that limit the performance of DRX cathodes, many studies have been conducted which seek to apply the key findings and synthesize new DRX compositions which circumvent prior limitations. These synthesis strategies incorporate elements of HE design, fluorination, and acceleration by both ab-initio simulation and machine learning. Notably, Lun et al. [15] synthesize three distinct DRX models with an increasing number of TM components to evaluate the impact of configurational entropy on reversible capacity. As expected, the presence of SRO is diminished in the highest entropy composition and the capacity increases as a function of the number of TMs present. Pei et al. [177] use an alternative approach and synthesize a $Li_{1.46}Ni_{0.32}Mn_{1.2}O_{4-x}$ ($0 < x < 4$) DRX composition with the intention that initial delithiation drives a phase change resulting in the formation of a medium entropy

spinel-type structure with partial disorder. This methodology runs counter to the prevailing trend of maximizing entropy to limit SRO formation and instead seeks to produce a wholly different semi-ordered state that is itself conducive to long-range Li transport. The authors report that the predicted structural transformation does occur after initial delithiation, and that the resulting electrochemical performance is high with a discharge capacity of 314.1 mA h g^{-1} at a current density of 100 mA g^{-1}. In addition to these studies where the choice of composition is driven primarily by chemical intuition and prior results in literature, some authors are also turning to computational methods to determine optimal TM occupancy on the cation sublattice. Gao et al. [188] employ a DFT based approach to assess the influence of different TM dopants on relevant properties such as band gap, oxygen valence, and lattice stability. After screening 8 TMs the authors conclude that Nb is a promising candidate and a follow up experimental measurement of the predicted material results in improved electrochemical performance relative to undoped Li_2MnO_3. To further accelerate the selection of performant TMs for HE cathode compositions, Sturman et al. [19] deploy a random forest regression algorithm to predict ideal TMs based on features such as redox compatibility, procurement cost, and energy density. The authors identify $LiNi_{0.2}Mn_{0.2}Co_{0.2}Fe_{0.2}Ti_{0.2}O_2$ as their best performing cathode and report that the material is both low cost and has a stable capacity of 85 mAh g^{-1} when charged to a voltage of 4.4 V.

A review of the recent literature on DRX cathode design and development reveals that numerous permutations of design strategy and chemical composition can successfully produce cathode materials with desirable electrochemical properties. While

this is a positive development towards the goal of improving Li-ion battery performance; the challenge of screening the vast compositional search space to identify optimal cathode materials remains unresolved. Due to the flexibility of the DRX framework in incorporating many distinct TM types and the general compatibility between individual TMs, the task of identifying and validating all high-performance compositions is intractable from a purely experimental approach. Therefore, in this work we present a novel approach for high-throughput screening of DRX cathode candidates to accelerate the process of material discovery and ultimately advance the performance of Li-ion batteries. DFT and crystal graph neural network methods are employed in tandem to predict and validate the likelihood of SRO formation in DRX compositions spanning a wide range of constituent TMs. Specifically, three distinct models of SRO designed to be compatible with the limited length scale of ab-initio calculations are considered and evaluated in the context of experimentally observed SRO structures. Furthermore, the impact of entropy on the likelihood of SRO formation is determined from explicit calculation of configurational entropy on the cation sublattice. Lastly, a promising cathode candidate is identified and validated at the ab-initio level of theory with compelling results to motivate future experimental synthesis.

7.2 Computational Methodology

7.2.1 Density Functional Theory

All density functional theory (DFT) calculations in this work are performed using the Vienna Ab initio Simulation Package (VASP) [83], [84], [85]. Projector augmented plane wave (PAW) pseudopotentials [86] describe the interactions between core and valence electrons. The generalized gradient approximation (GGA) and Perdew-Burke-Ernzerhof (PBE) functional [23] are used to describe the exchange correlation energy.

GGA+U is employed to improve the performance when modeling localized *d* electrons, which is a known limitation in DFT [35]. The U values selected for Mn, Ti, and Zr are 3.9, 2.0, and 4.0 respectively. These values are adopted from prior DFT work which considered the same cations [189], [190], [191]. A plane-wave cutoff energy of 500 eV is used in all calculations following a convergence study over the range of 300 - 750 eV.

Each simulation cell is a 2 x 2 x 2 rocksalt supercell consisting of 64 atoms. A k-point convergence study found that a 5 x 5 x 5 Γ-point centered Monkhorst-Pack [88] mesh provides a reasonable balance between computational speed and precision for structures of this size. Magnetic moments are assigned only to the Mn atoms which are initialized to 5.0 μ_B each. This initial value is adopted from the work of Jain et al. [64]. The converged magnetic moment on each Mn atom varies between compositions and different configurations within the same composition. All structural relaxations employ a Gaussian smearing scheme with a smearing width of 0.05 eV. This setting is recommended for oxides in the VASP documentation. After each relaxation is completed, the total energy is extracted from a single-point calculation of the previously relaxed structure. This single-point calculation uses the tetrahedron method with Blöchl corrections as its smearing scheme to achieve the most accurate measurement of energy [89].

7.2.2 Crystal Graph Convolutional Neural Network

The crystal graph neural network implementation used in this work is the Crystal Hamiltonian Graph Neural Network (CHGNet) developed by Deng et al [63]. Tests of the pre-trained model distributed with the source code (v0.3.0) show excellent qualitative agreement with the DFT calculations in this work. Figure 7-1 illustrates the parity between CHGNet and DFT predictions for the total energy per atom of the DFT

relaxed $Li_{1.25}$ samples. Note that using CHGNet on pre-relaxed samples is intended as a benchmark exercise - the results presented in Chapters 7.3.2 and 7.3.3 use CHGNet to execute structural relaxations directly on idealized supercells. The $Li_{1.25}$ subset is selected because it is most relevant for the application domain. The magnitude of the predicted energies differs, but the line of best fit through the data has a slope very near to 1 indicating that the CHGNet and DFT predictions are almost equivalent when a linear offset is applied.

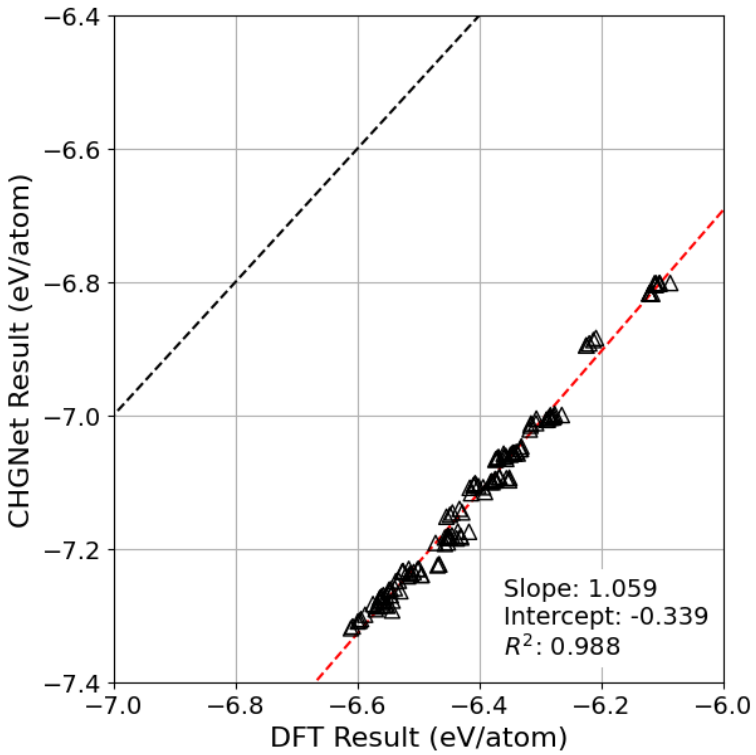

Figure 7-1. Parity plot comparing the performance of CHGNet predictions against DFT ground truth. The dashed black line represents perfect parity, and the red dashed line represents a linear fit to the data.

Alternative implementations were also tested: namely, the orbital graph convolutional neural network (OGCNN) by Karamad et al. [61], the atomistic line graph neural network (ALIGNN) by Choudhary and DeCost [192], and the original crystal graph convolutional neural network (CGCNN) by Xie and Grossman [59]. Ultimately,

CHGNet's ability to predict the force acting on each atom and thus relax idealized supercells paired with its vast training set that enables compositional search across all transition metals (TMs) makes it the most effective model for this work.

7.2.3 Structure Generation

Structures in this work vary in both composition and ordering type. Specifically, three distinct Li fractions are considered: $Li_{0.75}$, $Li_{1.0}$, and $Li_{1.25}$ with $Li_{1.25}$ being most relevant for industrial applications. On the non-Li cation sublattice, the TMs of interest are Mn, Ti, and Zr where Mn acts as the redox site and Ti and Zr function as charge compensators. This compositional space can be generalized with the chemical formula: $Li_XMn_Y(Ti,Zr)_ZO_2$ where Y + Z = 2 – X. Seven distinct compositions, spanning different cation types and stoichiometries, are evaluated for each Li fraction for a total of 21 compositions under investigation.

To approximate SRO in a way that is compatible with the limited length scale accessible to ab-initio calculations, Li atoms are localized to low index planes of type {100}, {110}, and {111}. The planes are arranged in an alternating fashion to keep the interplanar distance between pairs of ordered and disordered planes constant. The three ordering types are illustrated in Figure 7-2. In addition to samples with specific ordering, fully disordered special quasirandom structures (SQS) are also generated for each composition which serve as a baseline of no SRO to compare against. SQS is preferrable to generation with a simple random choice algorithm as it minimizes local correlation between pairs of atoms which is particularly important in periodic crystal systems [67].

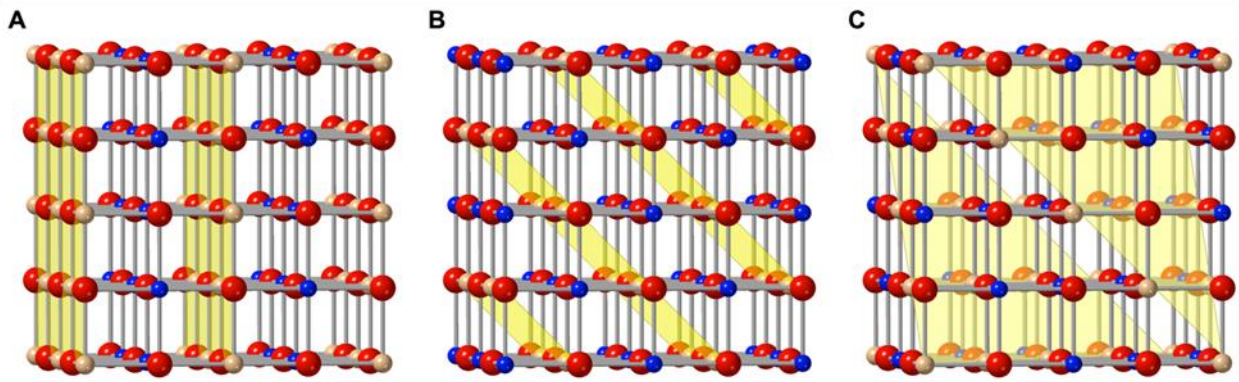

Figure 7-2. Ordering types illustrated on idealized $LiMnO_2$ rocksalt structures. The structures are ordered by creating Li layers on low index crystallographic planes {100} (A), {110} (B), and {111} (C). The ordered Li planes are highlighted in yellow. O is red, Mn is blue, and Li is beige.

The cumulative number of cations on the ordered planes in each system is always 16. This constraint is significant in relation to the Li fraction of the structure. For $Li_{0.75}$ compositions, this has the implication that 4 of the 16 cation sites will be occupied by a cation other than Li and for $Li_{1.25}$ samples, 4 Li cations will occupy disordered planes. Only in the $Li_{1.0}$ samples will Li atoms be perfectly separated from the other cation species. This is a consequence of limited system size. However, because the ordered planes always contain significantly more Li than disordered planes, this effect is not expected to bias either the $Li_{0.75}$ or $Li_{1.25}$ samples.

The primary structure generation tool used throughout this work is *sqsgenerator* developed by Gehringer et al. [66]. Systems with alternating planes of ordered Li and disordered cations are generated by leveraging the software's capability to operate on user-defined subsets of lattice sites rather than entire crystal structures. This ensures disordered planes are populated as if they were part of an SQS while ordered planes remain unmodified and contain appropriate amounts of Li. For each composition under investigation, 5 fully disordered configurations, 3 {100} ordered configurations, 3 {110} ordered configurations, and 3 {111} ordered configurations are generated for a total of

14 unique structures per composition. For $Li_{1.25}$ compositions the number is increased to 5 of each ordering type for a total of 20 unique structures per composition. This scheme balances limitations on computational resources with the goal of adequately sampling the configurational space of each composition.

The process of generating samples for prediction by CHGNet follows a similar procedure on a larger scale. One simplification is the elimination of $Li_{0.75}$ and $Li_{1.0}$ compositions to focus only on the more application relevant $Li_{1.25}$. Within this compositional space, all viable combinations of Mn, Ti and Zr are generated with the stipulation that the Mn content is $\geq Mn_{0.375}$. This restriction reflects the requirement in the application domain that enough Mn is present to exploit for redox reactions. For each viable composition, a limit of 10 samples per ordering type are generated. Note that a maximum limit is imposed but not always achieved because *sqsgenerator* may not always find 10 distinct configurations with optimal disorder. This results in 935 unique structures spanning 28 different compositions – a sample size 6.7x greater than the original $Li_{1.25}$ DFT dataset. It is important to consider that each of these structures are unrelaxed and as generated would have identical lattice parameters. However, because CHGNet is capable of predicting the force acting on each atom, it is possible to use the model to relax the generated structures directly.

7.3 Results

7.3.1 DFT Calculations

A central theme of discussion in this work is the tendency for a particular structure to exist as ordered or disordered. This property is not intrinsic to each structure, but rather is made evident through comparison. To quantify a structure's tendency to order from a thermodynamic perspective, one must compare the energy of

a structure with imposed order to that of a structure with imposed disorder. Repeating this process for a range of samples will result in one of three possibilities: 1) the energy of the ordered sample is more positive than the energy of the disordered sample, 2) the energy of the ordered sample is more negative than the energy of the disordered sample, or 3) the energy of the ordered sample is within the range of energy of the disordered configurations. Each of these scenarios can be seen in Figure 7-3, which illustrates the DFT final energy per atom for $Li_{1.25}Mn_{0.5625}Zr_{0.1875}O_2$ specifically.

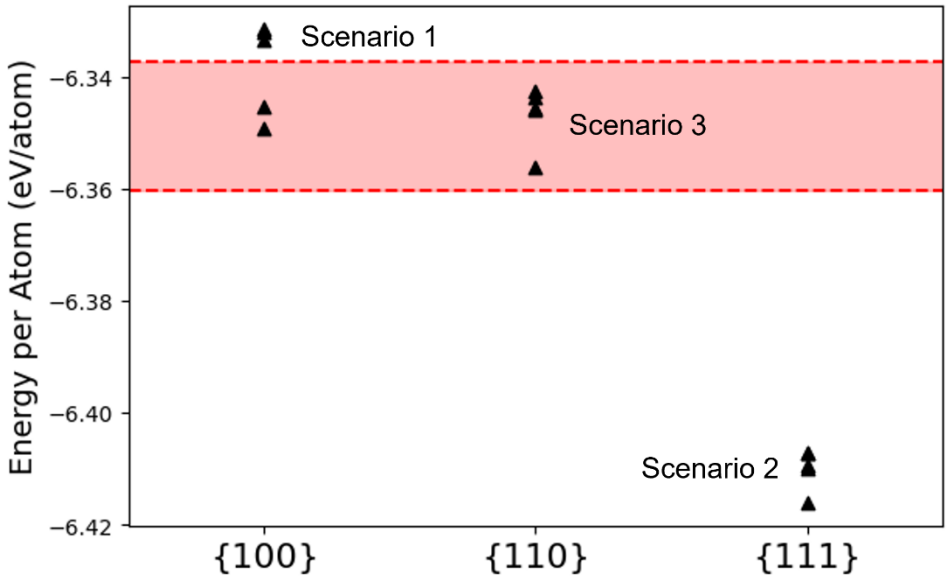

Figure 7-3. DFT final energy per atom for the $Li_{1.25}Mn_{0.5625}Zr_{0.1875}O_2$ composition. The red band spanning the width of the figure represents the energy range of the fully disordered configurations.

In scenarios 1 and 3, the ordered sample should be considered to “favor disorder” because at least one comparable disordered sample is lower in energy and thermodynamics dictates that the ordered sample will eventually relax into that lower energy state given sufficient time to overcome any kinetic barriers. In scenario 2, the ordered sample should be considered to “favor order” because it is lower in energy than all comparable disordered samples and thus cannot reduce its energy by transitioning to

a disordered state. It is important to note that this method is only valid when comparing structures with the same composition. This is the criteria that is used to determine whether a particular sample favors order or disorder throughout the remainder of this work.

A fundamental consideration in understanding how SRO develops in HEOs is the physical form that it takes. By investigating three unique approximations of SRO for each composition in the dataset, DFT calculations can elucidate which type is most likely to form. In Figure 7-4, the percentage of samples that favor or disfavor order are presented for each ordering type broken down by Li fraction. Red bars represent the samples that are strictly lower in energy than the minimum disordered reference, grey bars are within the range of disordered samples, and blue bars are strictly higher in energy than the maximum disordered reference.

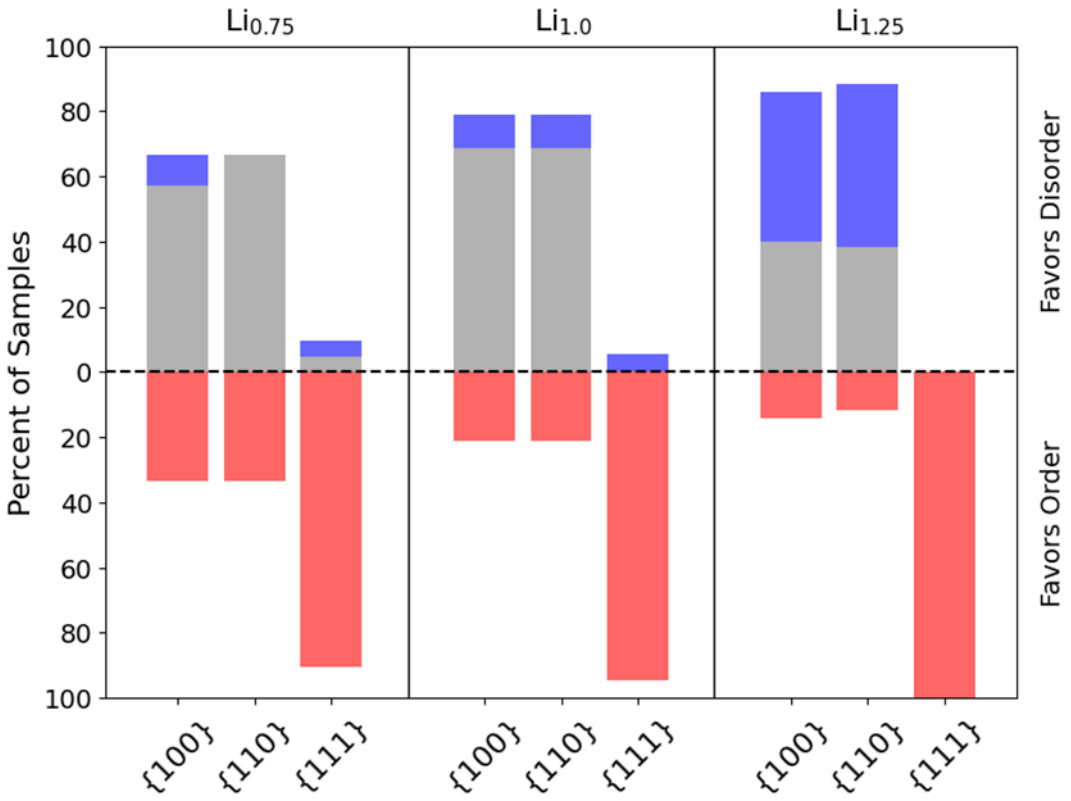

Figure 7-4. Effect of ordering type on ordering favorability. Blue bars represent the percentage of ordered samples in each group that are strictly higher in energy than the highest disordered sample of the same composition, grey bars represent the percentage of ordered samples that are within the range of the disordered samples of the same composition, and red bars represent the percentage of ordered samples that are strictly lower in energy than the lowest disordered sample of the same composition.

From inspection of Figure 7-4, it is evident that {111} type ordering dominates across all Li fractions. In fact, 100% of {111} ordered $Li_{1.25}$ samples are favorable relative to disorder. In addition to this clear trend, a positive correlation between the Li fraction and share of {100} and {110} ordered samples favoring disorder can be observed. This dichotomy between the increasing preference for disorder in {100} and {110} ordered samples as a function of Li content and the clear dominance of {111} ordering favorability in $Li_{1.25}$ suggests that there is a qualitative difference in the chemical environment of {111} ordered samples. Referring back to Figure 7-2c, the

crystallography of the ordered planes confirms this. In {111} ordered samples, the Li planes are purely cationic. Conversely, both {100} and {110} ordered planes are interspersed with oxygen atoms creating a different local environment for the cations. This tendency to favor order along strictly cationic {111} planes is also present in crystal structures that have been experimentally characterized as local representations of SRO. In Figure 7-5, both spinel and γ-$LiFeO_2$ unit cells are illustrated to highlight cation connectivity along {111} planes.

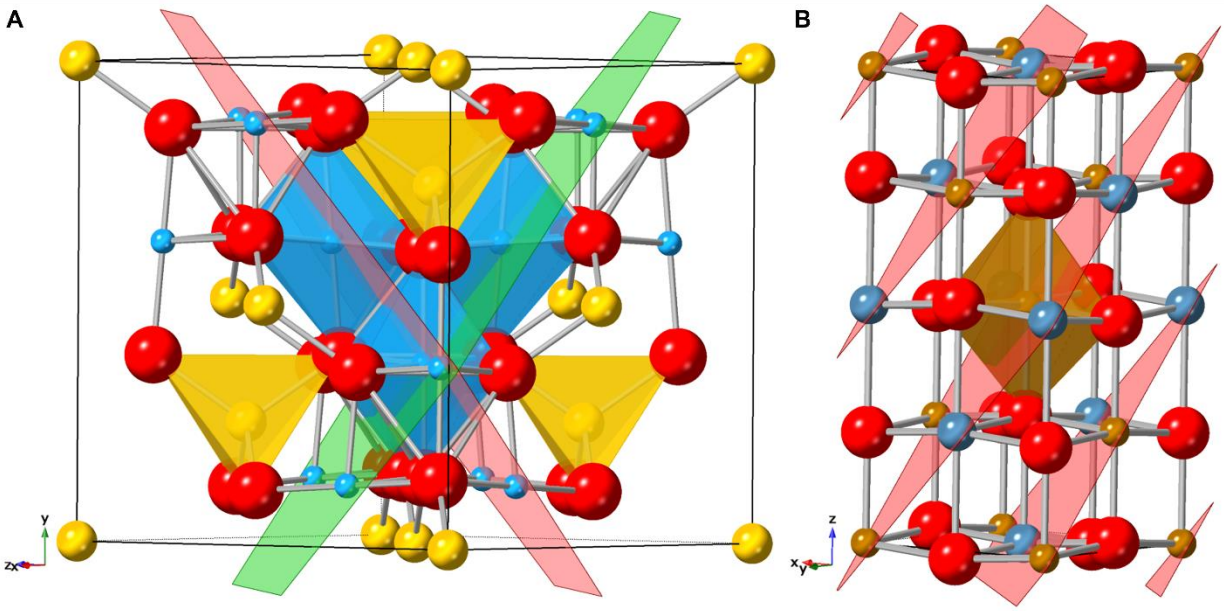

Figure 7-5. Diagram of cation connectivity in a generic AB_2O_4 spinel (A) and γ-$LiFeO_2$ (B).

The AB_2O_4 spinel structure in Figure 7-5a is reported to be the semi-ordered end state of a phase transformation from DRX $Li_{1.46}Ni_{0.32}Mn_{1.2}O_{4-x}$ ($0 < x < 4$) induced by an initial delithiation of the structure [177]. The red and green planes denote members of {111} and $\{1\bar{1}1\}$ respectively. Observe that these planes are parallel with the octahedrally coordinated B-sites and never intersect an anion site much like the structural arrangement depicted in Figure 7-2c. Similarly, Figure 7-5b illustrates cation connectivity in the γ-$LiFeO_2$ unit cell which has been identified as the localized SRO

structure associated with DRX $Li_{1.25}Nb_{0.25}Mn_{0.5}O_2$ [17]. Again, the highlighted planes cross only the cation sites. It should be noted that the highlighted planes in Figure 7-5b are members of {112} rather than {111} so the transferability back to the Figure 7-2c arrangement is not perfect but rather a close analog. The fact that the {111} ordering type – a simplified model of SRO that is strongly predicted to be the dominant ordering type in this work - shares key structural features with experimentally validated expressions of SRO corroborates its validity as an approximation of SRO in small simulation cells.

A major factor driving interest in HEOs as a material system for energy storage is the purported phase stabilization induced by the configurational entropy associated with a higher number of cation components. To address the impact of this entropic effect, Figure 7-6 reports the ordering favorability of each sample broken down by the number of non-Li cation components.

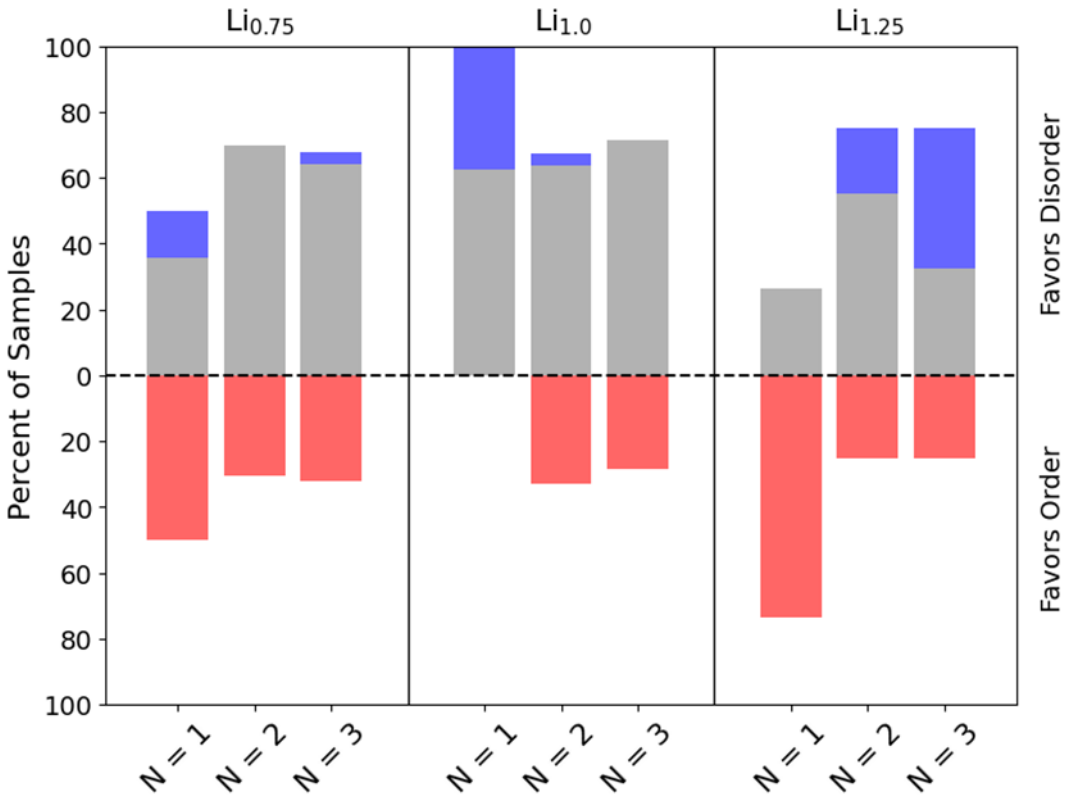

Figure 7-6. Effect of the number of transition metals (Mn, Ti, Zr) on ordering favorability. Blue bars represent the percentage of ordered samples in each group that are strictly higher in energy than the highest disordered sample of the same composition, grey bars represent the percentage of ordered samples that are within the range of the disordered samples of the same composition, and red bars represent the percentage of ordered samples that are strictly lower in energy than the lowest disordered sample of the same composition.

Perhaps most evident in Figure 7-6 is the difference in the behavior of N=1 samples for the $Li_{1.0}$ compositions as compared to both $Li_{0.75}$ and $Li_{1.25}$. This can be partly explained by the unique structural characteristic of the $LiMnO_2$ composition in relation to the ordering schemes employed in this work. Because the total number of available cation sites is 32 and the Li atoms are fixed to occupy half of them on the ordered planes, that leaves the other half as pure Mn. This results in just 1 possible configuration for each ordering type of the $LiMnO_2$ composition rather than a range of configurations available to all other compositions. In contrast, N=1 samples of the $Li_{0.75}$

and $Li_{1.25}$ compositions tend to favor order most strongly. Furthermore, the N=2 and N=3 samples are most likely to favor disorder especially for $Li_{1.25}$ compositions. However, there is only a minor difference in the behavior of N=3 over N=2 in $Li_{1.25}$ with N=3 having a higher percentage of samples strictly favoring disorder, but both achieving the same tendency to disorder when samples competitive with disorder are included. Taken together, this provides some support for the idea of entropic stabilization though the effect is largely outweighed by the dominance of {111} type ordering shown in Figure 7-4.

In addition to simply counting the number of unique TMs, it is possible to assess the impact of configurational entropy more directly by explicitly calculating it for each sample. Entropy is derived using Equations 7-1 and 7-2 as follows:

$$\Delta S = -R \sum_{i=0}^{n} x_i \ln x_i \tag{7-1}$$

$$x_i = \frac{n_i}{N_c} \tag{7-2}$$

Where R is the ideal gas constant and i indexes over the n total cation types. The atom fraction x_i is the quotient of the number of "active" cations of type i and the total number of cations in the system N_c. Active cations are defined as those which are not constrained to an ordered Li-plane.

To visualize this representation of entropy in relation to ordering favorability, the entropy of each sample is calculated and used to construct two distinct distributions: one from the samples which favor order and one from the samples which favor disorder. Kernel density estimation (KDE) is used to evaluate the probability density function (PDF) of each data set. To extract the magnitude of the preference for either ordering

condition, the PDFs are transformed by calculating their contribution to the sum of the two distributions as a percentage. This scheme is presented in Figure 7-7 and illustrates the percentage of samples favoring each ordering condition as a function of the explicitly calculated configurational entropy.

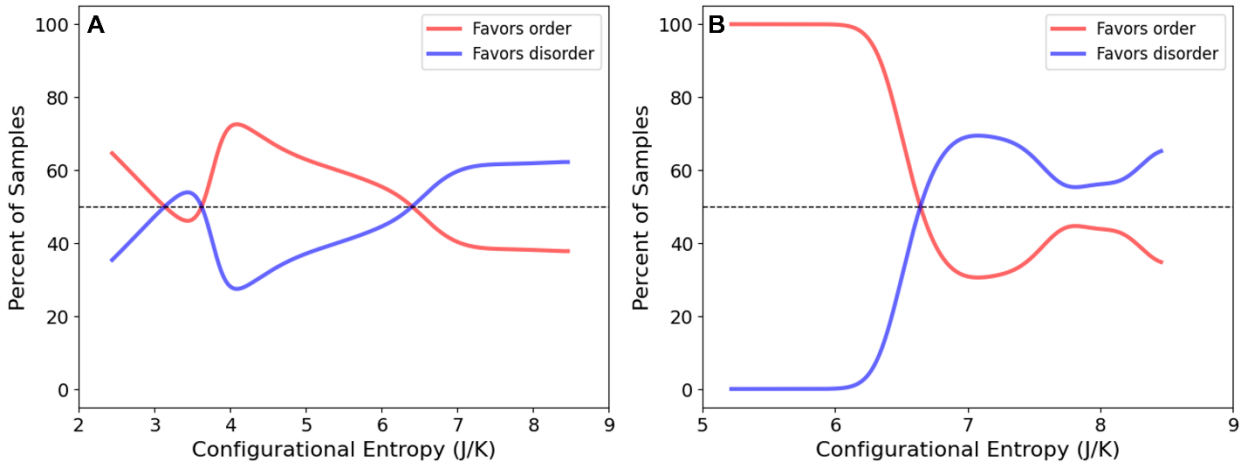

Figure 7-7. Distribution of configurational entropy for samples in the DFT relaxed dataset. The red curve represents the percentage of samples favoring order and the blue curve represents the percent of samples favoring disorder. All Li fractions (A), only $Li_{1.25}$ samples (B).

The two subplots of Figure 7-7 represent subsets of samples in the DFT relaxed dataset. Figure 7-7a contains data for all samples across all Li fractions while Figure 7-7b is limited to just the $Li_{1.25}$ samples. In Figure 7-7a, there is a clear offset between the two distributions with order tending to dominate in the low-entropy range and disorder tending to dominate in the high entropy range. The divergence between the two peaks at an entropy of 4.1 J/K where the split is approximately 75/25 in favor of order. At the highest end of the scale, disorder is favored at 65%. In Figure 7-7b the same general trends can be observed. At the low end of the scale, order is favored at 100% until 6.2 J/K where the distributions begin trending towards the center. The highest peak favoring disorder is 70% at an entropy of 7.1 J/K. One might also observe that the range of entropy between these two subsets is not equivalent. This is due to the fact that in the

$Li_{1.0}$ samples (only present in Figure 7-7a) the positions of all Li atoms are fixed and thus cannot contribute to the entropy as active cations. The same is true of the $Li_{0.75}$ samples, but in this case there are additional TM cations on the ordered Li planes which are counted as active. In the $Li_{1.25}$ samples, excess Li on non-ordered planes is counted as active and thus contributes to entropy.

7.3.2 CHGNet Predictions

The primary goal of using an accelerated energy prediction tool like CHGNet is to enable a thorough scan over a wider compositional space than is reasonably accessible to ab-initio methods. By exhaustively scanning the $Li_XMn_Y(Ti,Zr)_ZO_2$ search space, particular compositions that especially favor either order or disorder can be identified and further investigated. In Figure 7-8, ternary phase diagrams illustrating the percentage of samples favoring disorder at each composition (Figures 7-8b and 7-8c) are compared to the limited set of compositions investigated using DFT (Figure 7-8a). The colormap is scaled such that regions exhibiting high preference for disorder are shown in red and those with low preference are shown in blue. Regions where the map is blank indicate that 0% of samples favor disorder. Note that these maps (and all CHGNet results in this work) are limited to $Li_{1.25}$ compositions because of their relevance as potential cathode compositions.

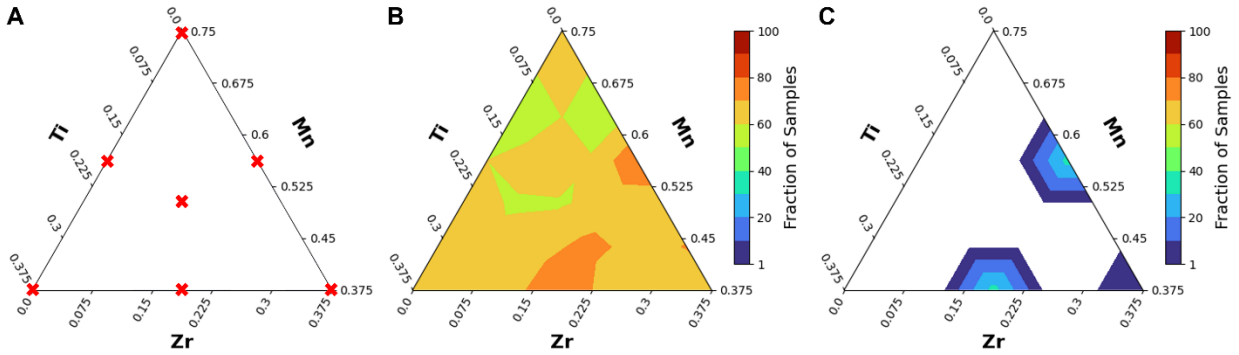

Figure 7-8. Ternary phase diagrams illustrating: the compositions investigated with DFT (A), the percentage of all ordered samples that favor disorder (B), and the percentage of {111} ordered samples that favor disorder (C).

Figure 7-8b, which represents all {100}, {110}, and {111} ordered samples, depicts that throughout the entire Mn-Ti-Zr compositional space disorder is favored in 50-80% of samples depending on the specific composition. Most compositions in the space tend to have 60-70% of their samples favor disorder. This reflects the finding from the DFT calculations that {100} and {110} ordered samples tend to favor disorder while {111} always favors order. Therefore, it is expected that $\frac{2}{3}$ or 67% of samples would tend to favor disorder. To further support this interpretation, Figure 7-8c represents the percentage of only the {111} ordered samples that favor disorder. If CHGNet predictions were to accurately reflect the DFT findings it should be expected that none of these samples would favor disorder. Indeed, only 2 compositions out of the 28 total are predicted to exhibit any percentage of their samples favoring disorder. Furthermore, within these two compositions, the maximum predicted percentage is just 30-40%. Because these two problematic compositions happen to already be represented within the DFT relaxed dataset it is straightforward to confirm that they should not in fact exhibit any preference for disorder. To address this, Figure 7-9 contrasts the results of the DFT calculations with CHGNet predictions for these two

compositions. Note that in this comparison, CHGNet is operating on structures which have already been relaxed by DFT whereas those which are a part of Figure 7-8 are relaxed strictly with CHGNet. Comparing the two under these specific conditions reveals a sensitivity to lattice site distortions that is crucial in understanding the formation of SRO.

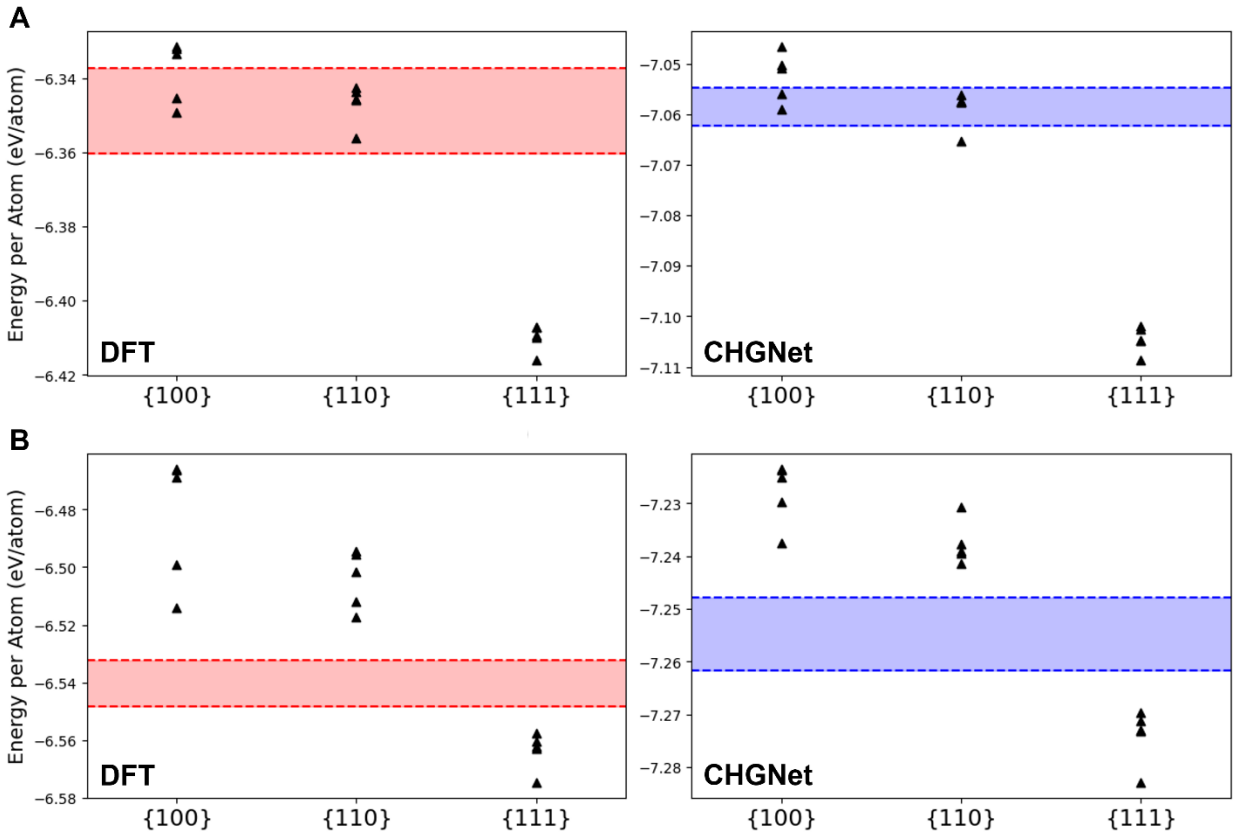

Figure 7-9. Direct comparison between DFT calculation results and CHGNet predictions on DFT relaxed samples. Each subplot refers to a unique composition: $Li_{1.25}Mn_{0.5625}Zr_{0.1875}O_2$ (A) $Li_{1.25}Mn_{0.375}Ti_{0.1875}Zr_{0.1875}$ (B). DFT results are shown on the left in red and CHGNet predictions are shown on the right in blue.

Referring to Figure 7-9, DFT clearly predicts all {111} ordered samples to favor order. Interestingly, CHGNet predicts the same despite the results of Figure 7-8 which would suggest that these two compositions should have 30-40% of their {111} samples predicted to favor disorder. The explanation for this discrepancy is the fact that the

results presented in Figure 7-8 are for structures which employ CHGNet to do all structural relaxation whereas those in Figure 7-9 rely on DFT. Therefore, it is evident that the classification of a sample as favoring order or disorder may be sensitive to particular lattice site distortions that are only captured at the ab-initio level of theory. This finding also has the implication that CHGNet's prediction of per-atom forces is less accurate than its prediction of total energy. Despite this specific failure of the model to reproduce DFT results for 2 of the 28 compositions, the overall performance of CHGNet in classifying samples as favoring order or disorder is excellent. Furthermore, one should note the resolution required of the model to accurately make this type of classification. In Figures 7-9a and 7-9b the difference in energy between the minimum disordered reference state and the maximum {111} ordered sample is just 47 meV/atom and 10 meV/atom respectively. This level of accuracy approaches that of DFT relative to experiment and highlights how the small effect size of SRO formation makes it a challenge to predict using even the best available methods [109].

Having established that CHGNet is in close qualitative agreement with DFT regarding the prediction of ordering favorability throughout the Mn-Ti-Zr compositional space, it is instructive to use its predictions to revisit the impact of configurational entropy. Similar to the results presented in Figure 7-7b, Figure 7-10 also plots the percentage of samples favoring either ordering condition as a function of the configurational entropy derived from Equations 7-1 and 7-2. However, the samples used to generate Figure 7-10 span 28 compositions in the Mn-Ti-Zr compositional space rather than just the 7 unique compositions investigated with DFT. Furthermore, the

energies used to classify each sample as either favoring order or disorder are predicted by CHGNet.

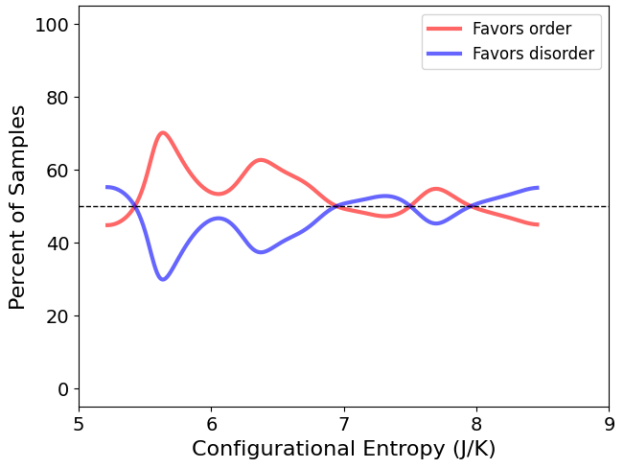

Figure 7-10. Distribution of configurational entropy for all samples in the Mn-Ti-Zr compositional space with energy predictions and structural relaxations handled by CHGNet.

In comparing Figures 7-7b and 7-10, it appears that the inclusion of additional compositions in Figure 7-10 results in a more muted expression of the same trends found in Figure 7-7b. A preference to form order for samples on the lower half of the entropy scale remains with the exception of a small crossover at the minimum bound. Between 6.9 J/K and 8.0 J/K the two distributions are highly competitive with preference for disorder ultimately dominating 58% to 42% at the upper bound of the entropy scale. While it is evident that including additional compositions diminishes the perceived influence of configurational entropy on stabilizing disorder, one trend which remains strong is the tendency for samples of lower entropy (below 6.9 J/K) to favor the formation of order. Therefore, while high entropy may not be sufficient as a design variable to control SRO formation, it is reasonable to conclude that low entropy configurations should be avoided as they are consistently associated with a preference for order.

7.3.3 Expanded Compositional Search

Building on the findings presented in Chapters 7.3.1 and 7.3.2 which establish a foundation for understanding how ordering type and configurational entropy influence the formation of SRO in the Mn-Ti-Zr system, it follows that expanding the compositional search space could help to identify specific compositions as desirable synthesis candidates for experimental testing. Recall that DFT and CHGNet both predict a strong preference for {111} type ordering throughout the Mn-Ti-Zr system. Therefore, in an effort to identify compositions for which SRO is thermodynamically unfavorable, it is necessary to expand the search space to consider compositions which include alternative TMs and assess their tendency to favor disorder relative to {111} type ordering.

The methodology used to generate this broader dataset is essentially the same as is described in Chapter 7.2.3. However, each composition contains a pair of the following TMs: Ti, V, Cr, Fe, Co, Ni, Zr, Nb, and Mo. The constraint specifying the lower bound of Mn content to be $\geq Mn_{0.375}$ remains unchanged which leaves each composition with a total of 3 TM types. Excluding the Ti-Zr pair which has already been investigated in Chapter 7.3.2, this expanded dataset includes 35 unique TM pairs. To save computational resources and focus on the most relevant phenomena, structure generation is limited to full disorder and {111} ordering types. These constraints result in a dataset of 9908 distinct samples across 525 unique compositions.

CHGNet is employed to execute both structural relaxation and energy prediction of each sample from which determinations of ordering favorability are made. Of the 525 unique compositions just 152 are predicted to exhibit any degree of favorability for disorder relative to the {111} ordering type. These compositions are plotted in Figure 7-

11. It can be seen that the $Li_{1.25}Mn_{0.5625}Zr_{0.1875}O_2$ composition, which proved to be problematic for CHGNet in Chapter 7.3.2, is on the lower end of the curve in terms of the percentage of samples predicted to actually favor full disorder. This enhances confidence in the methodology as a screening tool because it shows that the model identifies a significant number of compositions that are more likely to favor disorder than the composition for which it failed to do so. In fact, 12 compositions are predicted to exhibit a 100% tendency to favor disorder relative to {111} ordering.

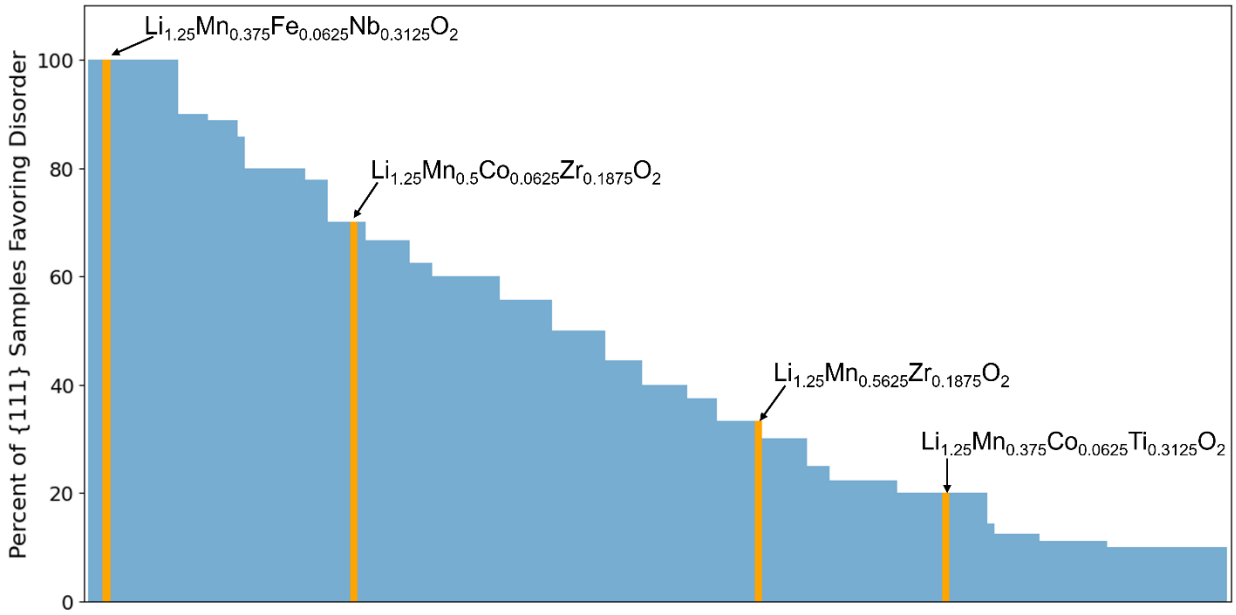

Figure 7-11. Each of the 152 compositions which CHGNet predicts to exhibit some degree of disorder relative to {111} type ordering. Specific compositions of interest are highlighted in orange.

To further downselect this group of novel compositions, a filter is applied to retain only those which are predicted to exhibit ≥ 50% of samples favoring disorder. This results in 69 compositions for which there is likely some preference for disorder. To characterize this set of compositions, Figure 7-12 illustrates the frequency with which both individual TMs and pairs of TMs are found in the compositions that make up the set.

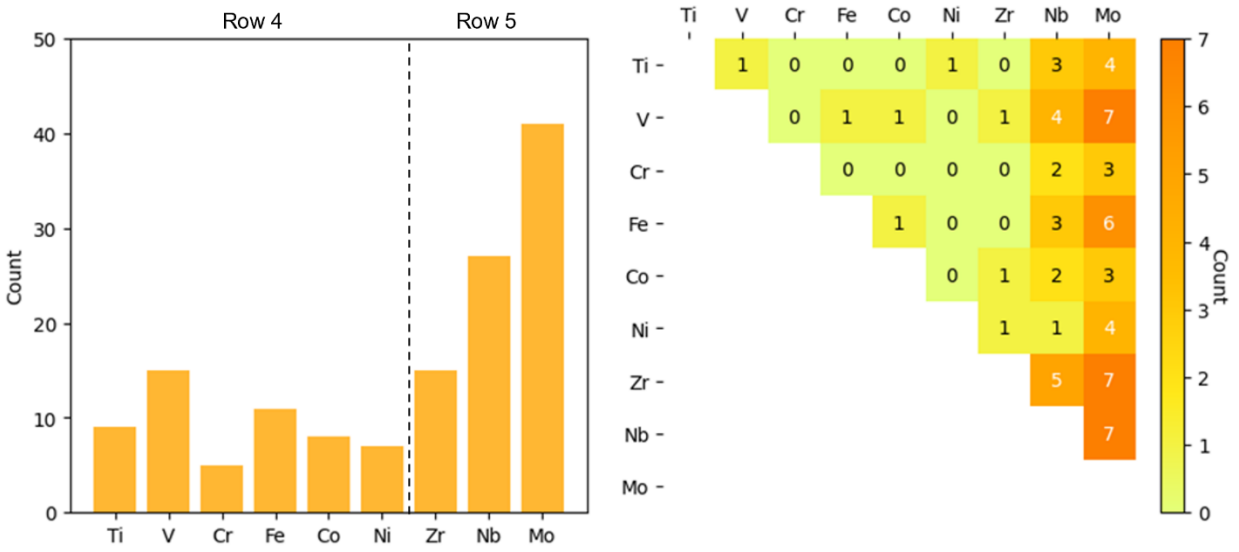

Figure 7-12. Frequency of both individual TMs (left) and pairs of TMs (right) to be found in the compositions which are predicted to have ≥ 50% of their samples favor disorder relative to {111} ordering.

Inspection of the individual TM histogram in Figure 7-12 reveals that Mo is the most frequently found TM in the set. Additionally, it appears that there is some correlation between an element's Z value and the frequency with which it is found because the highest Z elements; Zr, Nb, and Mo are arranged in the same order as their frequencies. However, this trend is reversed for row 4 TMs in which there is a downward trend in frequency from V to Ni. Observation of the pair frequency heatmap reinforces Mo's position as the most common TM in the set with Mo-V, Mo-Zr, and Mo-Nb being the most frequent pairs to appear.

The identification of 12 novel compositions which are predicted to favor disorder relative to {111} type ordering in 100% of samples (Figure 7-11) is a satisfying result which impels further investigation. To close the loop in the cycle of materials discovery, DFT validation of these compositions is conducted to confirm that the {111} ordered samples do in fact favor disorder. As of now, this validation has been completed for 3 of the 12 compositions. Out of the 3 completed compositions, 1 has proven to reproduce

the predicted results and exhibit a 100% tendency to disorder. This composition is the $Li_{1.25}Mn_{0.375}Fe_{0.0625}Nb_{0.3125}O_2$ formulation highlighted in Figure 7-11. The DFT calculated final energy per atom for each sample of this composition is presented in Figure 7-13. Each of the {111} ordered samples have an energy greater than or equal to that of the lowest energy disordered reference state indicating that they are all competitive with disorder and thus will tend to relax into a disordered state given sufficient time to overcome any kinetic barriers. This result affirms the validity of the CHGNet screening process and provides a promising direction for future experimental synthesis and characterization.

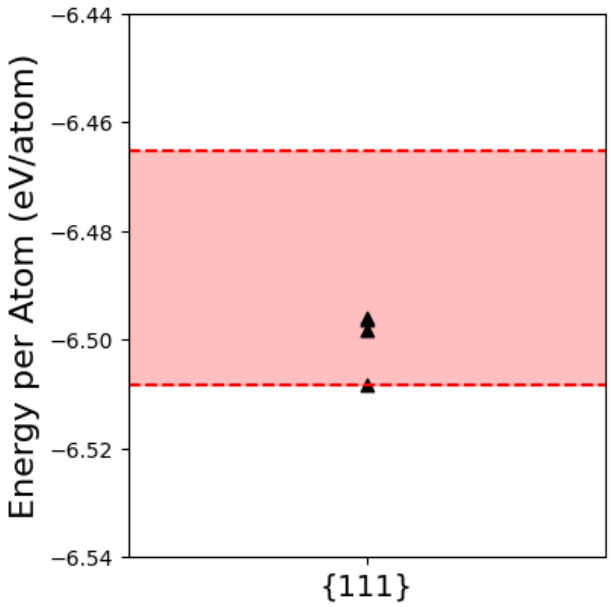

Figure 7-13. DFT results for the $Li_{1.25}Mn_{0.375}Fe_{0.0625}Nb_{0.3125}O_2$ composition which is predicted by CHGNet to favor disorder relative to {111} ordering in 100% of samples.

7.4 Discussion and Conclusions

The investigation of SRO and its intersection with the ordering type, entropy, and composition of DRX cathode candidates presented in this work advances our understanding of the complex design criteria surrounding this promising material

system. DFT calculations confirm that the {111} ordering type is thermodynamically favorable for all compositions in the Mn-Ti-Zr system. Experimentally determined local structures of SRO in DRX materials share similar cation connectivity with the {111} ordering type thus affirming the simplified representation used in this work as a valid approximation [17], [177]. Both DFT and CHGNet results indicate that lower entropy configurations are more likely to favor ordering which is consistent with findings in the literature which report that increasing the number of TMs on the cation sublattice results in a reduction of SRO [15]. In this study, however, the consideration of entropy goes beyond using the number of transition metals as a proxy and advances the understanding by explicitly calculating the configurational entropy of the cation sublattice to include the effect of varying the concentration of each TM for systems with the same number of TM components. Furthermore, we show that the correlation between low entropy and SRO formation is stronger than the correlation between HE and full disorder indicating that HE alone is not sufficient to resolve SRO formation, but low entropy should certainly be avoided. This work also introduces a high-throughput method to predict SRO formation in compositions containing arbitrary TMs. To our knowledge, this screening procedure has never before been applied to the problem of identifying SRO formation in DRX materials. Notably, through the implementation of this framework, we identify a number of compositions which are highly likely to thermodynamically favor full disorder and validate one such composition with DFT. Should this result be experimentally confirmed, it represents a great advancement in cathode performance by eliminating the problem of SRO without any requirement to modify the synthesis procedure or add any post-processing steps.

In conclusion, this study introduces a novel and highly efficient screening procedure to identify SRO formation in compositionally diverse DRX materials. We find that a compact approximation of the local structure of SRO produces results consistent with experiment. HE stabilization of disorder is investigated and revealed to be a necessary but insufficient factor in controlling SRO formation. Furthermore, we identify 12 new DRX compositions which are highly likely to exhibit thermodynamically stable disorder on the cation sublattice. Of these new compositions, one has been confirmed via ab-initio calculation to favor full disorder. This finding represents a promising advancement in the capability of DRX cathode materials which is much needed to improve Li-ion battery performance.

CHAPTER 8
SUMMARY AND FUTURE WORK

In this dissertation, a wide range of materials systems have been investigated with multiple simulation methodologies to address crucial research questions in the domains of high temperature corrosion, HLW disposal, and novel battery development. First, the mobility of point defects in the mediating $MnCr_2O_4$ layer of an oxide film which grows atop austenitic steel alloys are investigated using DFT in order to develop an atomistic description of the oxide growth mechanism. This analysis is extended to Cr_2O_3, another component of the oxide film, and a mechanism for evolution of the film is proposed based on the predicted migration barrier heights. Then, the interactions between an ionic solution representative of the groundwater present in a geological waste repository and various edge terminated clay models are characterized by MD simulation. The clay interlayer environment is then further investigated with MD to determine the precise arrangement of alkylammonium cations that are shown to enhance radionuclide sequestration. Lastly, a multimodal study of Li-HEO cathode materials employing both ab-initio and cutting-edge CHGNet models predicts new regions of compositional space that are likely to form stable disordered structures and enhance cycling performance.

In Chapter 3, the formation energy of vacancy, interstitial, substitution, and antisite defects is evaluated with DFT to assess the defect energetics in $MnCr_2O_4$. Each defect type is also considered as part of a migration pathway to understand the defect migration kinetics contributing to oxide film growth. The findings indicate that Mn vacancies are the most readily formed and migrate with a low migration barrier height of just 0.45 eV. The chemical complexity and unique structural vacancies inherent to the

spinel system also enable antisite and substitution type defects to contribute to cation migration. In fact, by first forming a Cr_{Mn} substitution defect, Cr is able to reduce its vacancy mediated migration barrier height from 2.41 eV to just 0.85 eV – significantly increasing its mobility along the cation sublattice. Additionally, oxygen was found to migrate most favorably via interstitialcy type mechanism with a barrier height of 1.86 eV. These findings highlight the rapid mobility of cations through the spinel phase suggesting a preference for cations to move outwards towards an oxidizing surface rather than for oxygen to diffuse down to the bulk alloy surface.

In Chapter 4, a similar analysis to $MnCr_2O_4$ in Chapter 3 is conducted for another component of the oxide film, Cr_2O_3. Vacancy, interstitial, and Mn_{Cr} substitution defects are evaluated for favorability with consideration for charge state and environmental conditions. The mobility of Cr and Mn via 4 unique elementary migration pathways is considered to identify the most efficient route for long-range diffusion. Mn as a Mn_{Cr} substitution defect is consistently predicted to have a lower barrier height than the native Cr. Furthermore, including the preferred Cr vacancy charge state results in further barrier height reduction for both Mn and Cr. By combining these findings with our prior work on $MnCr_2O_4$ we present a set of possible mechanisms driving the change in relative layer thickness after total oxide thickness has stabilized. Based on the barrier heights from this work, $MnCr_2O_4$ is predicted to grow at the alloy interface and Cr_2O_3 is predicted to grow at the $MnCr_2O_4$ interface.

In Chapter 5, the distribution of aqueous ions in the presence of phyllosilicate edge models with unique Mg_{Al}^{-} substitution defect distributions are analyzed with MD simulation to identify likely radionuclide adsorption sites and optimal substitution

patterns. Significant clustering of both cations and anions is observed around terminated edge structures even for the charge neutral PRL system. In MMT configurations with highly localized charge density due to the proximity of Mg_{Al}^{-} substitution sites, dense clusters of cations were observed to form in the interlayer adjacent to such sites. Furthermore, a secondary more diffuse layer of anions surrounds these clusters suggesting that functionalization of the net negative MMT structure can induce anion sequestration in the interlayer. Additionally, MMT configuration with low localized charge density due to an even distribution of substitution sites behave much like the charge neutral PRL system and do not offer significantly increased residence times of Na^{+} or Cl^{-} ions within the interlayers.

In Chapter 6, MD simulation is again used to characterize a clay interlayer environment this time consisting of a range of linear and quaternary alkylammonium cations which have been shown to improve radionuclide sequestration performance. MD simulation with CLAYFF and GAFF2 potentials showed good agreement with experimentally measured interlayer spacing results supporting the methodology as an effective computational tool for characterization. The interlayer regions tended to increase in density with increasing alkylammonium concentration despite also increasing the interlayer spacing. This suggests that the orientation of alkylammoniums tends to become more close packed as additional molecules are added instead of forcing a delamination of the clay sheet. Orientation angle measurements of carbon chains relative to the basal plane of the clay sheet indicated that alkylammonium molecules tend to prefer to lay parallel to the clay surface in flay outstretched configuration at low concentrations. As concentration is increased, the alkylammoniums

deviate from their parallel configuration and begin to tilt some or all of their long carbon chains to accommodate neighboring molecules. Distributions of central N positions suggest that the N side always tends to favor a position closer to the basal plane than the center of the interlayer. Furthermore, depending on size, alkylammonium molecules tend to favor monolayer configurations at low concentration and gradually switch to distinct bilayer and ultimately pseudo-trilayer at the highest concentrations. This evolution of layering and orientation is consistent with experimental measurements.

In Chapter 7, a high-throughput scan of Li-HEO compositions is conducted with DFT to validate a CHGNet model capable of efficiently searching the entire compositional space for compositions which are likely to favor full structural disorder. DFT calculations show that compositions of all Li fractions tend to favor {111} type ordering. The influence of compositional entropy is less clear although in $Li_{1.25}$ samples the N=2 and N=3 samples tend to favor disorder with the highest likelihood which gives some support to the theory that compositional entropy is stabilizing disorder. Using CHGNet to scan a broader compositional range proved to be an effective way to identify compositions that are likely to favor disorder. The model identified 12 novel compositions which are strongly predicted to favor disorder over {111} type ordering. A follow up DFT calculation of one of the 12 affirmed that disorder is in fact favored. This exciting finding motivates further screening and DFT validation with the ultimate goal of confirmation via experimental synthesis and cycle testing.

While the work described in this dissertation provides a number of valuable and actionable conclusions, it also reveals opportunities for continued research. The discussion of high temperature corrosion presented in Chapters 3 and 4 offer a

compelling starting point for the construction of a comprehensive mechanistic model of corrosion in 21-2N alloy, however, further simulation work which includes the contribution of phonons to the formation and migration energy of each defect species could be incorporated to better account for the environmental conditions in which the physical phenomenon actually occurs. Additionally, as was specifically highlighted in Chapter 4, the migration of oxygen through the outermost Mn_3O_4 oxide layer has yet to be characterized in the literature. Inclusion of this migration energy would serve to improve the fidelity of any hierarchical model attempting to predict the evolution of oxide formation at the onset and in later stages. While significant advancements are still possible through simulation alone, this project would benefit from further experimental characterization as well. Most relevant to this work, a prolonged exposure of the oxide film on 21-2N could be conducted out to 3000 hours or longer to determine how the relative layer thickness continues to evolve once total thickness has stabilized. Such an experiment would help to validate the simulation-based mechanism predictions and address the long-term stability of the outer Mn_3O_4 layer which appears to be shrinking in relation to the remaining Cr_2O_3 and $MnCr_2O_4$ layers.

The work on functionalized clay buffer materials presented in Chapters 5 and 6 would also benefit from further investigation. Perhaps most interesting from a simulation perspective would be the incorporation of complex pertechnetate and iodate ions into the alkylammonium saturated interlayers presented in Chapter 6. Such a simulation was excluded from this work due to the lack of a high-quality empirical potential for the ions. In future study though, it would be valuable to identify how the ions tend to orient themselves in the interlayer and also measure their diffusivity within the interlayer at

different alkylammonium concentrations. Experiments could also be conducted in tandem which measure the concentration of alkylammonium required (across different chain lengths and branching structure) to achieve sufficient radionuclide sequestration in order to optimize the synthesis process and reduce the required inputs as the process is scaled up.

Advancements to Li-ion battery performance presented in Chapter 7 offer the broadest range of continued work. For work that is strictly computational, there remains a vast unsearched compositional space for TMs beyond Mo which was the limit in this study. Furthermore, only pairs of charge compensating TMs were considered. To fully embrace the HE design philosophy, three or more TM components could be included to explore possible improvements in disorder favorability. Most applicable to the findings of Chapter 7, an experimental synthesis and charge cycling test of the ab-initio validated $Li_{1.25}Mn_{0.375}Fe_{0.0625}Nb_{0.3125}O_2$ composition would close the materials discovery loop and affirm the proposed screening methodology. Experimental evidence supporting the CHGNet predictions would advance Li-ion battery capacity and improve confidence in regards to the applicability of ML methods to real materials systems.

LIST OF REFERENCES

[1] K. E. Kushida, J. Murray, and J. Zysman, “Cloud Computing: From Scarcity to Abundance,” *J. Ind. Compet. Trade*, vol. 15, no. 1, pp. 5–19, Mar. 2015, doi: 10.1007/s10842-014-0188-y.

[2] G. H. Koch, M. P. H. Brongers, N. G. Thompson, Y. P. Virmani, and J. H. Payer, “Chapter 1 - Cost of corrosion in the United States,” in *Handbook of Environmental Degradation of Materials*, M. Kutz, Ed., Norwich, NY: William Andrew Publishing, 2005, pp. 3–24. doi: 10.1016/B978-081551500-5.50003-3.

[3] D. Pierce *et al.*, “High temperature materials for heavy duty diesel engines: Historical and future trends,” *Prog. Mater. Sci.*, vol. 103, pp. 109–179, Jun. 2019, doi: 10.1016/j.pmatsci.2018.10.004.

[4] R. K. Wild, “High temperature oxidation of austenitic stainless steel in low oxygen pressure,” *Corros. Sci.*, vol. 17, no. 2, pp. 87–104, Jan. 1977, doi: 10.1016/0010-938X(77)90011-7.

[5] F. J. Perez, M. J. Cristobal, G. Arnau, M. P. Hierro, and J. J. Saura, “High-Temperature Oxidation Studies of Low-Nickel Austenitic Stainless Steel. Part I: Isothermal Oxidation,” p. 14, 2001.

[6] C. S. Tedmon, D. A. Vermilyea, and J. H. Rosolowski, “Intergranular Corrosion of Austenitic Stainless Steel,” p. 12, 1971.

[7] I. Abdallah *et al.*, “Oxidation kinetics and microstructure evolution of high Mn stainless-steel alloy in CO2 at 700 °C,” *Corros. Sci.*, 2022, doi: 10.1016/j.corsci.2021.110013.

[8] E. Omri and H. Saadaoui, “An empirical investigation of the relationships between nuclear energy, economic growth, trade openness, fossil fuels, and carbon emissions in France: fresh evidence using asymmetric cointegration,” *Environ. Sci. Pollut. Res.*, vol. 30, no. 5, pp. 13224–13245, Jan. 2023, doi: 10.1007/s11356-022-22958-1.

[9] E. E. Michaelides and D. N. Michaelides, “Impact of nuclear energy on fossil fuel substitution,” *Nucl. Eng. Des.*, vol. 366, p. 110742, Sep. 2020, doi: 10.1016/j.nucengdes.2020.110742.

[10] D. Butler, “France digs deep for nuclear waste,” *Nature*, vol. 466, no. 7308, pp. 804–805, Aug. 2010, doi: 10.1038/466804a.

[11] P. de Preter, “SAFIR-2 and the Belgian methodological R and D programme on deep disposal,” Nuclear Energy Agency of the OECD (NEA), Jan. 2002.

[12] N. A. Wall *et al.*, “Functionalized Clays for Radionuclide Sequestration: A Review,” *ACS Earth Space Chem.*, vol. 6, no. 11, pp. 2552–2574, Nov. 2022, doi: 10.1021/acsearthspacechem.2c00098.

[13] Y.-G. Chen, L.-Y. Jia, W.-M. Ye, B. Chen, and Y.-J. Cui, “Advances in experimental investigation on hydraulic fracturing behavior of bentonite-based materials used for HLW disposal,” *Environ. Earth Sci.*, vol. 75, no. 9, p. 787, Apr. 2016, doi: 10.1007/s12665-016-5644-z.

[14] E. Maulden *et al.*, “Properties of iron-functionalized organoclays. Consequences for pertechnetate sequestration,” *Appl. Clay Sci.*, vol. 233, p. 106828, Mar. 2023, doi: 10.1016/j.clay.2023.106828.

[15] Z. Lun *et al.*, “Cation-disordered rocksalt-type high-entropy cathodes for Li-ion batteries,” *Nat. Mater.*, vol. 20, no. 2, Art. no. 2, Feb. 2021, doi: 10.1038/s41563-020-00816-0.

[16] D. A. Kitchaev *et al.*, “Design principles for high transition metal capacity in disordered rocksalt Li-ion cathodes,” *Energy Environ. Sci.*, vol. 11, no. 8, pp. 2159–2171, 2018, doi: 10.1039/C8EE00816G.

[17] M. A. Jones, P. J. Reeves, I. D. Seymour, M. J. Cliffe, S. E. Dutton, and C. P. Grey, “Short-range ordering in a battery electrode, the ‘cation-disordered’ rocksalt Li 1.25 Nb 0.25 Mn 0.5 O 2,” *Chem. Commun.*, vol. 55, no. 61, pp. 9027–9030, 2019, doi: 10.1039/C9CC04250D.

[18] N. Qiu, H. Chen, Z. Yang, S. Sun, Y. Wang, and Y. Cui, “A high entropy oxide (Mg0.2Co0.2Ni0.2Cu0.2Zn0.2O) with superior lithium storage performance,” *J. Alloys Compd.*, vol. 777, pp. 767–774, Mar. 2019, doi: 10.1016/j.jallcom.2018.11.049.

[19] J. Sturman, C.-H. Yim, E. A. Baranova, and Y. Abu-Lebdeh, “Communication—Design of LiNi0.2Mn0.2Co0.2Fe0.2Ti0.2O2 as a High-Entropy Cathode for Lithium-Ion Batteries Guided by Machine Learning,” *J. Electrochem. Soc.*, vol. 168, no. 5, p. 050541, May 2021, doi: 10.1149/1945-7111/ac00f4.

[20] M. Born and R. Oppenheimer, “Zur Quantentheorie der Molekeln,” *Ann. Phys.*, vol. 389, no. 20, pp. 457–484, 1927, doi: 10.1002/andp.19273892002.

[21] P. Hohenberg and W. Kohn, “Inhomogeneous Electron Gas,” *Phys. Rev.*, vol. 136, no. 3B, pp. B864–B871, Nov. 1964, doi: 10.1103/PhysRev.136.B864.

[22] W. Kohn and L. J. Sham, “Self-Consistent Equations Including Exchange and Correlation Effects,” *Phys. Rev.*, vol. 140, no. 4A, pp. A1133–A1138, Nov. 1965, doi: 10.1103/PhysRev.140.A1133.

[23] J. P. Perdew, K. Burke, and Y. Wang, “Generalized gradient approximation for the exchange-correlation hole of a many-electron system,” *Phys. Rev. B*, vol. 54, no. 23, pp. 16533–16539, Dec. 1996, doi: 10.1103/PhysRevB.54.16533.

[24] J. Tao, J. P. Perdew, V. N. Staroverov, and G. E. Scuseria, “Climbing the Density Functional Ladder: Nonempirical Meta--Generalized Gradient Approximation Designed for Molecules and Solids,” *Phys. Rev. Lett.*, vol. 91, no. 14, p. 146401, Sep. 2003, doi: 10.1103/PhysRevLett.91.146401.

[25] J. Sun *et al.*, “Accurate first-principles structures and energies of diversely bonded systems from an efficient density functional,” *Nat. Chem.*, vol. 8, no. 9, Art. no. 9, Sep. 2016, doi: 10.1038/nchem.2535.

[26] S. Kurth, J. P. Perdew, and P. Blaha, “Molecular and solid-state tests of density functional approximations: LSD, GGAs, and meta-GGAs,” *Int. J. Quantum Chem.*, vol. 75, no. 4–5, pp. 889–909, 1999, doi: 10.1002/(SICI)1097-461X(1999)75:4/5<889::AID-QUA54>3.0.CO;2-8.

[27] R. Ahlrichs, F. Furche, and S. Grimme, “Comment on ‘Assessment of exchange correlation functionals’ [A.J. Cohen, N.C. Handy, Chem. Phys. Lett. 316 (2000) 160–166],” *Chem. Phys. Lett.*, vol. 325, no. 1, pp. 317–321, Jul. 2000, doi: 10.1016/S0009-2614(00)00654-0.

[28] J. P. Perdew and Y. Wang, “Accurate and simple analytic representation of the electron-gas correlation energy,” *Phys. Rev. B*, vol. 45, no. 23, pp. 13244–13249, Jun. 1992, doi: 10.1103/PhysRevB.45.13244.

[29] J. P. Perdew and W. Yue, “Accurate and simple density functional for the electronic exchange energy: Generalized gradient approximation,” *Phys. Rev. B*, vol. 33, no. 12, pp. 8800–8802, Jun. 1986, doi: 10.1103/PhysRevB.33.8800.

[30] J. P. Perdew, K. Burke, and M. Ernzerhof, “Generalized Gradient Approximation Made Simple,” *Phys. Rev. Lett.*, vol. 77, no. 18, pp. 3865–3868, Oct. 1996, doi: 10.1103/PhysRevLett.77.3865.

[31] J. P. Perdew, K. Burke, and M. Ernzerhof, “Perdew, Burke, and Ernzerhof Reply:,” *Phys. Rev. Lett.*, vol. 80, no. 4, pp. 891–891, Jan. 1998, doi: 10.1103/PhysRevLett.80.891.

[32] R. Armiento and A. E. Mattsson, “Functional designed to include surface effects in self-consistent density functional theory,” *Phys. Rev. B*, vol. 72, no. 8, p. 085108, Aug. 2005, doi: 10.1103/PhysRevB.72.085108.

[33] A. E. Mattsson, R. Armiento, J. Paier, G. Kresse, J. M. Wills, and T. R. Mattsson, “The AM05 density functional applied to solids,” *J. Chem. Phys.*, vol. 128, no. 8, p. 084714, Feb. 2008, doi: 10.1063/1.2835596.

[34] S. L. Dudarev *et al.*, “Understanding STM images and EELS spectra of oxides with strongly correlated electrons: a comparison of nickel and uranium oxides,” *Micron*, vol. 31, no. 4, pp. 363–372, Aug. 2000, doi: 10.1016/S0968-4328(99)00115-8.

[35] S. L. Dudarev, G. A. Botton, S. Y. Savrasov, C. J. Humphreys, and A. P. Sutton, “Electron-energy-loss spectra and the structural stability of nickel oxide: An LSDA+U study,” *Phys. Rev. B*, vol. 57, no. 3, pp. 1505–1509, Jan. 1998, doi: 10.1103/PhysRevB.57.1505.

[36] P. E. Blöchl, “Projector augmented-wave method,” *Phys. Rev. B*, vol. 50, no. 24, pp. 17953–17979, Dec. 1994, doi: 10.1103/PhysRevB.50.17953.

[37] S. Steiner, S. Khmelevskyi, M. Marsmann, and G. Kresse, “Calculation of the magnetic anisotropy with projected-augmented-wave methodology and the case study of disordered Fe1-xCox alloys,” *Phys. Rev. B*, vol. 93, no. 22, p. 224425, Jun. 2016, doi: 10.1103/PhysRevB.93.224425.

[38] E. van Lenthe, R. van Leeuwen, E. J. Baerends, and J. G. Snijders, “Relativistic regular two-component Hamiltonians,” *Int. J. Quantum Chem.*, vol. 57, no. 3, pp. 281–293, 1996, doi: 10.1002/(SICI)1097-461X(1996)57:3<281::AID-QUA2>3.0.CO;2-U.

[39] D. Hobbs, G. Kresse, and J. Hafner, “Fully unconstrained noncollinear magnetism within the projector augmented-wave method,” *Phys. Rev. B*, vol. 62, no. 17, pp. 11556–11570, Nov. 2000, doi: 10.1103/PhysRevB.62.11556.

[40] W. C. Swope, H. C. Andersen, P. H. Berens, and K. R. Wilson, “A computer simulation method for the calculation of equilibrium constants for the formation of physical clusters of molecules: Application to small water clusters,” *J. Chem. Phys.*, vol. 76, no. 1, pp. 637–649, Jan. 1982, doi: 10.1063/1.442716.

[41] M. Griebel, S. Knapek, and G. W. Zumbusch, *Numerical simulation in molecular dynamics: numerics, algorithms, parallelization, applications*. in Texts in computational science and engineering, no. 5. Berlin: Springer, 2007.

[42] S. Nosé, “A unified formulation of the constant temperature molecular dynamics methods,” *J. Chem. Phys.*, vol. 81, no. 1, pp. 511–519, Jul. 1984, doi: 10.1063/1.447334.

[43] W. G. Hoover, “Canonical dynamics: Equilibrium phase-space distributions,” *Phys. Rev. A*, vol. 31, no. 3, pp. 1695–1697, Mar. 1985, doi: 10.1103/PhysRevA.31.1695.

[44] H. J. C. Berendsen, J. P. M. Postma, W. F. van Gunsteren, A. DiNola, and J. R. Haak, “Molecular dynamics with coupling to an external bath,” *J. Chem. Phys.*, vol. 81, no. 8, pp. 3684–3690, Oct. 1984, doi: 10.1063/1.448118.

[45] H. C. Andersen, “Molecular dynamics simulations at constant pressure and/or temperature,” *J. Chem. Phys.*, vol. 72, no. 4, pp. 2384–2393, Feb. 1980, doi: 10.1063/1.439486.

[46] M. Parrinello and A. Rahman, “Polymorphic transitions in single crystals: A new molecular dynamics method,” *J. Appl. Phys.*, vol. 52, no. 12, pp. 7182–7190, Dec. 1981, doi: 10.1063/1.328693.

[47] F. A. Faber, A. Lindmaa, O. A. von Lilienfeld, and R. Armiento, “Machine Learning Energies of 2 Million Elpasolite ABC2D6 Crystals,” *Phys. Rev. Lett.*, vol. 117, no. 13, p. 135502, Sep. 2016, doi: 10.1103/PhysRevLett.117.135502.

[48] D. Xue, P. V. Balachandran, J. Hogden, J. Theiler, D. Xue, and T. Lookman, “Accelerated search for materials with targeted properties by adaptive design,” *Nat. Commun.*, vol. 7, no. 1, Art. no. 1, Apr. 2016, doi: 10.1038/ncomms11241.

[49] A. Seko, A. Togo, H. Hayashi, K. Tsuda, L. Chaput, and I. Tanaka, “Prediction of Low-Thermal-Conductivity Compounds with First-Principles Anharmonic Lattice-Dynamics Calculations and Bayesian Optimization,” *Phys. Rev. Lett.*, vol. 115, no. 20, p. 205901, Nov. 2015, doi: 10.1103/PhysRevLett.115.205901.

[50] A. P. Bartók, R. Kondor, and G. Csányi, “On representing chemical environments,” *Phys. Rev. B*, vol. 87, no. 18, p. 184115, May 2013, doi: 10.1103/PhysRevB.87.184115.

[51] L. Himanen *et al.*, “DScribe: Library of descriptors for machine learning in materials science,” *Comput. Phys. Commun.*, vol. 247, p. 106949, Feb. 2020, doi: 10.1016/j.cpc.2019.106949.

[52] M. Rupp, A. Tkatchenko, K.-R. Müller, and O. A. von Lilienfeld, “Fast and Accurate Modeling of Molecular Atomization Energies with Machine Learning,” *Phys. Rev. Lett.*, vol. 108, no. 5, p. 058301, Jan. 2012, doi: 10.1103/PhysRevLett.108.058301.

[53] F. Faber, A. Lindmaa, O. A. von Lilienfeld, and R. Armiento, “Crystal structure representations for machine learning models of formation energies,” *Int. J. Quantum Chem.*, vol. 115, no. 16, pp. 1094–1101, 2015, doi: 10.1002/qua.24917.

[54] H. Huo and M. Rupp, “Unified Representation of Molecules and Crystals for Machine Learning,” *ArXiv170406439 Cond-Mat Physicsphysics*, Jan. 2018, Accessed: Nov. 07, 2021. [Online]. Available: http://arxiv.org/abs/1704.06439

[55] Y. LeCun, Y. Bengio, and G. Hinton, “Deep learning,” *Nature*, vol. 521, no. 7553, Art. no. 7553, May 2015, doi: 10.1038/nature14539.

[56] A. Krizhevsky, I. Sutskever, and G. E. Hinton, “ImageNet Classification with Deep Convolutional Neural Networks,” in *Advances in Neural Information Processing Systems*, Curran Associates, Inc., 2012. Accessed: Feb. 01, 2024. [Online]. Available: https://papers.nips.cc/paper_files/paper/2012/hash/c399862d3b9d6b76c8436e924a68c45b-Abstract.html

[57] R. Collobert and J. Weston, “A unified architecture for natural language processing: deep neural networks with multitask learning,” in *Proceedings of the 25th international conference on Machine learning*, in ICML ’08. New York, NY, USA: Association for Computing Machinery, Jul. 2008, pp. 160–167. doi: 10.1145/1390156.1390177.

[58] D. K. Duvenaud *et al.*, “Convolutional Networks on Graphs for Learning Molecular Fingerprints,” in *Advances in Neural Information Processing Systems*, Curran Associates, Inc., 2015. Accessed: Feb. 01, 2024. [Online]. Available: https://papers.nips.cc/paper_files/paper/2015/hash/f9be311e65d81a9ad8150a60844bb94c-Abstract.html

[59] T. Xie and J. C. Grossman, “Crystal Graph Convolutional Neural Networks for an Accurate and Interpretable Prediction of Material Properties,” *Phys. Rev. Lett.*, vol. 120, no. 14, p. 145301, Apr. 2018, doi: 10.1103/PhysRevLett.120.145301.

[60] C. W. Park and C. Wolverton, “Developing an improved crystal graph convolutional neural network framework for accelerated materials discovery,” *Phys. Rev. Mater.*, vol. 4, no. 6, p. 063801, Jun. 2020, doi: 10.1103/PhysRevMaterials.4.063801.

[61] M. Karamad, R. Magar, Y. Shi, S. Siahrostami, I. D. Gates, and A. B. Farimani, “Orbital Graph Convolutional Neural Network for Material Property Prediction,” *Phys. Rev. Mater.*, vol. 4, no. 9, p. 093801, Sep. 2020, doi: 10.1103/PhysRevMaterials.4.093801.

[62] J. Cheng, C. Zhang, and L. Dong, “A geometric-information-enhanced crystal graph network for predicting properties of materials,” *Commun. Mater.*, vol. 2, no. 1, Art. no. 1, Sep. 2021, doi: 10.1038/s43246-021-00194-3.

[63] B. Deng *et al.*, “CHGNet as a pretrained universal neural network potential for charge-informed atomistic modelling,” *Nat. Mach. Intell.*, vol. 5, no. 9, pp. 1031–1041, Sep. 2023, doi: 10.1038/s42256-023-00716-3.

[64] A. Jain *et al.*, “Commentary: The Materials Project: A materials genome approach to accelerating materials innovation,” *APL Mater.*, vol. 1, no. 1, p. 011002, Jul. 2013, doi: 10.1063/1.4812323.

[65] F. Otto, Y. Yang, H. Bei, and E. P. George, “Relative effects of enthalpy and entropy on the phase stability of equiatomic high-entropy alloys,” *Acta Mater.*, vol. 61, no. 7, pp. 2628–2638, Apr. 2013, doi: 10.1016/j.actamat.2013.01.042.

[66] D. Gehringer, M. Friák, and D. Holec, “Models of configurationally-complex alloys made simple,” *Comput. Phys. Commun.*, vol. 286, p. 108664, May 2023, doi: 10.1016/j.cpc.2023.108664.

[67] A. Zunger, S.-H. Wei, L. G. Ferreira, and J. E. Bernard, “Special quasirandom structures,” *Phys. Rev. Lett.*, vol. 65, no. 3, pp. 353–356, Jul. 1990, doi: 10.1103/PhysRevLett.65.353.

[68] D. L. Douglass, F. Gesmundo, and C. de Asmundis, “The air oxidation of an austenitic Fe-Mn-Cr stainless steel for fusion-reactor applications,” *Oxid. Met.*, vol. 25, no. 3–4, pp. 235–268, Apr. 1986, doi: 10.1007/BF00655899.

[69] D. L. Douglass and J. S. Armijo, “The effect of silicon and manganese on the oxidation mechanism of Ni-20 Cr,” *Oxid. Met.*, vol. 2, no. 2, pp. 207–231, 1970, doi: 10.1007/BF00603657.

[70] D. L. Douglass and F. Rizzo-Assuncao, “The oxidation of Fe-19.6Cr-15.1Mn stainless steel,” *Oxid. Met.*, vol. 29, no. 3–4, pp. 271–287, Apr. 1988, doi: 10.1007/BF00751800.

[71] A. L. Marasco and D. J. Young, “The Oxidation of Iron-Chromium-Manganese Alloys at 900 C,” p. 18, 1991.

[72] M. Ekström, “Oxidation and corrosion fatigue aspects of cast exhaust manifolds,” 2015, [Online]. Available: http://urn.kb.se/resolve?urn=urn:nbn:se:kth:diva-166274

[73] T. Gheno, D. Monceau, J. Zhang, and D. J. Young, “Carburisation of ferritic Fe–Cr alloys by low carbon activity gases,” *Corros. Sci.*, vol. 53, no. 9, pp. 2767–2777, Sep. 2011, doi: 10.1016/j.corsci.2011.05.013.

[74] “Identification of MnCr2O4 nano-octahedron in catalysing pitting corrosion of austenitic stainless steels.” [Online]. Available: https://reader.elsevier.com/reader/sd/pii/S1359645410003289?token=82713300A022B6261B87EC183879B5B40E87A40308E27B2C978F8FC4E9BA5B0C19401ED906557C43B419F1C8E1E088C9

[75] C. A. Gilbert, R. Smith, S. D. Kenny, S. T. Murphy, R. W. Grimes, and J. A. Ball, “A theoretical study of intrinsic point defects and defect clusters in magnesium aluminate spinel,” *J. Phys. Condens. Matter*, vol. 21, no. 27, p. 275406, Jun. 2009, doi: 10.1088/0953-8984/21/27/275406.

[76] D. Bacorisen, R. Smith, B. P. Uberuaga, K. E. Sickafus, J. A. Ball, and R. W. Grimes, “Atomistic simulations of radiation-induced defect formation in spinels: MgAl2O4, MgGa2O4, and MgIn2O4,” *Phys. Rev. B*, vol. 74, no. 21, p. 214105, Dec. 2006, doi: 10.1103/PhysRevB.74.214105.

[77] B. P. Uberuaga *et al.*, “Defect kinetics in spinels: Long-time simulations of MgAl2O4, MgGa2O4, and MgIn2O4,” *Phys. Rev. B*, vol. 75, no. 10, p. 104116, Mar. 2007, doi: 10.1103/PhysRevB.75.104116.

[78] J. A. Ball *et al.*, “Defect processes in MgAl2O4 spinel,” *Solid State Sci.*, vol. 10, no. 6, pp. 717–724, Jun. 2008, doi: 10.1016/j.solidstatesciences.2007.04.005.

[79] R. Smith, D. Bacorisen, B. P. Uberuaga, K. E. Sickafus, J. A. Ball, and R. W. Grimes, “Dynamical simulations of radiation damage in magnesium aluminate spinel, MgAl2O4,” *J. Phys. Condens. Matter*, vol. 17, no. 6, pp. 875–891, Jan. 2005, doi: 10.1088/0953-8984/17/6/008.

[80] B. P. Uberuaga and G. Pilania, “Inversion, chemical complexity, and interstitial transport in spinels,” *J. Am. Ceram. Soc.*, vol. 104, no. 5, pp. 2313–2324, 2021, doi: 10.1111/jace.17598.

[81] C. L. Muhich, V. J. Aston, R. M. Trottier, A. W. Weimer, and C. B. Musgrave, “First-Principles Analysis of Cation Diffusion in Mixed Metal Ferrite Spinels,” *Chem. Mater.*, vol. 28, no. 1, pp. 214–226, Jan. 2016, doi: 10.1021/acs.chemmater.5b03911.

[82] J. Gilewicz-Wolter, “Diffusion of Chromium, Manganese, and Iron in MnCr2O4 Spinel,” vol. 26, no. 5, p. 4, 2005.

[83] G. Kresse and J. Hafner, “Ab initio molecular dynamics for liquid metals,” *Phys. Rev. B*, vol. 47, no. 1, pp. 558–561, Jan. 1993, doi: 10.1103/PhysRevB.47.558.

[84] G. Kresse and J. Furthmüller, “Efficiency of ab-initio total energy calculations for metals and semiconductors using a plane-wave basis set,” *Comput. Mater. Sci.*, vol. 6, no. 1, pp. 15–50, Jul. 1996, doi: 10.1016/0927-0256(96)00008-0.

[85] G. Kresse and J. Furthmüller, “Efficient iterative schemes for ab initio total-energy calculations using a plane-wave basis set,” *Phys. Rev. B*, vol. 54, no. 16, pp. 11169–11186, Oct. 1996, doi: 10.1103/PhysRevB.54.11169.

[86] G. Kresse and D. Joubert, “From ultrasoft pseudopotentials to the projector augmented-wave method,” *Phys. Rev. B*, vol. 59, no. 3, pp. 1758–1775, Jan. 1999, doi: 10.1103/PhysRevB.59.1758.

[87] C. Franchini, R. Podloucky, J. Paier, M. Marsman, and G. Kresse, “Ground-state properties of multivalent manganese oxides: Density functional and hybrid density functional calculations,” *Phys. Rev. B*, vol. 75, no. 19, p. 195128, May 2007, doi: 10.1103/PhysRevB.75.195128.

[88] H. J. Monkhorst and J. D. Pack, “Special points for Brillouin-zone integrations,” *Phys. Rev. B*, vol. 13, no. 12, pp. 5188–5192, Jun. 1976, doi: 10.1103/PhysRevB.13.5188.

[89] P. E. Blöchl, O. Jepsen, and O. K. Andersen, “Improved tetrahedron method for Brillouin-zone integrations,” *Phys. Rev. B*, vol. 49, no. 23, pp. 16223–16233, Jun. 1994, doi: 10.1103/PhysRevB.49.16223.

[90] C. Freysoldt, “Manual for sxdefectalign version 2.2,” p. 11, Feb. 2019.

[91] C. Freysoldt *et al.*, “First-principles calculations for point defects in solids,” *Rev. Mod. Phys.*, vol. 86, no. 1, pp. 253–305, Mar. 2014, doi: 10.1103/RevModPhys.86.253.

[92] C. Freysoldt, J. Neugebauer, and C. G. Van de Walle, “Fully Ab Initio Finite-Size Corrections for Charged-Defect Supercell Calculations,” *Phys. Rev. Lett.*, vol. 102, no. 1, p. 016402, Jan. 2009, doi: 10.1103/PhysRevLett.102.016402.

[93] M. W. Finnis, A. Y. Lozovoi, and A. Alavi, “The Oxidation of NiAl: What Can We Learn from Ab Initio Calculations?,” *Annu. Rev. Mater. Res.*, vol. 35, no. 1, pp. 167–207, 2005, doi: 10.1146/annurev.matsci.35.101503.091652.

[94] W. Bergermayer, H. Schweiger, and E. Wimmer, “Ab initio thermodynamics of oxide surfaces: O 2 on Fe 2 O 3 (0001),” *Phys. Rev. B*, vol. 69, no. 19, p. 195409, May 2004, doi: 10.1103/PhysRevB.69.195409.

[95] T. Lee, Y. Lee, S. Piccinin, and A. Soon, “Ab Initio Thermodynamics of Surface Oxide Structures under Controlled Growth Conditions,” *J. Phys. Chem. C*, vol. 121, no. 4, pp. 2228–2233, Feb. 2017, doi: 10.1021/acs.jpcc.6b11445.

[96] K. Reuter and M. Scheffler, “First-Principles Atomistic Thermodynamics for Oxidation Catalysis: Surface Phase Diagrams and Catalytically Interesting Regions,” *Phys. Rev. Lett.*, vol. 90, no. 4, p. 046103, Jan. 2003, doi: 10.1103/PhysRevLett.90.046103.

[97] W. X. Li *et al.*, “Oxidation of Pt(110),” *Phys. Rev. Lett.*, vol. 93, no. 14, p. 146104, Sep. 2004, doi: 10.1103/PhysRevLett.93.146104.

[98] J. Gustafson *et al.*, “Self-Limited Growth of a Thin Oxide Layer on Rh(111),” *Phys. Rev. Lett.*, vol. 92, no. 12, p. 126102, Mar. 2004, doi: 10.1103/PhysRevLett.92.126102.

[99] W. Zhang, J. R. Smith, and X.-G. Wang, “Thermodynamics from ab initio computations,” *Phys. Rev. B*, vol. 70, no. 2, p. 024103, Jul. 2004, doi: 10.1103/PhysRevB.70.024103.

[100] C. Gray, Y. Lei, and G. Wang, “Charged vacancy diffusion in chromium oxide crystal: DFT and DFT+U predictions,” *J. Appl. Phys.*, vol. 120, no. 21, p. 215101, Dec. 2016, doi: 10.1063/1.4970882.

[101] J. Malcolm W. Chase, *NIST-JANAF thermochemical tables*. Fourth edition. Washington, DC : American Chemical Society ; New York : American Institute of Physics for the National Institute of Standards and Technology, 1998., 1998. [Online]. Available: https://search.library.wisc.edu/catalog/999842910902121

[102] G. Henkelman, B. P. Uberuaga, and H. Jónsson, “A climbing image nudged elastic band method for finding saddle points and minimum energy paths,” *J. Chem. Phys.*, vol. 113, no. 22, pp. 9901–9904, Dec. 2000, doi: 10.1063/1.1329672.

[103] G. Henkelman and H. Jónsson, “Improved tangent estimate in the nudged elastic band method for finding minimum energy paths and saddle points,” *J. Chem. Phys.*, vol. 113, no. 22, pp. 9978–9985, Dec. 2000, doi: 10.1063/1.1323224.

[104] F. S. Galasso, *Structure and Properties of Inorganic Solids: International Series of Monographs in Solid State Physics*. Elsevier, 2016.

[105] E. Stoll, P. Fischer, W. Hälg, and G. Maier, “Redetermination of the cation distribution of spinel (MgAl2O4) by means of neutron diffraction,” *J. Phys.*, vol. 25, no. 5, pp. 447–448, 1964, doi: 10.1051/jphys:01964002505044700.

[106] U. Schmocker and F. Waldner, “The inversion parameter with respect to the space group of $MgAl_2O_4$ spinels,” *J. Phys. C Solid State Phys.*, vol. 9, no. 9, pp. L235–L237, May 1976, doi: 10.1088/0022-3719/9/9/003.

[107] “Thermodynamic assessment of the Cr-Mn-O system.” [Online]. Available: https://reader.elsevier.com/reader/sd/pii/S0925838810014660?token=453B0E0C779164FB89283C61E39610B4B073EF2457DB9F4BE6409D32158E3F072D257419360099CC9F4832012C483272&originRegion=us-east-1&originCreation=20221031231755

[108] K. E. Sickafus, J. M. Wills, and N. W. Grimes, “Structure of Spinel,” *J. Am. Ceram. Soc.*, vol. 82, no. 12, pp. 3279–3292, 1999, doi: https://doi.org/10.1111/j.1151-2916.1999.tb02241.x.

[109] S. Kirklin *et al.*, “The Open Quantum Materials Database (OQMD): assessing the accuracy of DFT formation energies,” *Npj Comput. Mater.*, vol. 1, no. 1, Art. no. 1, Dec. 2015, doi: 10.1038/npjcompumats.2015.10.

[110] Z. Lu, J. Zhu, E. A. Payzant, and M. P. Paranthaman, “Electrical Conductivity of the Manganese Chromite Spinel Solid Solution,” *J. Am. Ceram. Soc.*, vol. 88, no. 4, pp. 1050–1053, 2005, doi: https://doi.org/10.1111/j.1551-2916.2005.00205.x.

[111] N. K. Othman, O. Othman, J. Zhang, and D. Young, “Water Vapour Effects of Cyclic Oxidation on Fe-Cr Alloys,” *Sains Malays.*, vol. 39, pp. 249–259, Apr. 2010.

[112] T. Gheno, D. Monceau, and D. J. Young, “Kinetics of breakaway oxidation of Fe–Cr and Fe–Cr–Ni alloys in dry and wet carbon dioxide,” *Corros. Sci.*, vol. 77, pp. 246–256, Dec. 2013, doi: 10.1016/j.corsci.2013.08.008.

[113] T. D. Nguyen, J. Zhang, and D. J. Young, “Effects of cerium and manganese on corrosion of Fe–Cr and Fe–Cr–Ni alloys in Ar–20CO2 gas at 818 °C,” *Corros. Sci.*, vol. 76, pp. 231–242, Nov. 2013, doi: 10.1016/j.corsci.2013.06.046.

[114] R. S. Ullberg, X. Wu, M. R. Tonks, and S. R. Phillpot, “Energetics and diffusion kinetics of point defects in MnCr2O4 spinel from first principles,” *J. Phys. Chem. Solids*, vol. 181, p. 111519, 2023.

[115] B. Medasani, M. L. Sushko, K. M. Rosso, D. K. Schreiber, and S. M. Bruemmer, “First-Principles Investigation of Native Interstitial Diffusion in Cr2O3,” *J. Phys. Chem. C*, vol. 122, no. 24, pp. 12984–12993, Jun. 2018, doi: 10.1021/acs.jpcc.8b04383.

[116] V. Irmer and M. Feller-Kniepmeier, “Diffusion of manganese in α-iron single crystals of different purity,” *J. Phys. Chem. Solids*, vol. 33, no. 11, pp. 2141–2148, Jan. 1972, doi: 10.1016/S0022-3697(72)80244-0.

[117] X. Wu *et al.*, “A phase-field study of stainless-steel oxidation from high-temperature carbon dioxide exposure,” *Comput. Mater. Sci.*, vol. 218, p. 111996, 2023.

[118] M. Tonks, S. Phillpott, A. Couet, J. Perepezko, W. Jiang, and M. Carroll, “Multiscale Development and Validation of the Stainless Steel Alloy Corrosion (SStAC) Tool for High Temperature Engine Materials,” DOE-UF--08459, 1972203, Apr. 2023. doi: 10.2172/1972203.

[119] P. A. Kharecha and J. E. Hansen, “Prevented Mortality and Greenhouse Gas Emissions from Historical and Projected Nuclear Power,” *Environ. Sci. Technol.*, vol. 47, no. 9, pp. 4889–4895, May 2013, doi: 10.1021/es3051197.

[120] S. Ramírez, P. Vieillard, A. Bouchet, A. Cassagnabère, A. Meunier, and E. Jacquot, “Alteration of the Callovo–Oxfordian clay from Meuse-Haute Marne underground laboratory (France) by alkaline solution. I. A XRD and CEC study,” *Appl. Geochem.*, vol. 20, no. 1, pp. 89–99, Jan. 2005, doi: 10.1016/j.apgeochem.2004.03.009.

[121] S. Altmann, C. Tournassat, F. Goutelard, J.-C. Parneix, T. Gimmi, and N. Maes, “Diffusion-driven transport in clayrock formations,” *Appl. Geochem.*, vol. 27, no. 2, pp. 463–478, Feb. 2012, doi: 10.1016/j.apgeochem.2011.09.015.

[122] M. Bradbury and B. Baeyens, “Near Field sorption Data Bases for Compacted MX-80 Bentonite for Performance Assessment of a High-Level Radioactive Waste Repository in Opalinus Clay Host Rock,” U.S. Department of Energy Office of Scientific and Technical Information, Aug. 2003. Accessed: Jul. 31, 2023. [Online]. Available: https://www.osti.gov/etdeweb/biblio/20406661

[123] H. Van Olphen, *An introduction to clay colloid chemistry : for clay technologists, geologists, and soil scientists*, 2nd ed. Krieger Pub. Co., 1991. Accessed: Jul. 31, 2023. [Online]. Available: https://cir.nii.ac.jp/crid/1130000794872801792

[124] E. Ferrage, B. Lanson, B. A. Sakharov, and V. A. Drits, “Investigation of smectite hydration properties by modeling experimental X-ray diffraction patterns: Part I. Montmorillonite hydration properties,” *Am. Mineral.*, vol. 90, no. 8–9, pp. 1358–1374, Aug. 2005, doi: 10.2138/am.2005.1776.

[125] B. Rotenberg, V. Marry, N. Malikova, and P. Turq, “Molecular simulation of aqueous solutions at clay surfaces,” *J. Phys. Condens. Matter*, vol. 22, no. 28, p. 284114, Jun. 2010, doi: 10.1088/0953-8984/22/28/284114.

[126] A. W. Miller and Y. Wang, “Radionuclide Interaction with Clays in Dilute and Heavily Compacted Systems: A Critical Review,” *Environ. Sci. Technol.*, vol. 46, no. 4, pp. 1981–1994, Feb. 2012, doi: 10.1021/es203025q.

[127] H. Geckeis, J. Lutzenkirchen, R. Polly, T. Rabung, and M. Schmidt, “Mineral–Water Interface Reactions of Actinides,” *Chem. Rev.*, 2013, doi: 10.1021/cr300370h.

[128] R. C. Moore *et al.*, “Iodine immobilization by materials through sorption and redox-driven processes: A literature review,” *Sci. Total Environ.*, vol. 716, p. 132820, May 2020, doi: 10.1016/j.scitotenv.2019.06.166.

[129] A. H. Meena and Y. Arai, “Environmental geochemistry of technetium,” *Environ. Chem. Lett.*, vol. 15, no. 2, pp. 241–263, Jun. 2017, doi: 10.1007/s10311-017-0605-7.

[130] L. Zhu *et al.*, “Identifying the Recognition Site for Selective Trapping of 99TcO4– in a Hydrolytically Stable and Radiation Resistant Cationic Metal–Organic Framework,” *J. Am. Chem. Soc.*, vol. 139, no. 42, pp. 14873–14876, Oct. 2017, doi: 10.1021/jacs.7b08632.

[131] Z. Wang and L. Liu, “A density functional study of the swelling behaviors of Na-bentonite,” presented at the Clays in natural and engineered barriers for radioactive waste confinement - 5 International meeting Book of abstracts, France, 2012, p. 923.

[132] L. Sun, J. T. Hirvi, T. Schatz, S. Kasa, and T. A. Pakkanen, “Estimation of Montmorillonite Swelling Pressure: A Molecular Dynamics Approach,” *J. Phys. Chem. C*, 2015, doi: 10.1021/acs.jpcc.5b04972.

[133] X. Zheng, T. R. Underwood, and I. C. Bourg, “Molecular dynamics simulation of thermal, hydraulic, and mechanical properties of bentonite clay at 298 to 373 K,” *Appl. Clay Sci.*, vol. 240, p. 106964, Aug. 2023, doi: 10.1016/j.clay.2023.106964.

[134] C. Tournassat, IanC. Bourg, M. Holmboe, G. Sposito, and CarlI. Steefel, “Molecular Dynamics Simulations of Anion Exclusion in Clay Interlayer Nanopores,” *Clays Clay Miner.*, vol. 64, no. 4, pp. 374–388, Aug. 2016, doi: 10.1346/CCMN.2016.0640403.

[135] G. Kosakowski, S. V. Churakov, and T. Thoenen, “Diffusion of Na and Cs in Montmorillonite,” *Clays Clay Miner.*, vol. 56, no. 2, pp. 190–206, Apr. 2008, doi: 10.1346/CCMN.2008.0560205.

[136] J. A. Greathouse, R. T. Cygan, J. T. Fredrich, and G. R. Jerauld, “Molecular Dynamics Simulation of Diffusion and Electrical Conductivity in Montmorillonite Interlayers,” *J. Phys. Chem. C*, vol. 120, no. 3, pp. 1640–1649, Jan. 2016, doi: 10.1021/acs.jpcc.5b10851.

[137] B. F. Ngouana W. and A. G. Kalinichev, “Structural Arrangements of Isomorphic Substitutions in Smectites: Molecular Simulation of the Swelling Properties, Interlayer Structure, and Dynamics of Hydrated Cs–Montmorillonite Revisited with New Clay Models,” *J. Phys. Chem. C*, vol. 118, no. 24, pp. 12758–12773, Jun. 2014, doi: 10.1021/jp500538z.

[138] A. G. Newton, K. D. Kwon, and D.-K. Cheong, “Edge Structure of Montmorillonite from Atomistic Simulations,” *Minerals*, vol. 6, no. 2, Art. no. 2, Jun. 2016, doi: 10.3390/min6020025.

[139] J. H. Lee and S. Guggenheim, “Single crystal X-ray refinement of pyrophyllite-1Tc,” *Am. Mineral.*, vol. 66, no. 3–4, pp. 350–357, Apr. 1981.

[140] L. P. Lavikainen, J. T. Hirvi, S. Kasa, T. Schatz, and T. A. Pakkanen, “Stability of dioctahedral 2:1 phyllosilicate edge structures based on pyrophyllite models,” *Theor. Chem. Acc.*, vol. 134, no. 9, p. 112, Aug. 2015, doi: 10.1007/s00214-015-1715-6.

[141] G. N. White, “Analysis and Implications of the Edge Structure of Dioctahedral Phyllosilicates,” *Clays Clay Miner.*, vol. 36, no. 2, pp. 141–146, 1988, doi: 10.1346/CCMN.1988.0360207.

[142] B. R. Bickmore, K. M. Rosso, K. L. Nagy, R. T. Cygan, and C. J. Tadanier, “Ab Initio Determination of Edge Surface Structures for Dioctahedral 2:1 Phyllosilicates: Implications for Acid-Base Reactivity,” *Clays Clay Miner.*, vol. 51, no. 4, pp. 359–371, Aug. 2003, doi: 10.1346/CCMN.2003.0510401.

[143] S. V. Churakov, “Ab Initio Study of Sorption on Pyrophyllite: Structure and Acidity of the Edge Sites,” *J. Phys. Chem. B*, vol. 110, no. 9, pp. 4135–4146, Mar. 2006, doi: 10.1021/jp053874m.

[144] X. Liu, J. Cheng, M. Sprik, X. Lu, and R. Wang, “Surface acidity of 2:1-type dioctahedral clay minerals from first principles molecular dynamics simulations,” *Geochim. Cosmochim. Acta*, vol. 140, pp. 410–417, Sep. 2014, doi: 10.1016/j.gca.2014.05.044.

[145] A. G. Newton and G. Sposito, “Molecular Dynamics Simulations of Pyrophyllite Edge Surface: Structure, Surface Energies, and Solvent Accessibility,” *Clays Clay Miner.*, vol. 63, no. 4, pp. 277–289, Aug. 2015, doi: 10.1346/CCMN.2015.0630403.

[146] A. T. Ta, R. S. Ullberg, and S. R. Phillpot, “Surface Reconstruction and Cleavage of Phyllosilicate Clay Edge by Density Functional Theory,” *Appl. Clay Sci.*, vol. 246, p. 107178, 2023, doi: 10.1016/j.clay.2023.107178.

[147] J. Qiu *et al.*, “Crystal chemistry characteristics and dispersion performance of Ca-montmorillonite with different layer charge density,” *Mater. Res. Express*, vol. 7, no. 7, p. 075505, Jul. 2020, doi: 10.1088/2053-1591/aba803.

[148] S. P. Pinho and E. A. Macedo, “Solubility of NaCl, NaBr, and KCl in Water, Methanol, Ethanol, and Their Mixed Solvents,” *J. Chem. Eng. Data*, vol. 50, no. 1, pp. 29–32, Jan. 2005, doi: 10.1021/je049922y.

[149] A. P. Thompson *et al.*, “LAMMPS - a flexible simulation tool for particle-based materials modeling at the atomic, meso, and continuum scales,” *Comput. Phys. Commun.*, vol. 271, p. 108171, Feb. 2022, doi: 10.1016/j.cpc.2021.108171.

[150] S. Plimpton, “Fast Parallel Algorithms for Short-Range Molecular Dynamics,” *J. Comput. Phys.*, vol. 117, no. 1, pp. 1–19, Mar. 1995, doi: 10.1006/jcph.1995.1039.

[151] A. I. Jewett, D. Stelter, J. Lambert, S. M. Saladi, and O. M. Roscioni, “Moltemplate: A Tool for Coarse-Grained Modeling of Complex Biological Matter and Soft Condensed Matter Physics | Elsevier Enhanced Reader,” *J. Mol. Biol.*, 2021, doi: 10.1016/j.jmb.2021.166841.

[152] R. T. Cygan, J.-J. Liang, and A. G. Kalinichev, “Molecular Models of Hydroxide, Oxyhydroxide, and Clay Phases and the Development of a General Force Field,” *J. Phys. Chem. B*, vol. 108, no. 4, pp. 1255–1266, Jan. 2004, doi: 10.1021/jp0363287.

[153] H. J. C. Berendsen, J. R. Grigera, and T. P. Straatsma, “The missing term in effective pair potentials,” *J. Phys. Chem.*, vol. 91, no. 24, pp. 6269–6271, Nov. 1987, doi: 10.1021/j100308a038.

[154] J.-P. Ryckaert, G. Ciccotti, and H. J. C. Berendsen, “Numerical integration of the cartesian equations of motion of a system with constraints: molecular dynamics of n-alkanes,” *J. Comput. Phys.*, vol. 23, no. 3, pp. 327–341, Mar. 1977, doi: 10.1016/0021-9991(77)90098-5.

[155] D. E. Smith and L. X. Dang, “Computer simulations of NaCl association in polarizable water,” *J. Chem. Phys.*, vol. 100, no. 5, pp. 3757–3766, Mar. 1994, doi: 10.1063/1.466363.

[156] B. Rotenberg, “Water and ions in clays : Unraveling the interlayer/micropore exchange using molecular dynamics,” *Geochim. Cosmochim. Acta*, 2007, doi: 10.1016/j.gca.2007.08.018.

[157] M. Hedström and O. Karnland, “Donnan equilibrium in Na-montmorillonite from a molecular dynamics perspective,” *Geochim. Cosmochim. Acta*, 2012, doi: 10.1016/j.gca.2011.11.007.

[158] Y.-W. Hsiao and M. Hedström, “Molecular Dynamics Simulations of NaCl Permeation in Bihydrated Montmorillonite Interlayer Nanopores,” *J. Phys. Chem. C*, vol. 119, no. 30, pp. 17352–17361, Jul. 2015, doi: 10.1021/acs.jpcc.5b01169.

[159] B. Ma, L. Charlet, A. Fernandez-Martinez, M. Kang, and B. Madé, “A review of the retention mechanisms of redox-sensitive radionuclides in multi-barrier systems,” *Appl. Geochem.*, vol. 100, pp. 414–431, 2019.

[160] P. Sellin and O. X. Leupin, “THE USE OF CLAY AS AN ENGINEERED BARRIER IN RADIOACTIVE-WASTE MANAGEMENT – A REVIEW,” *Clays Clay Miner.*, vol. 61, no. 6, pp. 477–498, Dec. 2013, doi: 10.1346/CCMN.2013.0610601.

[161] A. Milutinović-Nikolić *et al.*, “Removal of 99Tc (VII) by organo-modified bentonite,” *Appl. Clay Sci.*, vol. 95, pp. 294–302, 2014.

[162] E. M. Baum, H. D. Knox, and T. R. Miller, “Nuclides and isotopes,” *No Title*, 2002.

[163] J. E. Szecsody *et al.*, “Remediation of technetium in vadose zone sediments using ammonia and hydrogen sulfide gases,” *Vadose Zone J.*, vol. 14, no. 7, pp. 1–12, 2015.

[164] S. Marras, A. Tsimpliaraki, I. Zuburtikudis, and C. Panayiotou, “Thermal and colloidal behavior of amine-treated clays: The role of amphiphilic organic cation concentration,” *J. Colloid Interface Sci.*, vol. 315, no. 2, pp. 520–527, 2007.

[165] Q. Zhao and S. E. Burns, “Microstructure of Single Chain Quaternary Ammonium Cations Intercalated into Montmorillonite: A Molecular Dynamics Study,” *Langmuir*, vol. 28, no. 47, pp. 16393–16400, Nov. 2012, doi: 10.1021/la303422p.

[166] J. Qiu *et al.*, “Molecular dynamics simulation and experimental study of micro-structure and gel properties of single chain alkyl ammonium intercalated Na-montmorillonite,” *J. Appl. Polym. Sci.*, vol. 139, no. 23, p. 52310, 2022, doi: 10.1002/app.52310.

[167] Q. H. Zeng, A. B. Yu, G. Q. Lu, and R. K. Standish, “Molecular Dynamics Simulation of the Structural and Dynamic Properties of Dioctadecyldimethyl Ammoniums in Organoclays,” *J. Phys. Chem. B*, vol. 108, no. 28, pp. 10025–10033, Jul. 2004, doi: 10.1021/jp037245t.

[168] M. Slaný, L. Jankovič, and J. Madejová, “Near-IR study of the impact of alkyl-ammonium and -phosphonium cations on the hydration of montmorillonite,” *J. Mol. Struct.*, vol. 1256, p. 132568, May 2022, doi: 10.1016/j.molstruc.2022.132568.

[169] Q. H. Zeng, A. B. Yu, G. Q. Lu, and R. K. Standish, “Molecular Dynamics Simulation of Organic−Inorganic Nanocomposites: Layering Behavior and Interlayer Structure of Organoclays,” *Chem. Mater.*, vol. 15, no. 25, pp. 4732–4738, Dec. 2003, doi: 10.1021/cm0342952.

[170] L. Martínez, R. Andrade, E. G. Birgin, and J. M. Martínez, “PACKMOL: A package for building initial configurations for molecular dynamics simulations,” *J. Comput. Chem.*, vol. 30, no. 13, pp. 2157–2164, 2009, doi: 10.1002/jcc.21224.

[171] X. He, V. H. Man, W. Yang, T.-S. Lee, and J. Wang, “A fast and high-quality charge model for the next generation general AMBER force field,” *J. Chem. Phys.*, vol. 153, no. 11, p. 114502, Sep. 2020, doi: 10.1063/5.0019056.

[172] J. Zhu, H. He, J. Guo, D. Yang, and X. Xie, “Arrangement models of alkylammonium cations in the interlayer of HDTMA+ pillared montmorillonites,” *Chin. Sci. Bull.*, vol. 48, no. 4, pp. 368–372, Feb. 2003, doi: 10.1007/BF03183232.

[173] N. Yabuuchi *et al.*, “Origin of stabilization and destabilization in solid-state redox reaction of oxide ions for lithium-ion batteries,” *Nat. Commun.*, vol. 7, no. 1, p. 13814, Dec. 2016, doi: 10.1038/ncomms13814.

[174] M. S. Whittingham, “Lithium Batteries and Cathode Materials,” *Chem. Rev.*, vol. 104, no. 10, pp. 4271–4302, Oct. 2004, doi: 10.1021/cr020731c.

[175] A. Urban, J. Lee, and G. Ceder, “The Configurational Space of Rocksalt-Type Oxides for High-Capacity Lithium Battery Electrodes,” *Adv. Energy Mater.*, vol. 4, no. 13, p. 1400478, 2014, doi: 10.1002/aenm.201400478.

[176] J. Lee, A. Urban, X. Li, D. Su, G. Hautier, and G. Ceder, “Unlocking the Potential of Cation-Disordered Oxides for Rechargeable Lithium Batteries,” *Science*, vol. 343, no. 6170, pp. 519–522, Jan. 2014, doi: 10.1126/science.1246432.

[177] Y. Pei *et al.*, “A medium-entropy transition metal oxide cathode for high-capacity lithium metal batteries,” *Nat. Commun.*, vol. 13, no. 1, Art. no. 1, Oct. 2022, doi: 10.1038/s41467-022-33927-0.

[178] J. W. Sturman, E. A. Baranova, and Y. Abu-Lebdeh, “Review: High-Entropy Materials for Lithium-Ion Battery Electrodes,” *Front. Energy Res.*, vol. 10, 2022, Accessed: Dec. 10, 2023. [Online]. Available: https://www.frontiersin.org/articles/10.3389/fenrg.2022.862551

[179] J.-W. Yeh *et al.*, “Nanostructured High-Entropy Alloys with Multiple Principal Elements: Novel Alloy Design Concepts and Outcomes,” *Adv. Eng. Mater.*, vol. 6, no. 5, pp. 299–303, 2004, doi: 10.1002/adem.200300567.

[180] B. Cantor, I. T. H. Chang, P. Knight, and A. J. B. Vincent, “Microstructural development in equiatomic multicomponent alloys,” *Mater. Sci. Eng. -Struct. Mater. Prop. Microstruct. Process.*, vol. 375–377, pp. 213–218, Jul. 2004, doi: 10.1016/j.msea.2003.10.257.

[181] C. Oses, C. Toher, and S. Curtarolo, “High-entropy ceramics,” *Nat. Rev. Mater.*, vol. 5, no. 4, pp. 295–309, Feb. 2020, doi: 10.1038/s41578-019-0170-8.

[182] R.-Z. Zhang and M. J. Reece, “Review of high entropy ceramics: design, synthesis, structure and properties,” *J. Mater. Chem. A*, vol. 7, no. 39, pp. 22148–22162, 2019, doi: 10.1039/C9TA05698J.

[183] H. Ji *et al.*, “Hidden structural and chemical order controls lithium transport in cation-disordered oxides for rechargeable batteries,” *Nat. Commun.*, vol. 10, no. 1, Art. no. 1, Feb. 2019, doi: 10.1038/s41467-019-08490-w.

[184] Z. Lun *et al.*, “Design Principles for High-Capacity Mn-Based Cation-Disordered Rocksalt Cathodes,” *Chem*, vol. 6, no. 1, pp. 153–168, 2020, doi: 10.1016/j.chempr.2019.10.001.

[185] R. J. Clément, D. Kitchaev, J. Lee, and Gerbrand Ceder, “Short-Range Order and Unusual Modes of Nickel Redox in a Fluorine-Substituted Disordered Rocksalt Oxide Lithium-Ion Cathode,” *Chem. Mater.*, vol. 30, no. 19, pp. 6945–6956, Oct. 2018, doi: 10.1021/acs.chemmater.8b03794.

[186] B. Ouyang *et al.*, “Effect of Fluorination on Lithium Transport and Short-Range Order in Disordered-Rocksalt-Type Lithium-Ion Battery Cathodes,” *Adv. Energy Mater.*, vol. 10, no. 10, p. 1903240, 2020, doi: 10.1002/aenm.201903240.

[187] L. Li *et al.*, “Atomic-scale probing of short-range order and its impact on electrochemical properties in cation-disordered oxide cathodes,” *Nat. Commun.*, vol. 14, no. 1, Art. no. 1, Nov. 2023, doi: 10.1038/s41467-023-43356-2.

[188] Y. Gao, X. Wang, J. Ma, Z. Wang, and L. Chen, “Selecting Substituent Elements for Li-Rich Mn-Based Cathode Materials by Density Functional Theory (DFT) Calculations,” *Chem. Mater.*, vol. 27, no. 9, pp. 3456–3461, May 2015, doi: 10.1021/acs.chemmater.5b00875.

[189] A. Jain *et al.*, “Formation enthalpies by mixing GGA and GGA $+$ U calculations,” *Phys. Rev. B*, vol. 84, no. 4, p. 045115, Jul. 2011, doi: 10.1103/PhysRevB.84.045115.

[190] Z. Hu and H. Metiu, “Choice of U for DFT+U Calculations for Titanium Oxides,” *J. Phys. Chem. C*, vol. 115, no. 13, pp. 5841–5845, Apr. 2011, doi: 10.1021/jp111350u.

[191] S. Pandey *et al.*, “Electronic structures and magnetism of Zr-, Th-, and U-based metal-organic frameworks (MOFs) by density functional theory,” *Comput. Mater. Sci.*, vol. 184, p. 109903, Nov. 2020, doi: 10.1016/j.commatsci.2020.109903.

[192] K. Choudhary and B. DeCost, “Atomistic Line Graph Neural Network for improved materials property predictions,” *Npj Comput. Mater.*, vol. 7, no. 1, p. 185, Nov. 2021, doi: 10.1038/s41524-021-00650-1.

BIOGRAPHICAL SKETCH

R. Seaton Ullberg was born and raised in Winter Park, Florida. He received his Bachelor of Science in Materials Science and Engineering from the University of Florida in 2019. He went on to continue his graduate studies under the supervision of Prof. Simon R. Phillpot at the University of Florida earning a Master of Science in Materials Science and Engineering in 2021. Prior to beginning his graduate studies, Seaton joined the Phillpot Research Group as an undergraduate from 2017 to 2019 and worked on strategies for the rational development of interatomic potentials under the mentorship of Dr. Eugene Ragasa. His doctoral research was multifaceted – spanning multiple simulation methodologies and materials systems. His most notable projects addressed impactful research areas including high-temperature oxide formation, nuclear waste sequestration, and advanced battery development. He contributed to research sponsored by the US Department of Energy through the Nuclear Energy University Program and in collaboration with the National Energy Technology Laboratory.